ALMA MATER STUDIORUM · UNIVERSITÀ DI BOLOGNA

Scuola di Scienze
Dipartimento di Fisica e Astronomia
Corso di Laurea Magistrale in Fisica

Statistical Characterization of Cultured Neural Networks Activity recorded via MEA

Relatore:
Prof. Daniel Remondini

Correlatore:
Dott. Jugoslava Aćimović

Presentata da:
Daniele Corradini

Anno Accademico 2018/2019

"Onni ei tule etsien, vaan eläen"

Abstract

In questa tesi si sono analizzate le attività di neuroni in coltura estratti dalla corteccia cerebrale di ratto. Per registrarne il potenziale extracellulare, che è stato poi convertito sotto forma di spike, questi neuroni sono stati accoppiati con un Multi-Electrode Array a 60 canali. Sebbene presentano varie limitazioni, le reti neurali *in vitro* consentono un maggior controllo sul sistema perciò sono molto utilizzate nello studio delle funzionalità cerebrali, sia a riposo che stimolate. Tuttavia, essi sono influenzati da diversi fattori, come la densità, l'età e l'animale di provenienza dei neuroni, che ne rendono lo studio complicato. Lo scopo di questa tesi è proprio quello di caratterizzare questa variabilità attraverso vari metodi statistici, dai più tradizionali alle tecniche di Machine Learning, per capire l'attendibilità di questi sistemi semplificati. Inoltre, gli strumenti analitici utilizzati possono essere adattati a studi che utilizzano la stessa metodologia sperimentale. Utilizzando un software sviluppato in Python si sono estratte 40 misure che cercano di descrivere un ampio spettro delle attività, sia del singolo elettrodo che dell'intera rete, come lo spiking e i network bursts, attraverso tecniche standard, di correlazione e i più sofisticati Poicaré plots. Tutte queste misure sono state sistematicamente analizzate con l'obiettivo di classificare correttamente i campioni, tenendo conto anche dei fattori di confusione. Si inizia studiando le distribuzioni ed effettuando la PCA per vedere la segregazione dei dati nelle classi considerate. In seguito vengono implementati due classificatori, un K-Means Clustering e un Random Forest. Il primo, in accordo con i risultati ottenuti sulla separabilità delle classi, non raggiunge un'accuratezza elevata, mentre nel secondo le perfomance raggiunte sono migliori. Inoltre, questo metodo ci permette di calcolare l'importanza relativa delle feature usate nella classificazione, riscontrando che non c'è un gruppo particolare di misure che si contraddistingue dalle altre. In generale, vista la complessità dei dati, per ottenere una buona accuratezza occorrono molte feature. Un problema che si riscontra quando si stratificano i dati affetti da alta variabilità è l'overfitting dovuto alla scarsità dei campioni. Per far fronte a questa problematica si sono divise le serie temporali degli spike in modo da moltiplicare i dati a disposizione. In questo modo è stato studiato anche l'effetto del sottocampionamento temporale sulle misure, determinando che anche prendendo un quarto del campione si sono potute estrarre misure con un contenuto informativo significativo. Un altro tipo di sottocampionamento preso in considerazione è quello spaziale, un aspetto importante le cui consequenze ricadono su tutti i dispositivi che registrano l'attività cerebrale. Le misure si sono dimostrate abbastanza robuste perchè, a parte il caso in cui sono stati analizzati i dati registrati da soltanto 10 elettrodi, significativi cambiamenti non sono stati osservati. Questo studio sulla robustezza alla variabilità e al sottocampionamento delle misure ricavate dalla attività spontanea dei neural network *in vitro* ha ripercussioni sulle dinamiche perturbate da sostanze chimiche, stimoli elettrici o malattie.

Abstract

In this thesis we analysed cultured neural network activity, extracted from rat cortex. In order to record the extracellular potential, converted then into spikes, these cultures were coupled with a 60-channels Multi-Electrode Array. Although with its limitations, *in vitro* neural networks are really useful for understanding the brain functions, both in resting and stimulated state, because they allow more control over the system. However, many factors could influence their activity, i.e. plating density, culture age and batch, making their study tricky. To understand the faithfulness of this simplified system, this work aims to quantitative characterize this rich variability through various statistical methods, from the more traditional to machine learning techniques. Specifically, 40 different measures were extracted with a Python custom-made software, describing a wide spectrum of activity, both at single-channel and network level, such as the spiking and network bursts, by means of standard methods, correlations and more sophisticated Poincare plots. All these measures have been systematically analysed with classification purpose, being aware of the role of the confounding factors. We started looking at the distributions and performing the PCA to check if the selected samples shown class segregation. Afterwards, two classifiers were implemented, K-Means Clustering and Random Forest, an unsupervised and a supervised method, respectively. The former, in agreement with the preliminary results on class separability, did not achieve a high accuracy, while in the latter the performance considerably improved. Moreover, using this technique we could compute the relative feature importance, noticing that in almost all the classifications, a particular group of measures that contributed more was not found and, due to the complexity of the data, many features were needed to obtain good results. Due to the scarcity of data, overfitting is a common problem that come up when stratifying the data affected by many confounding factors. Data augmentation by splitting the recording in equal parts could overcome this issue. In this way we also studied the effect of temporal subsampling on the measures, determining that even with a quarter of the recording, we extracted measures that still retained meaningful information. Furthermore, we assessed spatial subsampling because it has crucial consequences on all the neural recording devices. Except the case when only 10 electrodes were considered, the measures were not substantially affected by the electrodes removal. Studying the measures robustness under variability and subsampling in spontaneous activity has an important impact on the cultured neural network dynamics perturbed by chemical compounds, electrical stimuli or disease.

Contents

Introduction

The brain is among the most complex systems in nature because it is composed by an enormous number of interconnected components. The brain consists of about 100 billion neurons and each neuron can have up to 10^5 inward connections. Thus, the whole brain represents a huge network with complex connectivity. Furthermore, brain networks possess multi-scale organization, from microscopic scale of networks of neurons to macroscopic networks between brain regions. In order to understand how the brain works we need to understand all these scales of organization.

In this work we focus on the microscopic scale of neuronal networks. These networks can be studied using various preparations. If a study focuses on fundamental biological mechanisms in cells, synapses and small networks, the experiments can also be done *in vitro*. These experiments are cheaper, it is easier to control them, to collect and analyse the data, and they also pose less ethical issues. In particular, we focus on one specific *in vitro* experimental preparation, the dissociated cortical cell cultures. In this preparation, neural cells are extracted from the brains of young animals, e.g. the cells can be obtained from the cortex of just born rats. These cells are plated in a Petri dish, regularly fed, and used to collect recordings for up to a month.

A recording technique that allows long-term recordings and uniform sampling of activity from the entire cell culture is multi-electrode array (MEA). The MEA consists of a planar grid of electrodes embedded into the central part of the dish, which allows that plated neurons grow in proximity of the electrodes. Each electrode collects the summed activity originating from a few neurons located close to the electrode. This raw activity in form of time-series data is further processed to extract relevant signals, which will be further discussed in Methods.

The typical recordings obtained from dissociated cell cultures using MEA show network bursts. Network bursts are stereotypical spatio-temporal patterns that consist of shorter intervals of intensive activity spreading across multiple points in the network. In-between bursts, the network activity is sparse and unsynchronized.

We extracted a wide range of measures that were carefully analysed to assessed quantitatively the amount of intrinsic variability of the data. The whole characterization of the neural network activity was performed using different type of statistical and machine learning tools [8], implemented by means of a Python custom-made software. In particular, these tools were applied to the data collected from various culturing protocols and days in vitro. As MEA recordings represent heavily subsampled representation of network activity [25], the sensitivity of these tools to subsampling is carefully examined.

The data analysis pipeline proposed in this study can easily be applied to any work that utilizes MEAs to record from dissociated cell cultures. The combination of dissociated cell cultures and MEAs has been widely used to study underlying mechanisms of neural excitability and information transmission in neural circuits [49, 47, 56, 54]. Moreover, the dissociated cell cultures are routinely used in pharmacological screening, and for testing of neuro-toxicity [20, 44]. Finally, dissociated neural cultures obtained from human stem cells are a very promising and ethically acceptable way to study human neural systems in health and pathology.

Each of these applications uses a similar setup, a set of recordings is collected from the unperturbed 'control' cultures, and another set of recordings is collected from the cultures perturbed in some way, e.g. by applying chemicals or having a genetic variability specific for some disease. The conclusions are obtained by assessing similarity/differences between the recordings from control and perturbed cultures. Clearly, the steps used to extract relevant features from the raw recordings as well as the methodology used to compare the two data sets can have huge effect on the final conclusion. Therefore, before performing this kind of tests is crucial to understand the deep-rooted source of variability of this kind of data. Thus, in this thesis we considered a multi-parametric approach, i.e. classification method, to reliably predict culture age, density and batch, by performing feature selection for the specific classification task.

This thesis would yield contributions by testing typical methods to extract features from the data, by testing the state-of-the-art methods to classify control vs perturbed data. Classification allows precise way to compare the data, to quantify (dis)similarity between data sets, and to evaluate significance of the comparison. Furthermore, we assessed to analyse how the subsampling of the neural network affects classification. In principle, more electrodes provide more information about the neural network. But less electrodes mean less heavy data, less demanding data analysis step, more efficient experimental protocols.

Briefly, the aim of this work is to meticulously studying a comprehensive set of measures to characterize to what extend the complex dataset obtained from the unperturbed activity of *in vitro* neural network is affected by variability and subsampling. This should lead to a more meaningful utilization of this methodology, that is, by choosing a suitable set of features that separate the different neural dynamics, being careful at the confounding factors that can bias the outcomes.

In general, the thesis can be divided into two main parts, the first chapter, the background, ad the last two chapters, the original work.

In the first chapter the state-of-the-art about the dissociated neural network, Multi-Electrode arrays and network burst dynamics is shortly reported. Specifically, it is introduced the experimental methodology used for obtaining the data, the neural networks *in vitro* models. First, a general overview of dissociated neural cultures is given, focusing on their limitations and advantages. Next, MEA device is described, illustrating its electronic structure, the physics behind its functioning and showing its most important applications in Neuroscience. Moreover, the last section of the chapter gives a brief insight into the *in vitro* neural network dynamics, focusing on the most striking property of this system, the network burst.

In the second chapter the dataset is accurately described, illustrating which kind of recordings contains and how the database is organized according to different factors, e.g. culture age, density and batch. Furthermore, the developmental evolution of the spiking activity of the cultured neural network is qualitatively shown. Then, the analysis pipeline is reported, from the preliminary steps used to extract the measures, i.e. the burst detection, to the machine learning methods implemented for studying the feature robustness. In the last part of the chapter, the focus is given to the several techniques used for quantifying the neural network dynamics, reporting both standard methods, more sophisticated approach adopted from chaotic time-series analysis, and spike train synchrony.

The final chapter shows the main results of the analysis. All the measures extracted from the neural activity data were systematically explored by plotting all the developmental trends, checking also how they are qualitatively influenced by density and batch. Subsequently, a more quantitative approach was conducted at various levels, starting from preliminary exploratory statistics, such as some basic distribution comparison and PCA visualization to check the linear separability of the classes. Finally, also more advanced analysis based on machine learning techniques were implemented, using both unsupervised and supervised methods. Here, different classifications to separate classes belonging to different densities, ages or batches were performed, also in the presence of temporal and spatial subsampling. Using the Random Forest algorithm the relative feature importance was analysed as well.

In conclusion, it came out that the data sets analysed were highly complex, as for each culture condition we considered, e.g. density, days *in vitro* and batch, the classes were not linearly separable. However, the supervised classification achieved good performances using the comprehensive set of measures we extracted from the recordings. The contribution of the features in the classification task was case-specific to the condition to discriminate. Moreover, the measures were not considerably affected by subsampling, both temporal and spatial.

Chapter 1

In vitro Neural Networks

In the first chapter is introduced the cultured neural network, that coupled with Multi-Electrode or Microelectrode Array (MEA) technology, represents an important *in vitro* model for studying the neural properties widely used in neuroscience research. This experimental methodology was used in [55] for obtaining the data analysed in this work. After a general overview on cultured neural network preparation, the MEA device is described, illustrating its functioning and some technological and clinical applications. Furthermore, the network burst activity is shortly described.

1.1 Dissociated Neural Cultures

Dissociated neuronal cell cultures are one of the standard experimental preparations used in neuroscience research. They allow easy recording (e.g. using electrodes or microscopy) and manipulation (e.g. using electrical stimulation or pharmacology) of neurons and networks of neurons. They were first proposed by an American biologist Ross Granville Harrison and soon spread to many other laboratories. For more than a century, this methodology has been improved to provide healthier cells, better differentiation and growth, longer survival of cells and cultures, leading to better quality of recordings and better reproducibility of results [5].

In order to understand the experimental methodology behind the extraction of the neural network activity data, we report some basic information about cell culturing, focusing on the neural cultures preparations used in [55]. The technique that permits to control in a *in vitro* environment cell growth is called **cell culture**. In particular, if the cells are extracted from the tissue and re-grown *ex novo* the method is called **dissociated cell cultures**. The neural tissue is taken from a specific part of the brain of young animals because cells from a young brain can easier adapt to new conditions in a culture. The brain area could be, e.g., prefrontal cortex [49], cortex including somatosensory, motor and association areas [55], hippocampus [47]. As we are dealing with neural tissue taken form cortex, in this case the experimental methodology is also called **cortical cell culturing**. While many animals can be used as cell donors, we focus on rodent (mice and rats) cultures that are the most common choice. The tissue is taken either from yet unborn animals (prenatal), or soon after birth (postnatal). We used data from rat embryos at day 18 of gestation (E18). The cells are extracted from the tissue using mechanical and pharmacological dissociation. The result of dissociation protocol is a liquid containing all cell types naturally found in the considered brain area, including **neurons** and **glia cells**, the unit blocks of the brain. The density of the cells in the liquid can be measured and it is an upper bound of the density of cells in the culture, as some cells inevitably die in culture. The liquid containing cells extracted from the tissue is then placed in a Petri dish where cells continue to grow ***in vitro***, that is usually properly pre-treated to enhance the life-span of the cells. Moreover, the cultures area grown under a sealed chamber to prevent contamination and reduce evaporation. In a dish, neurons can re-grow **neurites** removed during dissociation, specifically, the **dendrites** and the **axons**, the neuron ramifications involved in the afferent and efferent signal transmission, respectively. The **synapses**, the specialized structure that enables the neurons to communicate, are also formed between these neurites. The cells start interacting already during the first days in a dish, and in [55] the neural activity, composed by sparse and random spikes, was detectable from the third day *in vitro*. At the end of the first week *in vitro* some more structured activity patterns were recorded, as tiny network bursts. This means that the creation of new connections among the neurons starts after few days after plating the cells, make it possible to early record the **neural network** activity.

Here it is provided a short description of the main attributes of *in vitro* neuronal networks, highlighting the potential of this experimental methodology as well as its limitations.

1.1.1 Disadvantages

Although cultured neural networks led to improvements in the field of neuroscience, similarly to any simplified model, they have also many drawbacks.

When the neurons are extracted from the neural tissue and suspended in solution, their original connections are destroyed. The neurons suspension is left grow under a controllable setting for enabling the condition to form new synapses linkage. Thus, the new connectivity is drastically changed from the original template, influencing in such way also the functionality.

Moreover, cultured networks are usually plated in a Petri dish so the neurons have to be placed in a single-layer sheets of cells. This implies an even more disrupted connectivity, that from a three-dimensional architecture becomes a flat layer of neurons that lacks the original richer interconnectivity. This method could retain some functional properties of the tissue of origin even if as we saw, anatomically, dissociated cultures are far from being similar to the complex neural tissue structure. This disadvantage is overcome by new protocols that allow growth of organoids.

The cells are growing *ex vivo* so no sensory inputs affects cell growth. *In vivo*, it is known that sensory inputs significantly affect development. The sensory deprivation could have consequences on the normal cell development and they could express different network activity patterns [38].

An issue to not underrate when dealing with this kind of experimental preparation is their lack of longevity, due to neuron death. The neurons grow in an artificial environment and the protocols have to be carefully carried out to provide healthy cells and networks. Some experiments need to follow morphology changes and the activity alterations of the network for months, in particular, when one wants to assessed learning and memory mechanisms. Thus, enabling long-time recording and making the cultures survive as long as possible is crucial [40, 32].

1.1.2 Advantages

First of all, it represents a simplified neural model, a good compromise considering that sometimes studying realistic complex *in vivo* models can be really hard or even impossible due to ethical issue. It allows researchers to investigate neuronal activity in a much more accessible environment than would be possible in a living organism because the experimental protocol is easier and cheaper to prepare. These *in vitro* systems still possess basic biological mechanisms of neurons and neuronal networks and allow studying integration of cellular, synaptic and network mechanisms.

Moreover, pharmacological analysis of neurons and their environment is more easily accomplished than in an *in vivo* setting, as cultured neural networks offer easy control when applying chemical compounds [41], making them a useful setup for drug testing.

Neurons cultures made by rodents brain tissue has been an economical compromise in many studies. Seen the advantages of this experimental preparation, non-human cell cultures keep to be an acceptable source of cells for many purposes. In order to improve the accuracy of predictions, human pluripotent stem-cells are believed to be a good replace because they will allow us to study human neurons with less ethical issues. This makes the stem-cells cultures a promising experimental model of diseases. In this work we implemented a methodology for analyzing data from cell cultures that can be used for any type of cultures. Thus, we used a standard and well known protocol, rodent cell cultures, to test and develop methodology that can be used also for other type of 2D cultures including human stem-cell cultures.

1.2 Multi-Electrode Array

Understanding the maturation, arrangement, and emergent patterns of neuronal networks *in vitro* has been facilitated by advances in Multi-Electrode Array (MEA) technology. The possibilities offered by MEA devices allow the simultaneous monitoring and stimulation of many units non-invasively for long-term recording. This allows to analyse complex emergent neural properties and the underlying principles behind plasticity, connectivity, and information processing. Moreover, dissociated neuronal networks coupled with MEAs have been used as a standard model to investigate drugs neurotoxicity and human disease.

From the first introduction of MEAs (see [50, 16, 37] for the pioneering studies) many types and configurations have been developed. Depending on the research purpose, on the experimental preparation and the required resolution, different MEA settings have been used, with different number of electrodes, geometrical disposition, thickness and materials. For some particular phenomena high spatial sensitivity down to single cellular level is required in order to get more insights from the neural activity. The CMOS technology had led to build high-density MEAs to fulfill this need, permitting high spatial resolution recording almost at single neuron scale. Moreover, when dealing with neural network activity measures, to ensure robustness over the high inter-culture variability, a certain number of recordings is usually performed, as in drug screening experiment. In order to satisfy this requirement multi-well MEAs have been introduced that allow multiple recordings at the same time on a singe plate. A drawback of this platform is that the number of electrodes per well tends to decrease with the number of wells per plate. Thus, multi-well/high-density systems are in the wish list of the future neuroscience-related technology developments.

The authors of the data [55] used MEAs with 59 electrodes with a diameter of 30 μm, purchased from Multichannel Systems (Reutlingen, Germany), as the one on the upper left plot in figure 1.1. The electrodes were organized in a square grid with the corners missing, spaced 200 μm center-to-center. One electrode on the edge of the array was also absent because replaced by a large ground electrode.

FIGURE 1.1: Some of the MEAs produced by Multi Channel System (Reutlingen, Germany). Image from www.multichannelsystems.com.

MEA is an **extracellular recording** devise because allows measures of the extracellular activity from a population of neurons growing in close proximity to the electrodes. The output of the recording is a time series representing the extracellular potentials/voltages generated by several neurons located in vicinity of the electrodes. Such recordings reflecting the activity of several neurons are called **multi-unit recordings**. In [55] recordings took place in the same incubator used for maintaining the cultures and it started immediately after transferring each culture into the recording device. Then, those recordings were preprocessed by removing noise by filtering. Each time the extracellular voltage recording exceeds a certain threshold a time stamp, called **spike**, is saved. Spikes reflect action potentials from all neurons close to the electrode. An **action potential** is an event cause by an abrupt change of the membrane potential of a cell due to alterations in the ion concentrations, both in the intra- and extra-cellular environment. Specifically, the neuron strongly depolarizes the membrane voltage and, after a short time, this value is restored to the resting state, a mechanism that follows a coherent trajectory. In [55] MEA Bench software [53] was used for data acquisition and online spike detection. Spikes were detected set a threshold to 4.5 times of the estimated noise, both for upward or downward excursion of the voltage. A collection of spikes recorded during the entire recording time is called **spike train**. Each active electrode records one spike train. The spike trains from all electrodes can be combined into a **population spike train**. Both individual spike trains from electrodes, as well as the population spike train are typically analyzed to extract significant features of the cell culture activity.

1.2.1 Functioning and Electronics Insight

This section describes the technology behind the most common MEA chips, giving emphasis towards the physical prerequisites for an adequate extracellular stimulation and recording. Moreover, a short overview about the electronic design is given.

The main goal of a MEA chip is to record a signal from cells with the size of the order of micrometers so proper design and materials are needed to achieve a good signal quality when dealing with this reduced scale. In order to build a well-designed device one has to carefully select the main components, namely, substrate, conductors, insulators, electrodes and culture chambers. Moreover, the materials used to fabricate the components have to be properly chosen.

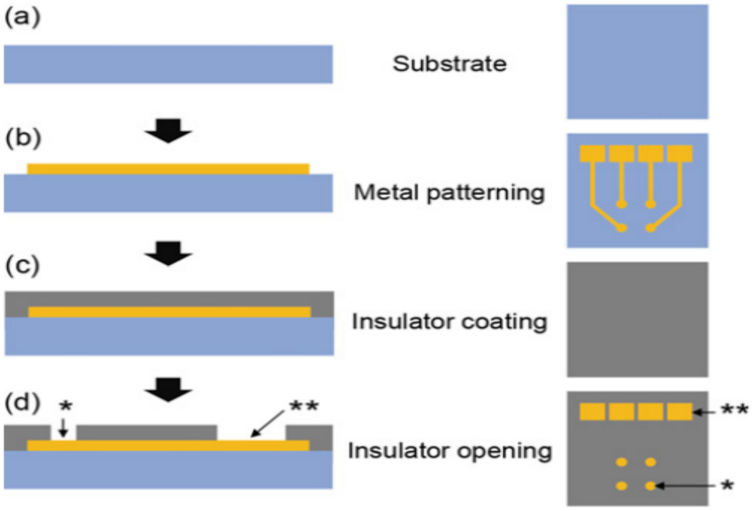

FIGURE 1.2: The fabrication steps for building a typical MEA chip: metal patterning, insulation, and electrode opening [22].

The figure 1.2 taken from [22] schematically illustrates the main fabrication steps. A patterned patina of metal is used to cover the substrate that represents the base of the device. The number of microelectrodes and the distance among them are determined by the pattern design. The conductor lines are covered by an inert insulator resistant to ionic solutions. Moreover, electrodes and contact pads are defined through holes on the insulator that expose the metal surface (connected with amplifier and filter) and the dimension of the opening determines the electrode size.

In order to obtain good quality recordings (or stimulation) with an high signal-to-noise ratio, a low electrode-culture medium impedance is desirable. Since the electrode size is of the order of the neuron size, the surface is modified with high-conductive materials to decrease the impedance [32].

Basically, MEA device is a flat ensemble of extracellular voltage probes allocated with a specific geometry (e.g. square, hexagonal) that can be used both for recording or stimulating the excitable cells it is coupled with. Therefore, at the base of the MEA functioning is the neuron-electrode coupling. In fact, as it is shown in figure 1.3, in order to detect the extracellular potential change, the neurons have to grow nearby or upon the electrode. The cell-electrode interface can be interpreted as an electronic component and its physical configuration explains the main properties of the recording, as the shape and the quality of the detected signal [32, 30].

The neurons grow on the MEA chip and soon they start to make contact with the surface of the electrodes. For example, in [55] MEA starts to detect spikes after 3 days. There are different physical theory attempting to explain how the recording (or stimulation) works. For instance, one can think at the cell-electrode interface as a circuit where the area of interaction between them can be represented as a resistance within which flows a current caused by the extracellular potential variation during a spike. In particular, the resistance can be high enough to produce a detectable voltage ranging from tens to hundreds of μV [22]. Physically a neuron can be imaged as a dipole where sink and source correspond to axon hillock and dendrites, respectively. Using a distributed current dipole model, it can be explained how the voltage

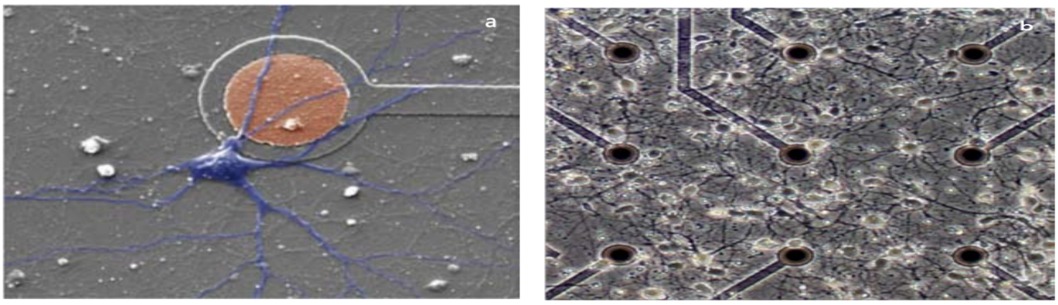

FIGURE 1.3: On the left the neuron-electrode interaction of a MEA chip in the second week *in vitro*. On the right dissociated neurons coupled with a MEA. Images taken from [32]

polarity depends on the position of the electrode with respect to the dipole (neuron). As the neurons directly grow on the electrodes (see figure 1.3) when recording the neural activity for a long time one should consider many aspects that may affect the performance of the detection. For example, the continuing culture development, e.g. the neuron extension and the adhesion to the electrode surfaces, the glial growth or the protein deposition, may increment the insulation of the micro-electrode reducing the quality of the signal [22].

There are many factors that affect the action potential shape, such as cell morphology, distance and coupling strength with the electrodes. All these different factors could change during neurons maturation leading to a spike waveform evolution in long-term recordings. Moreover, it can happen that a cell die, migrate or is replaced by another active cell, determining changes action potential amplitude. The main source of spike variability during maturation is associated with ion channel and synapses creation that obviously influences the membrane excitability. However, the neurons are not the only cells present in the cultures. The glial cells have a strong contribution in modulating the action potential, strengthening or weakening the signal depending on the relative position with respect to the electrode, and also by metabolic effects. As the electrodes are placed in the extracellular medium they are able to detect just the super-threshold activity, that is the action potentials, limiting the analysis insights to a small part of the neural signal. However, new technological developments are trying to overcome this issue allowing also in-cell recordings via MEA [32].

1.2.2 Applications

MEA device has been an essential biosensor for studying not only the neuronal plasticity and information processing but also in drug and toxin effects on neurons, modeling brain disorders and for machine-brain interfaces (see figure 1.4).

The good spatiotemporal resolution of the MEA device, together with the high sensibility towards the chemical environment of cultured neural networks, makes this experimental technique very useful in **drug screening** and toxicology testing. The monitoring after treating a neural culture *in vitro* with chemical compounds takes place starting from few days, for studying the acute affect, up to months, when long-term consequences have to be assessed [20]. The high-throughput data obtainable from MEA recordings are suitable for extracting information about the functional connectivity of the network subject to external perturbations, as well as the usual aspect of the neural activity, i.e. spikes and network bursts. Below, the

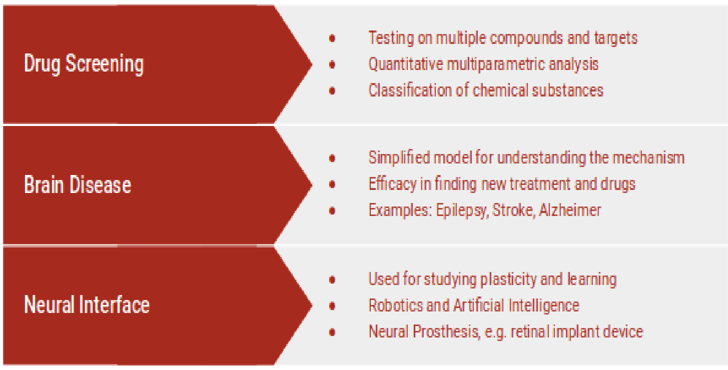

Drug Screening	• Testing on multiple compounds and targets • Quantitative multiparametric analysis • Classification of chemical substances
Brain Disease	• Simplified model for understanding the mechanism • Efficacy in finding new treatment and drugs • Examples: Epilepsy, Stroke, Alzheimer
Neural Interface	• Used for studying plasticity and learning • Robotics and Artificial Intelligence • Neural Prosthesis, e.g. retinal implant device

FIGURE 1.4: Table summarizing the main applications of MEA device, i.e. drug and toxicology screening, modeling brain disease and building machine-brain interfaces and prosthesis.

advantages of MEAs for screening compounds for potential neurotoxicity are summarized [20]. As we already said in Section 1.1.2, these systems *in vitro* are simple and easy-controllable models for studying the drug effect on neural activity. This technology, combined with the advanced machine learning tools (e.g pattern recognition analysis), could lead to an advancement in pharmacological treatment and toxic substance effect at the network level as well as at sub-cellular scale of ionic channels and receptors. Moreover, the long-term recording permits also to asses the developmental effect under repeated or chronic chemical perturbation performing the measurement multiple times on the same network. Studying the effect of multiple compounds or multiple targets (e.g. multiple receptors) is also possible. As it will be better described in the next chapter, this experimental setup allows to extract a rich information content just from the analysis of the extracellular voltage recordings, as spike trains, network bursts and synchronicity. Calculating an high number of diverse measures has the advantage to achieve an in-depth study of many different neural network mechanism. It also permits a better usage of the classification task, indispensable for this type of drug screening when testing the global effect of an unknown substance [44].

This short paragraph illustrates how *in vitro* systems can be used to study **brain dysfunctions** at cellular and sub-cellular level, as well as looking at disrupted network dynamics. For example, disorders associated with circulation problems (e.g. stroke [5]), excitability (e.g. epilepsy [5] and memory (e.g. Alzheimer [5]) have been studied with this experimental methodology. Through the use of dissociated neural networks coupled with MEA the researchers are able to investigate disrupted physiology mechanisms, to identify novel biomarkers and treatment, or to pursue high-throughput drug screening. As we already discussed in Section 1.1.2, the *in vitro* models have less practical and ethical issues. The same considerations are valid for studying brain disease, as using *in vitro* surrogates has less complications than *in vivo* or animal models.

In what follows an example of brain disease studied *in vitro* is reported, i.e. the epilepsy, a disorder associated with an excess of neuronal excitability. One of the more prominent spatiotemporal pattern shown by the dissociated neural cultures are the network bursts, an highly synchronized activity that resembles the epileptic dynamics *in vivo*. Dissociated neurons display this characteristic hyper-excitable activity even in absence of external electrical stimuli or chemical manipulation. Indeed, some studies (see [47, 56]) found a connection between increased spiking activity and lack of afferent input in disembodied systems. In fact, when neural cultures are electrically stimulated or pharmacologically perturbed, network bursts can diminish or even disappear [56].

We already mentioned that one of the main drawback of dissociated neural networks is the absence of feedback stimuli. In a brain any sensation formed through association of different phenomena are self-referential, meaning that the neurons are embodied with a sensory and motor system and situated in a environment to interact with. One solution to overcome this issue is to connect cultured neurons with computers or robots so they can experience artificial sensory inputs from the interactions with some external entities or simulated environments. In this way, using a neuro-engineered platform, it is possible to study learning, plasticity and information processing in a more realistic context. Understanding the cognition mechanism can increment our knowledge in neural pathology, **neural interface** and artificial intelligence [3].

In vitro neural interfaces can be used to help developing brain-machine prosthesis. The most prominent example is the retinal implant devices where the high spatio-temporal resolution of MEA chips can be used to replace the retinal ganglion cells. The final goal of this technology is to recover the sight in blind patients by means of electrical stimulation of disrupted retinas. [45].

The analysis tools developed in this thesis is applied to spontaneous activity. However, as the *in vitro* model is the same also when considering the applications listed above, our methodology can easily be used in experiments that attempt to studyThe analysis tools developed in this thesis is applied to spontaneous activity. However, as the *in vitro* model is the same also when considering the applications listed above, our methodology can easily be used in experiments that attempt to studying drug effects, neural diseases and neural interfaces.

1.3 Network Burst

This section gives a brief insight into the *in vitro* neural network dynamics, focusing on the most striking property of this neural system, the network burst (NB). Below its underlying biological mechanism, properties and role in neural processing and plasticity are illustrated, reporting some case studies.

Network burst is a spatiotemporal pattern activity occurring when a large cluster of neurons within a network spikes or bursts in a synchronized manner and in a short period of time. It is usually characterized by an initial rapid phase, called burst onset, when some neurons overcome the threshold potential level, start generating action potentials and through the synaptic connectivity propagate the excitation in other neurons. Finally, negative feedback mechanisms restore the dynamics to the quiescent pre-burst level and this phase, called offset, is usually longer the the previous ones, at least for mature cultures. An example of how a NB looks when analysing spiking data recorded via MEA is reported in figure 1.5. Specifically, the plot on the left shows the spatiotemporal organization of the spikes in a raster plot and the right-hand plot the network burst rate profile peak with visible onset and offset phases. This stereotypical neural network dynamics is a prominent feature of *in vitro* systems, although, similar type of activity has been observed also in the

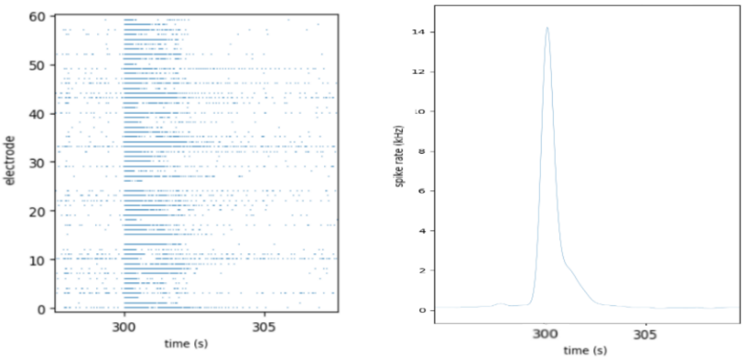

FIGURE 1.5: The plot on the left illustrates a network burst extracted from a typical population spike train of a cultured neural network recorded via MEA. The data come from a dense mature culture of 28 DIVs (dataset obtained in [55]). On the right the rate profile illustrates the network burst frequency peak with an abrupt rising and a longer tailed falling.

developing brain *in vivo* or in epilepsy. In fact, some studies state that this activity is due to lack of sensory input in the disembodied cultures. However, others think that NBs are normal and crucial for various brain functions, as information processing and memory [19]. In any case, understanding this neural activity can help to shed light in various phenomena, in healthy and pathological neural systems [39].

When talking about bursts, it should be stressed out that another phenomena, called (single) neuron burst, also exists. It order to avoid misunderstanding, it is important to also give a definition of neuronal burst. Moreover, single neuron burst can play a role also in the more complex network burst activity because neurons may synchronously bursting together when generating the characteristic spatiotemporal pattern. A neuron is considered to burst when periods of rapid action potential spiking are followed by quiescent periods much longer than typical inter-spike intervals. Various cellular mechanisms determine neuron bursts, but further discussion is out of the scope of this study [19].

In order to unravel the underlying biochemical and biophysical processes behind the generation, the propagation and the termination of a network burst, different researches have studied the effect on the network burst of different perturbation protocols, as electrical stimulation [56, 52] and synaptic or intrinsic current blockers [49, 47]. Initiation, spread and suppression of network bursting is a combination of various cellular, synaptic and network level mechanisms. Also, some putative mechanisms are still investigated and not fully understood. The mechanism behind network bursts is really complex and an exhaustive description of this activity is out of the scope of the thesis. However, in what follows we briefly summarize in a simplistic way the main biological mechanisms.

It has been understood that this spatiotemporal patter is due to a complex interplay between excitatory and inhibitory pathway in synaptic transmission and intrinsic membrane current [49, 47]. During the quiescent period a slow intrinsic current depolarizes some neurons, and eventually the potential reaches the threshold to generate spikes. These neurons are called the initiation sites as they are spontaneously activated and drive the NB in the onset phase [36]. This initial activation is then propagated across the network thanks to the contribution of the fast and slow excitatory synaptic receptors, following the specific connectivity among the neurons that influences the speed of the propagation. However, also other factors, as the actual state of the neurons and the synaptic delays shape this phase [36]. In a short time, with respect to the timescale of the phenomenon under study, the network reaches is maximum firing rate. Afterwards, bursts are terminated due to various mechanisms including synaptic depletion, hyperpolarization of neuronal cell membrane following spiking/bursting interval, recurrent synaptic inhibition and others. Some of the mechanisms might not be fully understood. A returning to the resting state after an intensive bursting period is needed to the neurons and synapses because it allows them to recover before they become able to produce spikes or initiate synaptic transmission again. Thus, in the network burst cycle, a longer period of inactivity between two bursts is fundamental.

1.3.1 Network Burst Evolution in Spontaneous Activity

The *in vitro* neural network dynamic is closely related with the morphological changes during the development. In fact, the maturation of the cultured neurons and their connections (e.g. synaptic formations) affects the properties of the spatiotemporal patterns, i.e. the network bursts. From the first days *in vitro*, when almost no connections are found, until the maturity reached after few weeks, when the network is fully formed, the activity ranges from sparse and random spikes to synchronous and intense network bursts. The interaction among the neurons forms the basis for these stereotyped events that usually involve most of the network. Thus, the structure-function relationship is crucial, as the spontaneous activity shapes the synaptic development through activity-dependent plasticity mechanisms and, at the same time, the emergent dynamics is strongly influenced by the underlying network connectivity [36].

Let us illustrate how to record the spontaneous changes in cultured neurons coupled with MEA chips. Usually, the first spikes are detected after a few days in vitro (DIVs). In the succeeding DIVs, the firing frequency increases in the overall culture. The activity recorded by individual electrodes can greatly vary as it depends on the number of neurons close to the electrode. This variability between different electrodes is also reflected in the individual network burst. Even if network bursts are synchronized firing activity at the network level, still the individual electrodes show differences in their firing rate profile. For instance, after few DIVs new sites can become active or silence, show changing in the maximum firing rate, in the duration of the sustained activity or in the temporal order between individual sites, due to both single neurons maturity and network connectivity evolution. Despite of that, in the short timescale of a network burst a constant underlying dynamics is expected due to the invariant factors in the synaptic connectivity, as topology and synaptic strength. This aspect is evident when averaging different network bursts closely recorded, in such a way to filter out inter-burst fluctuations and highlighting the main spatiotemporal patterns. For example, this is shown in figure 1.6 taken from [35], where it is possible to notice the amount of changing in the averaged network burst rate profile in neural cultures development.

The changes in the rate profile, concerning both the shape, the duration and the maximal firing rate are clear when taking into account few weeks in vitro (WIVs). As we already stressed out, they are due to the underlying morphological development both at neuron and network level. In [35] the authors reported an increase of the NBRP duration up to the 3^{rd} WIV followed by a decrease; in fact, as it is possible

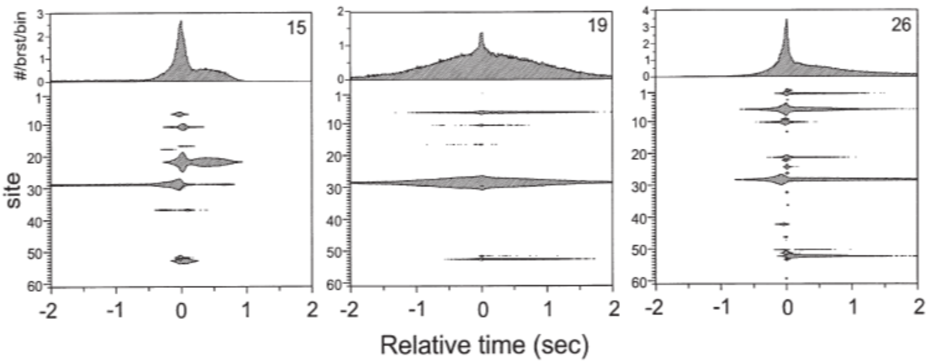

FIGURE 1.6: The upper part of the panels represents the 4 s network burst firing rate profiles at 15, 19 and 28 DIV averaged over all the network bursts found in a recording of 4 h. The lower part shows the correspondent averaged firing rates recorded by each electrode. Adapted from [35].

to see in figure 1.6 the NBRP at 19 DIV is shorter than the one at 28 DIV and, specifically, the shortening regards the onset phase. As far as it is concerned the structural changes, in the first three WIVs the neurons *in vitro* had developed more excitatory than inhibitory synapses. This synaptic unbalance enhance the overall network excitation causing the longer duration of the NBs. From the 4^{th} WIV the excitatory synapses start pruning out but the same does not happen at the inhibitory counterparts, changing in this way the excitatory-inhibitory balance towards the latter. This means a more tuned propagated activity through the network that leads to a shorter and more efficient NB onset phase.

Another example of how the spontaneous *in vitro* cortical network dynamics evolve during the first five weeks is given in [6]. In this study also the cross-correlation analysis is performed in order to get insights in how the functional connectivity emerged during the culture maturation. Moreover, the results have been compared with morphological studies through electron microscopy showing how the number of synapses changes across the DIVs. Also in this case it was observed the typical developmental patterns also reported in [35]. 1) The sparse random firing at few DIVs (figure 1.7.A) mainly due to neurons connected via gap junctions. 2) The low-frequency and large NBs before the 3^{rd} WIV (figure 1.7.B) with a more elevated correlation function due to 'far' and 'fast' connections. 3) The short and high-frequency NBs after the 4^{th} WIV (figure 1.7.C) with functional connectivity dominated by more local and mature excitatory connections.

As we already stated, the developmental changes are highly influenced by the activity-dependent mechanisms [54]. In fact, it can be speculated that the first period is mostly dominated by a global and intense neuronal interaction. After that, during the fourth and fifth WIV, the synaptic maturation leads to more specific dynamics with richer and more elaborated NB patterns, a transient decline of the synapses number and an higher balance between excitatory and inhibitory connections.

It is still not well understood how the information is processed and stored in our brain although some theories suggest that the key properties are to be searched in the dynamically linked cluster of neurons create by activity-dependent mechanism, such as the spike timing dependent plasticity. Since self-organized neural networks

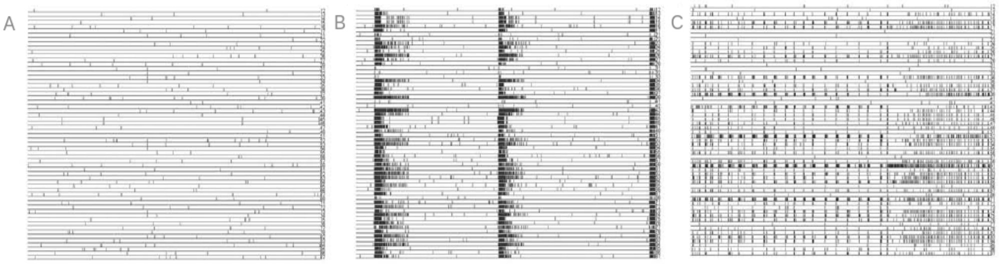

FIGURE 1.7: Raster plots showing the different global firing rate over 60 s of recording in three days *in vitro* (DIV), namely 7 DIV (A), 14 DIV (B), 35 DIV (C). Image adapted form [6].

in vitro are also capable to spontaneously reproduce recurring spatiotemporal emergent patterns, such as network bursts, they represent an optimal model for studying the neural abilities and plasticity mechanisms [42]. One of the most used experimental protocol is to analyse the effect of the electrical stimulation on the spontaneous neural network activity during development. These kind of experiment are making possible to better grasp the influence of structure-dynamic relationship in not yet well understood neural functions [27, 52, 1, 33, 56].

Chapter 2

Materials and Methods

From this chapter starts the original work of this thesis, that is, the statistical characterization of neural network activity recorded via MEA by means of machine learning techniques, both unsupervised and supervised. Firstly, the dataset obtained in [55] is described, illustrating which kind of recordings it contains and how it is organized. Then, the pipeline is reported, from the steps used to extract the measures to the machine learning methods performed for checking the feature robustness.

2.1 Dataset Description

This study uses a dataset published in [55] and considered a benchmark in the field. The access to the data was courteously provided on request by the authors of [55]. In the following paragraph are illustrated the main characteristics of the dataset, giving a brief overview of its properties by summarizing the main information contained in [55], and explaining how it will be used in this work.

2.1.1 Data Organization

The data were recorded from cultured cortical cells of rats by means of a Multi-Electrode Array (MEA) device (Multichannel System, `www.multichannelsystems.com`). The data present an in-depth study of development of burst patterns in cortical cultures over the course of the first five weeks *in vitro* (WIV) , encompassing a total of 963 half-hour-long recordings from 58 cultures of different sizes and suspension densities, determined by the plating volume (V) and the number of cells per plating volume (D), respectively. In total the dataset comprises five different experimental conditions, i.e. dense (V:20 μL; D:2500 cells/μL), small (V:5 μL; D:2500 cells/μL), sparse (V:20 μL; D:625 cells/μL), small and sparse (V:5 μL; D:625 cells/μL), ultra sparse (V:20 μL; D:156 cells/μL). However, in this study we decided to select just dense and sparse cultures (see Table 2.1), because they were the conditions with more recordings, making them more suitable for our classification purpose. The cultures exhibited a wide spectrum of spontaneous activity patterns, characterized by network bursts of different shapes, sizes and frequencies. Hence, this kind of data well fitted the main aim of the thesis - to quantitatively characterize the variability of neural network dynamics.

Dissociated neurons in culture began growing new neurites immediately after plating and soon formed densely interconnected circuits. In figure 2.1 (adapted from figure 2 in [55]) one can see how the neurons grown in dense and sparse dishes. While at 1 DIV the density difference between dense and sparse cultures is clearly visible (see figure 2.1, right most panels), after four WIVs it is not possible to see density differences just using basic microscopy images as the two culture conditions at 32 DIV are not distinguishable anymore (see figure 2.1 left most panels). We should keep this in mind when analysing the differences between dense and sparse measures in Section 3.1.2, when we will quantitatively determine how different is the activity between these two types of cultures during development.

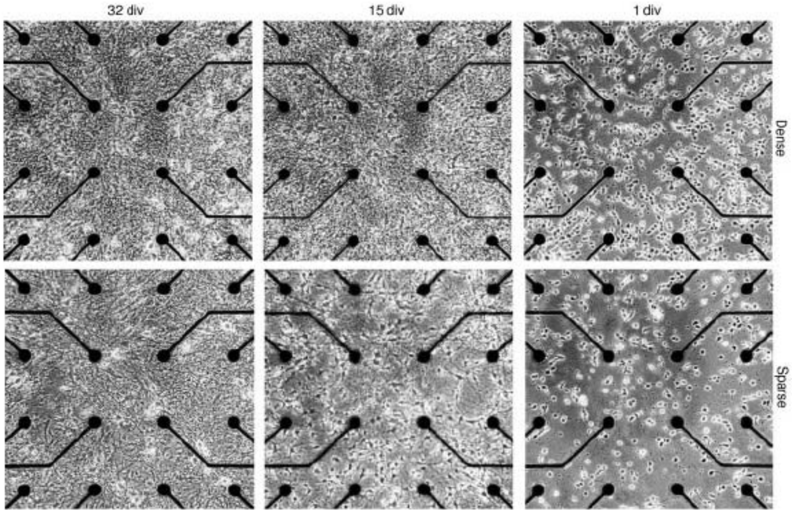

FIGURE 2.1: Photographs of three typical cultures of different densities, at 1, 15 and 32 DIV. Scale: electrode spacing is 200 μm center to center. Adaptation from [55].

Table 2.1 also shows some important plating parameters of the cortical neural cultures used for obtaining the data in [55]. The neurons were plated using different densities of suspension that determined the number of cells plated because the size of the Petri dish used (culture diameter) and the plating volume were the same in both cases. Moreover, the number of cultures followed were 30 for dense and 10 for sparse condition, divided among 8 and 3 batches, respectively. A batch is composed of all the cultures obtained from the same solution of dissociated cells. The cells are typically extracted from several rat pups taken from different litters, then mixed all together during the process of cell extraction from the cortex tissue. The end product is a solution containing various cells from several animals and drops of this solution are plated into individual cultures.

Plating Parameters	**Dense**	**Sparse**
Plating volume (μL)	20	20
Density of suspension (cells/μL)	2500	625
Number of cells plated (nominal)	50000	12500
Culture diameter (mm)	4.9 ± 0.4	4.9 ± 0.4
Drop thickness (mm)	1.69 ± 0.24	1.69 ± 0.24
Density at 1 div (x10^3 cells/mm^2)	2.5 ± 1.5	0.60 ± 0.24
Number of cultures followed	30	10
Number of batches	8	3
Total number of samples	526	159

TABLE 2.1: Plating parameters for dense and sparse cultures. Adaptation from [55].

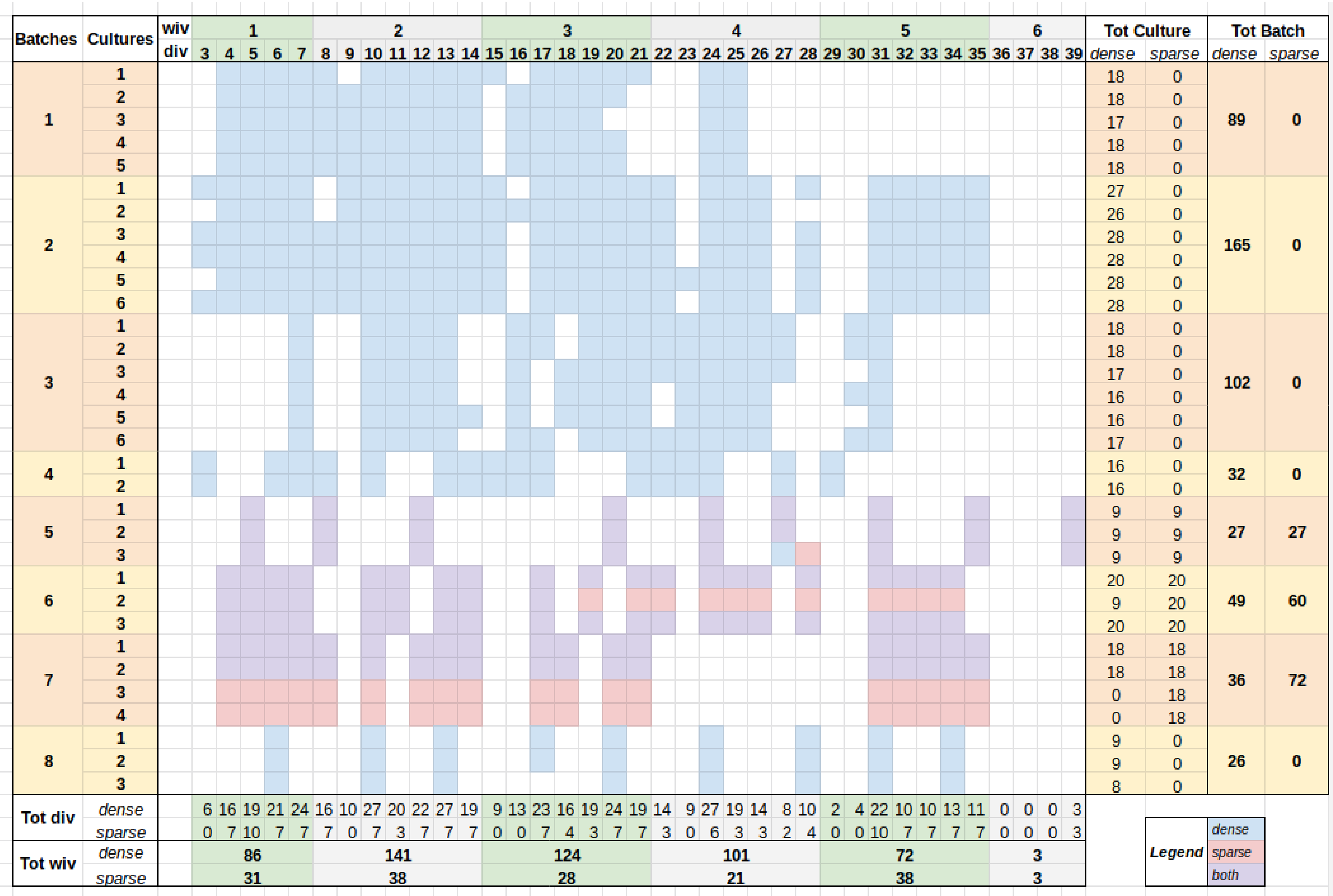

Batches	Cultures	wiv	1					2							3							4							5							6				Tot Culture		Tot Batch	
		div	3	4	5	6	7	8	9	10	11	12	13	14	15	16	17	18	19	20	21	22	23	24	25	26	27	28	29	30	31	32	33	34	35	36	37	38	39	*dense*	*sparse*	*dense*	*sparse*
1	1			🟦	🟦	🟦	🟦	🟦		🟦	🟦	🟦	🟦	🟦	🟦		🟦	🟦	🟦	🟦	🟦			🟦	🟦																18	0	89	0
	2			🟦	🟦	🟦	🟦	🟦	🟦	🟦	🟦	🟦	🟦	🟦		🟦	🟦	🟦	🟦	🟦				🟦	🟦																18	0		
	3			🟦	🟦	🟦	🟦	🟦	🟦	🟦	🟦	🟦	🟦	🟦		🟦	🟦	🟦	🟦					🟦	🟦																17	0		
	4			🟦	🟦	🟦	🟦	🟦	🟦	🟦	🟦	🟦	🟦	🟦		🟦	🟦	🟦	🟦	🟦				🟦	🟦																18	0		
	5			🟦	🟦	🟦	🟦	🟦	🟦	🟦	🟦	🟦	🟦	🟦		🟦	🟦	🟦	🟦	🟦				🟦	🟦																18	0		
2	1		🟦	🟦	🟦	🟦	🟦		🟦	🟦	🟦	🟦	🟦	🟦	🟦		🟦	🟦	🟦	🟦	🟦	🟦		🟦	🟦	🟦		🟦			🟦	🟦	🟦	🟦	🟦					27	0	165	0
	2			🟦	🟦	🟦	🟦		🟦	🟦	🟦	🟦	🟦	🟦	🟦	🟦	🟦	🟦	🟦	🟦	🟦	🟦		🟦	🟦	🟦					🟦	🟦	🟦	🟦	🟦					26	0		
	3		🟦	🟦	🟦	🟦	🟦	🟦	🟦	🟦	🟦	🟦	🟦	🟦	🟦		🟦	🟦	🟦	🟦	🟦	🟦		🟦	🟦	🟦		🟦			🟦	🟦	🟦	🟦	🟦					28	0		
	4		🟦	🟦	🟦	🟦	🟦	🟦	🟦	🟦	🟦	🟦	🟦	🟦	🟦		🟦	🟦	🟦	🟦	🟦	🟦		🟦	🟦	🟦		🟦			🟦	🟦	🟦	🟦	🟦					28	0		
	5			🟦	🟦	🟦	🟦	🟦	🟦	🟦	🟦	🟦	🟦	🟦	🟦		🟦	🟦	🟦	🟦	🟦	🟦	🟦	🟦	🟦	🟦		🟦			🟦	🟦	🟦	🟦	🟦					28	0		
	6		🟦	🟦	🟦	🟦	🟦	🟦	🟦	🟦	🟦	🟦	🟦	🟦	🟦		🟦	🟦	🟦	🟦	🟦	🟦		🟦	🟦	🟦		🟦			🟦	🟦	🟦	🟦	🟦					28	0		
3	1						🟦			🟦	🟦	🟦	🟦			🟦	🟦		🟦	🟦	🟦	🟦	🟦	🟦	🟦	🟦	🟦			🟦	🟦									18	0	102	0
	2						🟦			🟦	🟦	🟦	🟦			🟦	🟦		🟦	🟦	🟦	🟦	🟦	🟦	🟦	🟦	🟦			🟦	🟦									18	0		
	3						🟦			🟦	🟦	🟦	🟦			🟦		🟦	🟦	🟦	🟦	🟦	🟦	🟦	🟦	🟦	🟦				🟦									17	0		
	4						🟦			🟦	🟦	🟦	🟦			🟦		🟦	🟦	🟦	🟦		🟦	🟦	🟦	🟦				🟦	🟦									16	0		
	5						🟦			🟦	🟦	🟦	🟦	🟦		🟦		🟦	🟦	🟦	🟦		🟦	🟦	🟦	🟦					🟦									16	0		
	6						🟦			🟦	🟦	🟦	🟦			🟦	🟦		🟦	🟦	🟦	🟦	🟦	🟦	🟦	🟦				🟦	🟦									17	0		
4	1		🟦			🟦	🟦	🟦		🟦			🟦	🟦	🟦	🟦	🟦				🟦	🟦	🟦	🟦			🟦		🟦											16	0	32	0
	2		🟦			🟦	🟦	🟦		🟦			🟦	🟦	🟦	🟦	🟦				🟦	🟦	🟦	🟦			🟦		🟦											16	0		
5	1				🟪			🟪				🟪								🟪				🟪			🟪				🟪				🟪				🟪	9	9	27	27
	2				🟪			🟪				🟪								🟪				🟪			🟪				🟪				🟪				🟪	9	9		
	3				🟪			🟪				🟪								🟪				🟪			🟦	🟥			🟪				🟪				🟪	9	9		
6	1			🟪	🟪	🟪	🟪			🟪	🟪		🟪	🟪			🟪		🟪		🟪	🟪		🟪	🟪	🟪		🟪			🟪	🟪	🟪	🟪						20	20	49	60
	2			🟪	🟪	🟪	🟪			🟪	🟪		🟪	🟪			🟪		🟥		🟥	🟥		🟥	🟥	🟥		🟥			🟥	🟥	🟥	🟥						9	20		
	3			🟪	🟪	🟪	🟪			🟪	🟪		🟪	🟪			🟪		🟪		🟪	🟪		🟪	🟪	🟪		🟪			🟪	🟪	🟪	🟪						20	20		
7	1			🟪	🟪	🟪	🟪	🟪		🟪		🟪	🟪	🟪			🟪	🟪		🟪	🟪										🟪	🟪	🟪	🟪	🟪					18	18	36	72
	2			🟪	🟪	🟪	🟪	🟪		🟪		🟪	🟪	🟪			🟪	🟪		🟪	🟪										🟪	🟪	🟪	🟪	🟪					18	18		
	3			🟥	🟥	🟥	🟥	🟥		🟥		🟥	🟥	🟥			🟥	🟥		🟥	🟥										🟥	🟥	🟥	🟥	🟥					0	18		
	4			🟥	🟥	🟥	🟥	🟥		🟥		🟥	🟥	🟥			🟥	🟥		🟥	🟥										🟥	🟥	🟥	🟥	🟥					0	18		
8	1					🟦				🟦			🟦				🟦			🟦				🟦				🟦			🟦			🟦						9	0	26	0
	2					🟦				🟦			🟦				🟦			🟦				🟦				🟦			🟦			🟦						9	0		
	3					🟦				🟦			🟦							🟦				🟦				🟦			🟦			🟦						8	0		
Tot div	*dense*		6	16	19	21	24	16	10	27	20	22	27	19	9	13	23	16	19	24	19	14	9	27	19	14	8	10	2	4	22	10	10	13	11	0	0	0	3				
	sparse		0	7	10	7	7	7	0	7	3	7	7	7	0	0	7	4	3	7	7	3	0	6	3	3	2	4	0	0	10	7	7	7	7	0	0	0	3				
Tot wiv	*dense*		86					141							124							101							72							3							
	sparse		31					38							28							21							38							3							

Legend	🟦 *dense*
	🟥 *sparse*
	🟪 *both*

FIGURE 2.2: Samples from the dense (blue label) and sparse (red label) culture. If both densities were present the label was coloured in purple. It is also reported the total number of samples in each culture and batch (horizontal summation) and the total number of samples in each DIV and WIV (vertical summation). The table starts from the third DIV because the earlier cultures did not show any activity that could be recorded using MEA.

These cultures belonging to the same batch contain genetically similar cells (though the exact similarity cannot be known) which reduces one source of variability. For this reason we will also try to classify the cultures according to the batch.
Different number of cultures means also different number of samples (i.e. recordings), an important parameter that one has to take into account when performing the classification. The organization and the number of the recordings are also well illustrated in the table 2.2. In fact, in figure 2.2, the blue and red squares represent the dense and the sparse samples, respectively (purple means that both types are present). In the table the samples are divided according to the culture and the DIV. In turn, the cultures are grouped in batches and the DIVs in WIVs. In addition, the total number per culture/batch/DIV/WIV of the recordings available in the dataset are reported. As it is possible to see from figure 2.2, starting form the third DIV, the authors recorded half an hour of spontaneous activity on most days. In dense cultures, cells typically began firing detectable action potentials around 4-5 DIV. Tonic firing persisted for lifetime of the culture, but network bursts emerged later, which dominated the activity throughout the rest of development. In the next section we will give further insights in the qualitative changes in the bursting activity, by reanalyzing the data from [55] and reproducing the majority of results reported in [55].

2.1.2 Qualitative Description of the Data

The development of the activity of a typical cultures passes through various stages, characterized by different degrees of burstiness, different burst shapes and size, and different distributions of burst intervals. In figure 2.3 (replicated from figure 3.A in [55]) a detailed classification of the burst type found in the recordings is reported. The figure is divided between dense and sparse cultures and samples belonging to the same batch are grouped together. Moreover, along the row the samples are ordered according to the culture age, showing how the activity changes during development. As indicate by black bars in figure 2.3, half of the medium was replaced approximately every five days in most experiments. In some cultures the entire medium was replaced every week to test effect of the feeding schedule on the activity. No significant differences were observed in the activity patterns with respect to the other preparations. From figure 2.3 is possible to notice at one glance the rich variability of activity in different conditions. The main objective of this thesis is to quantitatively analysed this variability and to understand which measure better describes (and discriminates) the various activity patterns that are affected by different factors, i.e., densities, ages and batches.

The dataset is characterized by a rich variability mostly due to the wide diversity in the network burst patterns shown among the cultures. As we will better describe in the Results, the quantitative details of the development of different cultures varied widely depending on the culture ages, density and batch. Indeed, cultures from different platings could show visible qualitative differences in the activity patterns during development. In the paper [55] the authors devised a classification of the recordings following criteria based on the NB features, which are briefly reported below. The first NB characteristic that the authors in [55] considered is the level of burstiness, that is, how many electrodes were involved in the formation of a NB. Thus, they classified the NB tiny if less than 5 electrodes were involved. If not classified as tiny, the NBs were classified according to other spatio-temporal patterns. Then, they looked at the NB size, i.e. the number of spikes contained within the NB.

According to this feature the recordings were labelled as fixed size, variable size and bimodal size. Moreover, the authors checked the property of the termination phase in the NB which is usually longer than the initialization. If most of the falling times of the recorded NB was prolonged by an extended period of several seconds during which several channel continued bursting, the samples were named long-tailed. Another important NB characteristic that shows high variability in the recordings is the NB rate. If the spacing between two consecutive NBs was not regular but shown a chaotic behaviour, the sample was considered highly variable.

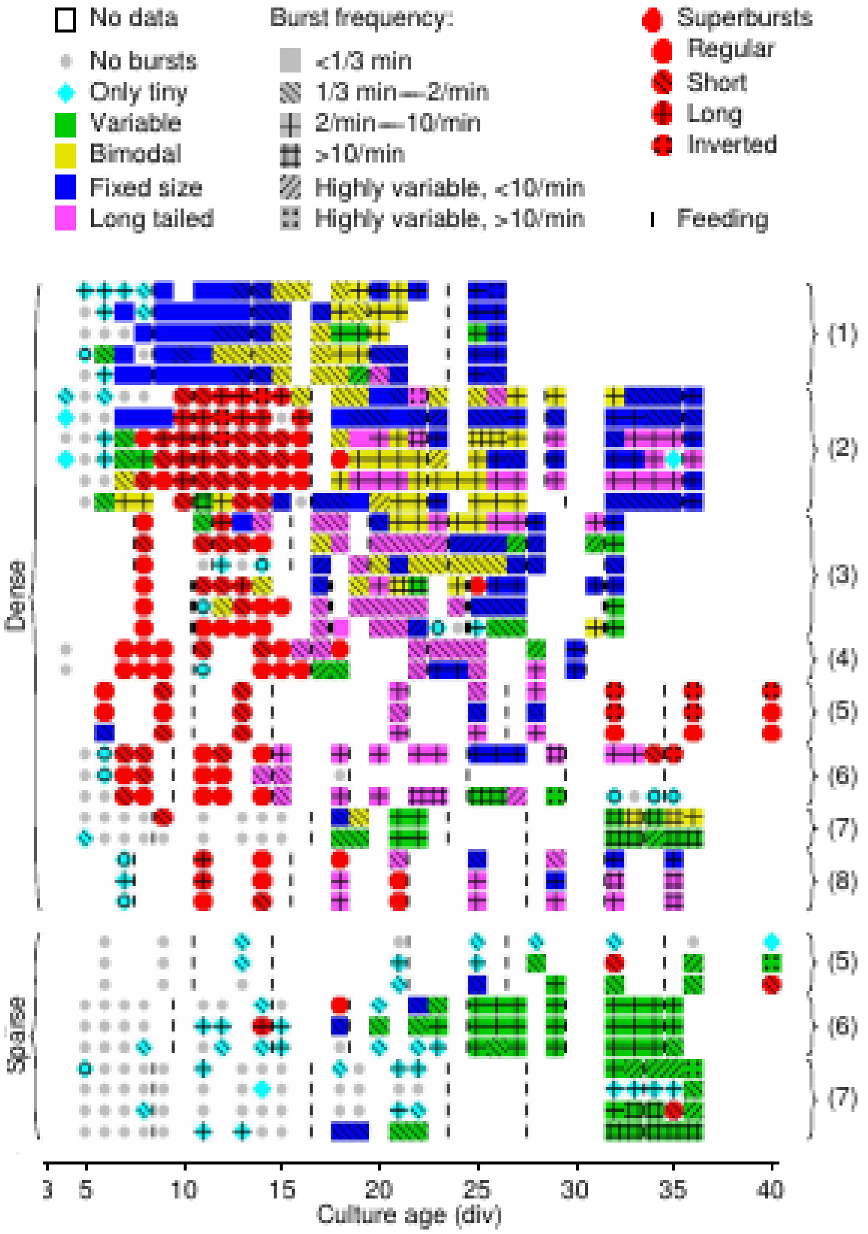

FIGURE 2.3: Overview of the different classes of bursting behaviour observed, according to shape, rate and superburstiness. The legend is reported in the upper part of the figure. The x-axis indicates the DIVs. The samples are grouped based on the density and the batch, the number in parenthesis. The black bars indicates the 'feeding time' of the cultures. Replication from Figure 3.A in [55].

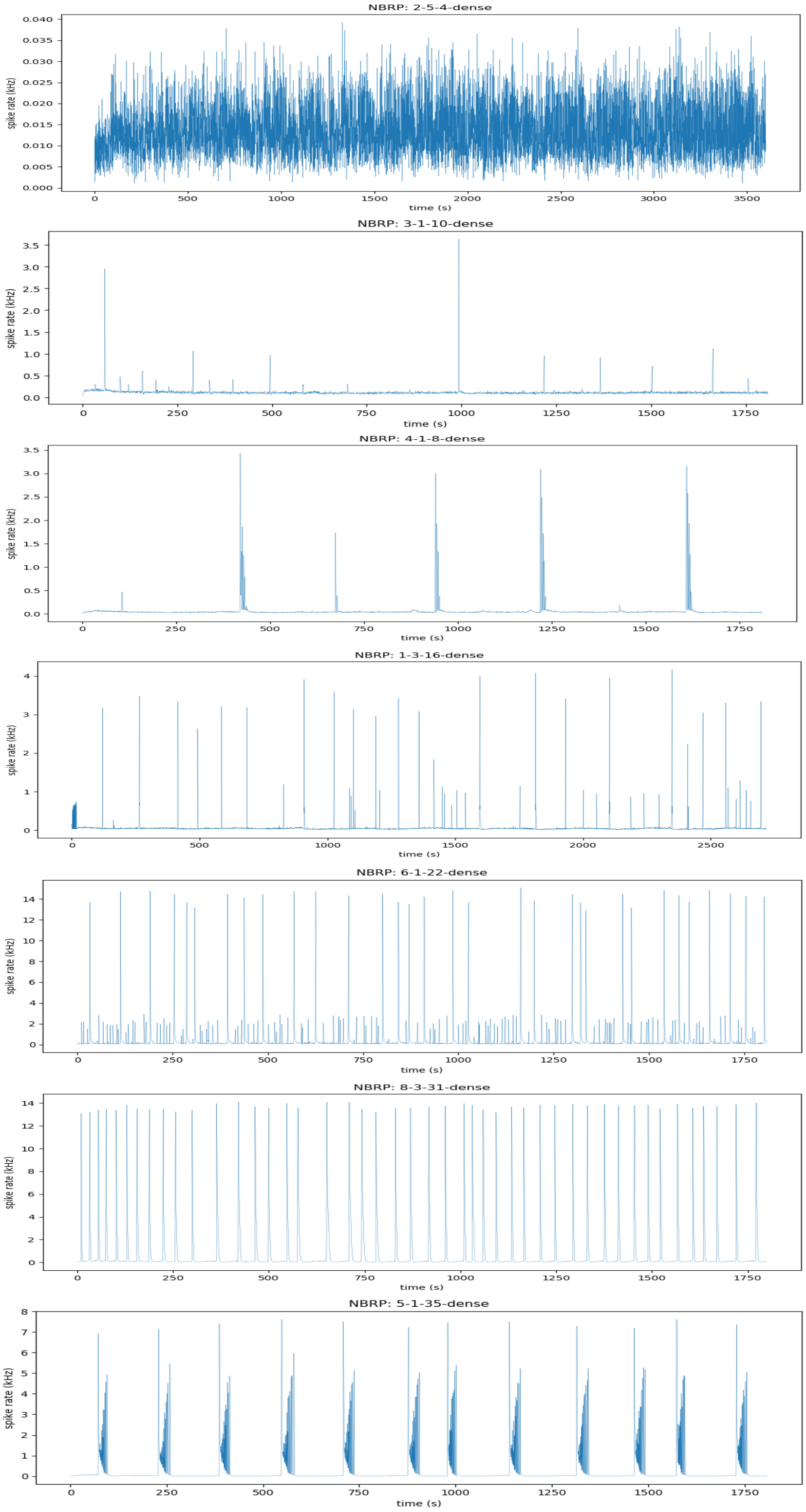

FIGURE 2.4: Examples of NB patterns at different culture ages visible from the rate profile (NBRP). All the recordings were taken from dense cultures. Starting from the upper plot, the spike activity does not show any NB (1st), then after some DIVs the NBs appear (2nd), sometimes in a superburst fashion (3rd). As the cultures keep developing, they show more pronounced NBs (4th) but they can still present some small NBs (5th). When they are mature the activity is made mostly by high-rate NBs (6th) or sometimes in elder culture inverted superbursts could appear (7th).

Finally, one pattern that appears in around half of the recordings was the superburstiness, a second order of activity organization when network bursts occurred in short, sharply defined trains. This particular type of activity is usually observed in early ages (first 2 WIVs). This phenomenon occurred when within a NB the maximum firing rate shows several peaks (see the third plot in figure 2.4). The recordings showing superbursts were classified according to the number of firing peaks within the superbursts. They were labelled regular, short and long superbursts if the number of bursts were highly conserved, variable but less than ten, variable with higher average, respectively. If the maximum number of spikes increased in the successive network bursts, as in the older cultures (after 30 DIV), the shape was considered inverted (see the last panel in figure 2.4).

From now on, following the numeration in [55], the samples will be labeled with three numbers, e.g. 5-1-35, indicating the batch, culture and the DIV, respectively. In what follows we will briefly describe how the NB patterns generally evolve during the first five WIVs checking at the network burst rate profile (NBRP), i.e., the trend of the spiking frequency across the time in one recording. NBRP reflects the spiking activity across the entire culture and integrates the activity from all electrodes, thus, including both spatial and temporal averaging. We will consider only dense cultures because they show a richer spectrum of patterns. However, usually the sparse cultures just had a delayed appearing of the pattern activity with respect to the dense counterparts. For instance, network bursting usually began after 5-7 DIV in dense cultures, and later in sparse cultures, after the second WIV. NB patters changed with culture age, and these changes were still ongoing after 30 DIV. Even between batches of the same density large differences existed both in terms of development speed and in terms of the type of burst. In the figure 2.4 some examples of NBRPs in some DIVs covering all the 5 WIVs of recordings are reported. The figure gives a simplistic glimpse of how cultured neural networks can change NB activity patterns during the development, passing from no detected NB to a superburst patterns. Specifically, after a WIV the first low-frequency NBs started appearing and in some batches they have been recognized as superbursts. In the third WIV the NB activity shown higher and irregular activity, both in frequency and intervals. In the fourth WIV the NB maximum firing rate kept increasing but some smaller NBs were still present until the last DIVs of the same week, when a more high-frequency regular activity occurred. At the fifth WIV some cultures shown also inverted superburstiness.

2.2 The Analysis Pipeline

In the following paragraphs all the steps of the analysis performed in this work are described in detail. It starts from the preprocessing and then it goes through the burst detection method. The machine learning techniques used in the last part of the analysis are also reported at the end of this section. Although we did not follow the actual order of the workflow in the description, due to the importance of the measures extracted in the analysis, they are reported separately in the last section of this chapter. The diagram shown in figure 2.5 schematically illustrates the main steps of the pipeline in the right order they occurred in the analysis. It should be stressed out that the last step also contains the subsampling analysis, where the classifications were repeated both shortening the recordings and removing the spiking activity of some electrodes.

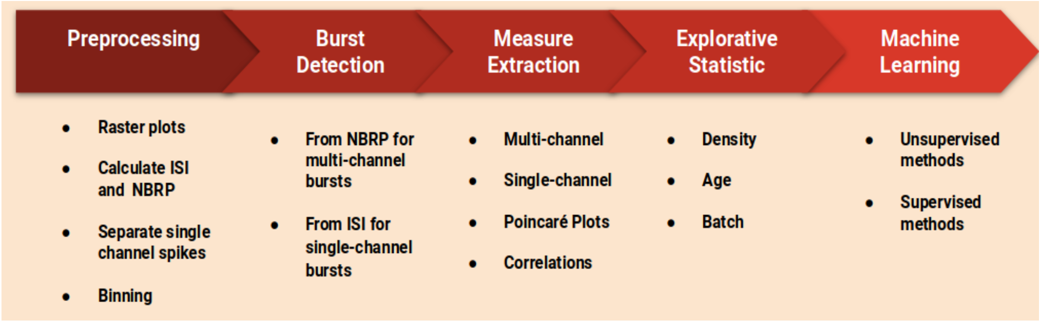

FIGURE 2.5: A simplified scheme of the pipeline. All the steps will be further explained in the next paragraphs.

2.2.1 Preliminary Steps

This step is not actually a preprocessing of the data since the samples are already in form of spike time-stamps with their respective channels. In this step the data were undergone to just some preliminary elaborations to facilitate the next analysis.
Firstly, in order to have an idea of how the recordings look like, it is important to check at the **raster plots**. This is a graph where all the spikes are represented in point-like form ordered across the recording duration. In each row are reported the spikes of a single electrode. This type of representation permits to see the synchronization of the electrodes at once. An example of raster plot is given in figure 2.6, where it is clearly possible to see the NBs . The spikes, represented by blue points, are placed more closely both in time and in space in the typical synchronized pattern of the NB. For this reason these plots will be used for testing the goodness of the burst detection, taking advantage of the clear visibility of NBs when the density of the points is higher than the baseline spiking activity.

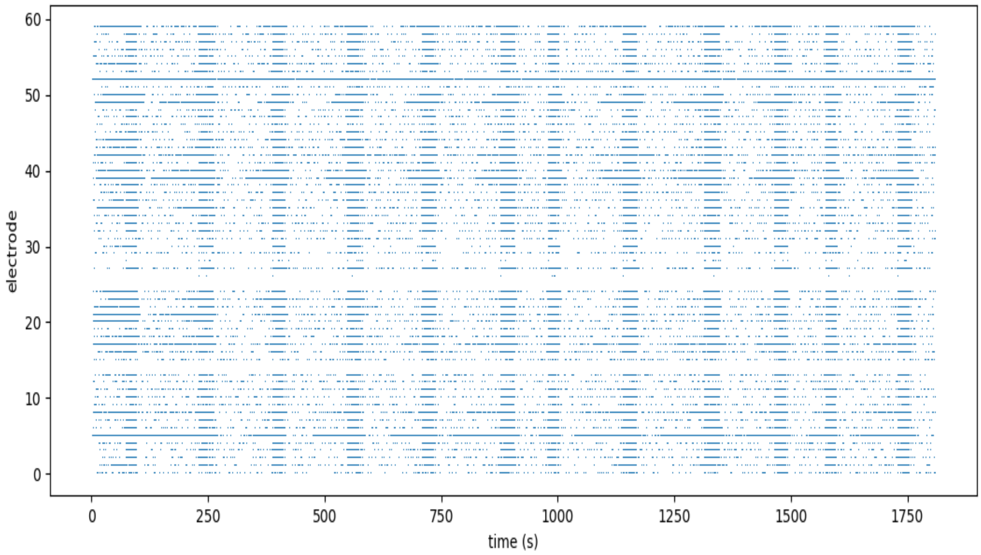

FIGURE 2.6: Example of raster plot taken from culture 5-1-35. The blue dots represent the population spikes, the x-axis the recording time and the y-axis the channels.

Although the raster plot is useful to test the burst detection, this procedure is performed starting from the **Network Burst Rate Profile** (NBRP) , an overall measure of the instantaneous global activity. We calculated the NBRPs using the definition given in [49]. The NBRPs were calculated by smoothing the spike counts in the bins via convolution with a Gaussian kernel. In literature, as in [55], the NBRP is also called array-wide spike detection rate (ASDR). Working with the NBRP is much better than working with the entire spiking recordings because it merges in a one-dimensional time series the properties of a multi-channel activity. Hence, it reduces the number of points to work with, making possible to use simpler univariate statistics. In order to calculate the spike counts we needed to bin the recording using a proper bin width, neither too short nor too long. In the latter case, when the time resolution is too low, one could not catch the right overall rate; in the former case, if the time binning is shorter of the time delay due to the signal transmission speed between the neurons, it is possible to come out with misleading results. Therefore, in order to obtain the maximal time delay one needs to find a lower bound for the velocity conduction in rat neuron cortex and the diameter of the MEA device (i.e. the maximal distance between the electrodes). From the literature [29, 28] the neuronal conduction seems to be not lower than 0.5 m/s and from [55] we know that the maximal MEA dimension is 1.72 mm so, with a straightforward calculation, the maximal time delay is 3.44 ms. Therefore, after some visual inspection of several NBRPs taken from different culture conditions, we concluded that a proper value for the time binning is 50 ms, a value that is high enough to avoid unwanted delaying effects and small enough to capture well the overall spike frequency, avoiding all the setbacks mentioned above. Moreover, this value is also used in other studies, as in [57]. Then, the spike count in each bin is divided by the bin width and by a factor of 1000 to obtain the spike frequency in kHz. The value averaged across the entire recording is called the overall firing rate (OFR) and this measure will be used for reproducing some results in [55]. Finally, in order to get a smooth curve a Gaussian kernel, with a standard deviation of 5 bin steps (SD=5) is applied. Some examples of NBRPs are illustrated in figure 2.4. As it will better explained in the next section, the spiking activity peak overcoming a certain threshold indicates a NB.

In this step, **Inter-Spike Intervals** (ISI) are also calculated, namely, the time intervals between each pair of consecutive spikes taken from all the channels. The ISIs are going to be used as a measure of the neural activity. Nevertheless, ISI can be used also in the burst detection as it will be illustrated in Section 2.2.2.

Furthermore, the recordings are split in their respective electrodes, that is, instead of having the spikes of all the electrodes ordered in time, they are also ordered, and binned, with respect to their recording channels. In other words it was calculated a matrix where the row indicated the electrodes and the columns the recording times, or if binned, the spiking frequencies. The **binned spiking matrix** will be useful when the multivariate measures will be computed (see Section 2.3.3).

2.2.2 Burst Detection

There are several methods for detecting the bursts and network bursts [2, 7]. In this work two methods were compared, one based on the ISI and the other on the NBRP. Both are different from the method used in [55]. In [55] the NBs were detected using the SIMMUX algorithm. Briefly, each electrode trace was searched for burstlets: sequences of at least four spikes with all inter-spike intervals less than a threshold (set to 1/4 of that electrode's inverse average spike detection rate, or to 100 ms if the

electrode's average spike detection rate was less than 10 Hz). Any group of burstlets across several electrodes that overlapped in time was considered a NB.
The burst detection method based on **ISI** tested in this work followed the implementation used in [49]. Spontaneous NBs were detected according to the following criteria:

- the first ISI < 100 ms defined the onset time of the NB;
- the first ISI > 100 ms defined the offset of the NB;
- a minimum of 10 electrodes must be active during the NB;
- a minimum of 10 spikes must be recorded per NB.

The ISI threshold was set at the fix value of 100 ms but it can be found also in a self-adapting way. The algorithm presented in [34] is based on the computation of the logarithmic inter-spike interval histogram and automatically detects the best threshold to distinguish between inter- and intra-burst spike intervals. However, it turned out that this approach is not easily applicable with all the experimental conditions we analysed, as for example sparse or early DIV cultures. In fact, the minimum of the logarithmic inter-spike interval histogram was not always easily defined and many visual inspections were needed. This induced our decision to adopt a simpler method.

Instead of using the spike times, an alternative method consists of detecting burst according to the spike frequency, that is, looking at the **NBRP**. The idea of the algorithm is rather simple: each peak in the NBRP above a certain threshold is interpreted as a NB. Nevertheless, it is not that straightforward because there are several issues to deal with. In the following paragraph it is briefly explained how the algorithm works, and it will be compared with the ISI-based method, justifying our final decision to adopt this method.
Initially, the peaks are detected using different thresholds, set according to the NB frequency. For each kind of NB also a different minimal distance between the peaks (d), a minimal width of the burst, i.e. the time length (w), and the relative height parameter (h) were set. Specifically, the NB peaks were classified in 4 categories:

- Ultrahigh burst: frequency peak higher than 10 kHz (d=0.5 s , w=0.5 s, h=0.98);
- High burst: frequency peak from 5 to 10 kHz (d=0.5 s , w=0.5 s, h=0.95);
- Middle burst: frequency peak from 1 to 5 kHz (d=0.25 s , w=0.35 s, h=0.85);
- Low burst: frequency peak from a variable low threshold to 1 kHz (d= 0.25 s, w=0.25 s, h=0.60).

The lower threshold is not fixed because for detecting small bursts more caution is needed. The detection of tiny bursts strongly depend on the baseline activity, calculated as the average spiking frequency, because the rate within a burst should be higher than the overall activity. In this way it is possible to detect small bursts in different conditions, both for low activity in early DIV or sparse cultures and in high activity of older dense cultures. However, below 0.1 kHz the bursts are discarded. From 0.1 kHz to 0.5 kHz, the rate was divided in 4 steps of 0.1 kHz width and for each range a different threshold was set. This division was mostly done in order to find a proper peak width. In fact, for each type of burst was used a different relative height parameter, that is, the distance from the peak and the peak ground, from which the width was calculated. The smaller values for lower peaks were chosen to not include into the NB too many noisy spikes, avoiding a broader width not justified from visual inspection of the raster plot. On the other hand, the width for high and sharp peaks has to be calculated close to the base of the peak because in this case the spikes are better clusterized within the burst and less border noisy spikes were visible in the raster plot.

Using this method, it can happen that when detecting two close peaks their widths **overlap**, as in the figure 2.7 where the case of a superburst is shown. To avoid this drawback this burst detection algorithm deletes the peaks with lower height, considering the overlapping NBs as a whole bigger NB with the MFR of the higher peak.

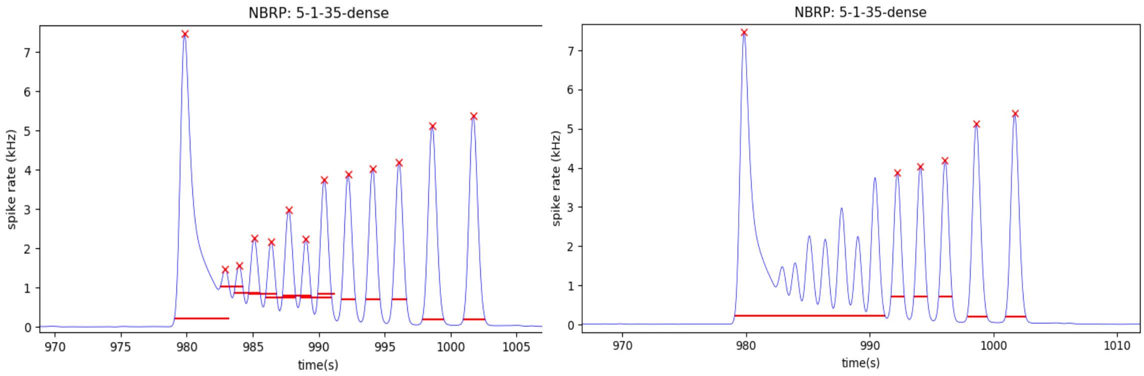

FIGURE 2.7: The plot on the left shows an example of peak overlapping and the plot on the right the peak detection after the correction. The figure illustrates the case of a superburst in a dense culture (5-1-35). It has to be noticed that burst detection on the right plot is not completed because in a superburst the smaller bursts are merged in just one burst.

Once the peaks are detected, some post-processing steps are also included in the algorithm. From visual inspection in the raster plots of the right borders of NBs, the offsets, we noticed that the detected offsets often cut the NB tail. Hence, the offset was shifted a little bit on the right, proportionally to the width and the height of the peak. Moreover, the left border of the NB (onset) often included more spikes that actually present in the raster plot, maybe due to the smoothing step in NBRP calculation. Also in this case, the onset was moved closer to the peak proportionally to the width and the peak height. The figure 2.8 shows the results of this **borders correction**. The upper plot is without correction, with the tails cut and with the onsets that include spikes which seem not to be part of the NBs. The lower plot shows the effect of the borders correction: the onset is closer to the beginning of the NB and the offset is moved further away to include more spikes within the NB. This correction is also motivated by the usual NB shape described in literature (cfr. Section 1.3.2 where it is described the spontaneous neural activity during development), characterized by short abrupt onset and a long tailed offset, at least for mature cultures.

Then, it was applied a further post-processing correction, namely, **merging** NBs separated by a really tiny time interval. This correction it was useful when small NBs where detected close to each other, in particular in the case of superbursts in young cultures when small NBs are nearly located. Or when a small NB is close to a bigger NB and it can be incorporated by this one (figure 2.9). This is also the case of

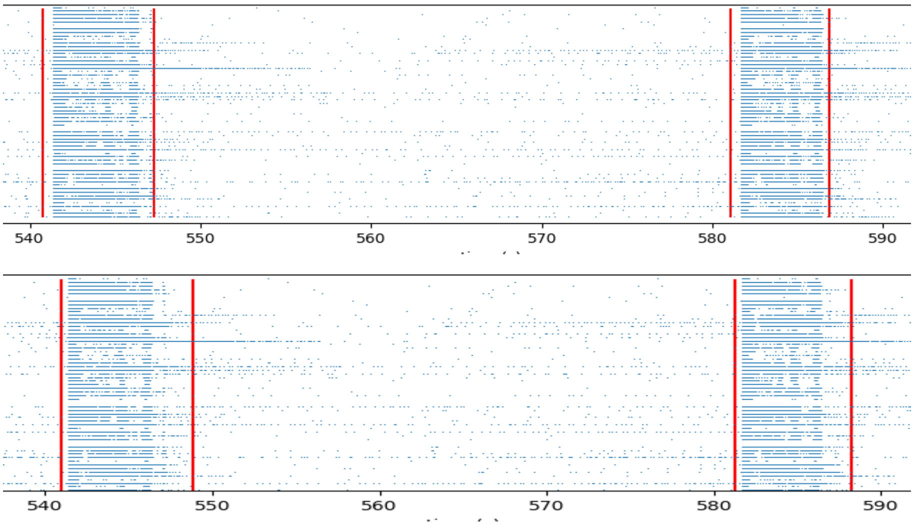

FIGURE 2.8: Example of border correction. The upper plot shows the onset and the offset detected in two NBs in a mature dense culture (6-1-32) without correction (red lines). The plot below shows the correction, both the onsets and the offsets are shifted on the right.

the inverted superbursts in older cultures (see figure 2.7) when few smaller NBs are placed after a bigger one at the beginning. Therefore, this *a posteriori* correction was mainly thought for not splitting a superburst in many smaller NBs.

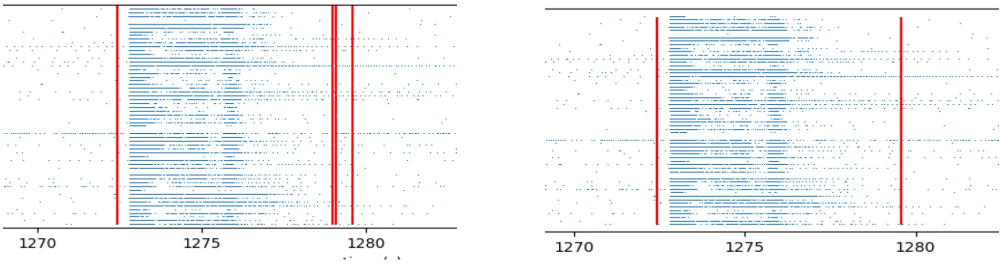

FIGURE 2.9: Example of merging correction. The left plot shows the onset and the offset detected in a NB in a mature dense culture (6-1-32) without corrections (red lines). The right plot shows the correction, as the small NB is incorporated in the bigger one.

In the next three figures some of the **pros and cons** of both methods are shown. The upper plots with the green lines report the results of the ISI method while the lower plots with the red lines show the NBRP method. In figure 2.10 an example of border comparison shows how usually the ISI-based method detect more neat NB borders. Figure 2.11 illustrates the overcounting of tiny NBs in ISI-based method and figure 2.12 shows how the ISI-based method could incorrectly detect big NBs in high-frequency baseline activity.

In general, the NBRP-based method is quite fast and accurate in detecting NBs but it has also some throwbacks, making the ISI method more suitable; for example:

- even with the adapting low threshold, sometimes it discards tiny NBs, in particular in samples that show high average activity or irregular bursting;
- it needs a lot of parameter tuning while the ISI method has only three free parameters;

- even with the border correction sometimes it does not detect perfectly NB tails, in particular when the NB show a long falling time (figure 2.10) .

On the other hand, the ISI method presents also some issues and it makes the NBRP-based method more appropriate. In the following bucket list its main disadvantages are listed:

- The ISI-based detection is more time consuming due to the enormous number of spikes usually detected from these neural cultures.
- Sometimes it counts as a NB very little cluster of spikes, as for example in low activity recordings it detects quite many NBs not detectable by visual inspection (overcounting) as it is shown in figure 2.11.
- In high baseline activity the method tends to undercount the NBs because it merges them. It detects also NBs lasting several minutes because it is not able to recognize the pause between two consecutive NBs. Moreover, it can detect a NB with a too long onset (see figure 2.12). This case can degenerate in a erroneous burst detection in elder culture when the spiking activity shows a really high frequency baseline.

These issues, as the undercounting and the overcounting, make the method not really reliable and it would need to be improved. This can be done by changing the parameters or adding a post-processing algorithm. The previous bucket lists are summarized in Table 2.2, that shows the pros and cons of the two methods.

	ISI	**NBRP**
border detection	✓	✗
number of parameters	✓	✗
small bursts in low activity	✗	✗
small bursts in high activity	✗	✓
computational time	✗	✓

TABLE 2.2: Summary of the pros and cons of ISI-based and NBRP-based detection methods. The check mark means that the methods behaves well, conversely the cross mark means that the method shows some issues.

Both the methods are not perfect and they need fine-tuning of parameters, post-processing and visual verification of the results. As Cotterill and Eglen already stated in [7], so far there is no ideal burst detection method that can be adapted for any kind of data. However, an alternative might to merge the two methods combining the positive aspects of the two. For example, taking the NB counting through frequency peak method and the borders detection from the ISI-based method. However, this could be too computationally demanding and after all the NBRP seems to be more suitable for the scope of this thesis. The main issues in the NBRP-based method is the NB border and the tiny NBs detection. However, these errors do not occur that often and they are relatively small so they should not affect the next analysis. Moreover, these errors are distributed equally in all the detected NBs and averaging out the measures over various samples, they should not create any bias in the outcomes.

The choice of using the NBRP-based method for detecting the NBs and the ISI-base for detecting the burst in the one-channel spiking activity is also in agreement with the guideline reported in [2], a comprehensive study of the burst detection methods.

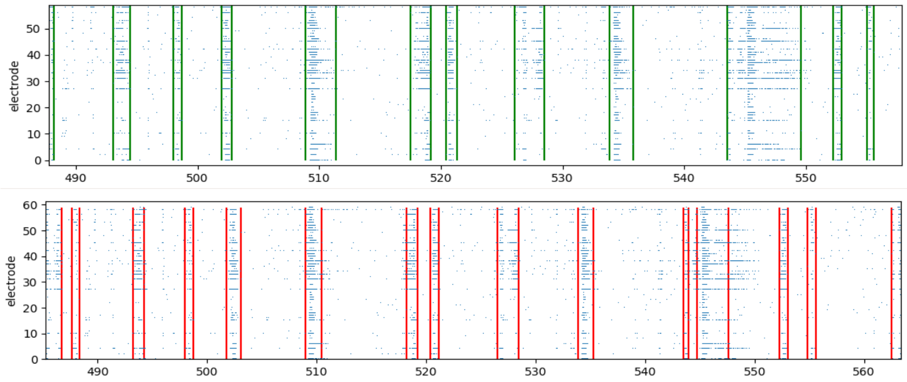

FIGURE 2.10: In this figure is reported an example of the border detection with the ISI-based (green lines) and the NBRP method (red lines). Usually the ISI-based method detects more accurate onsets and offsets even if exceptions were founded.

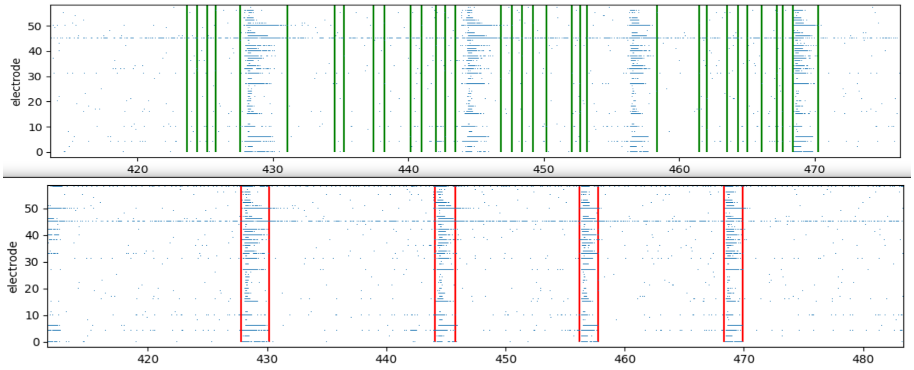

FIGURE 2.11: In this figure is reported an example of the tiny NBs detection with the ISI-based (green lines) and the NBRP method (red lines). Usually the ISI-based method tends to over-detect really small NBs, although sometimes the NBRP seems to discard many small NBs.

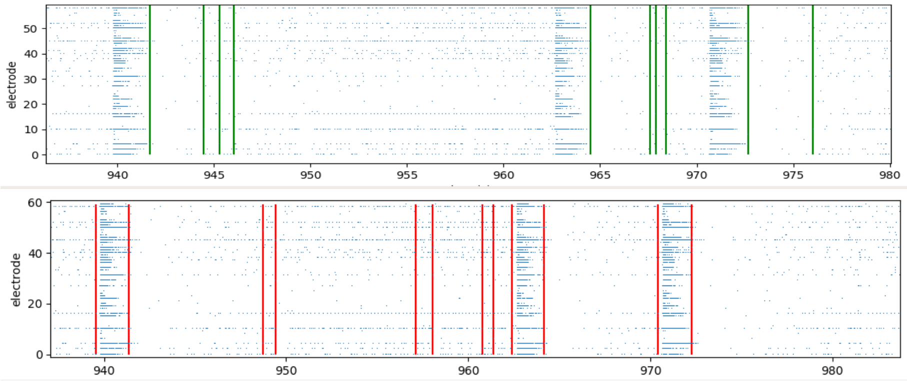

FIGURE 2.12: In this figure is reported an example of detection in the high baseline activity with the ISI-based (green lines) and the NBRP method (red lines). When the overall activity is high the ISI-based method detect really big NBs because it cannot distinguish the rate increasing due to a NB from the baseline.

2.2.3 Machine Learning Techniques

Now we will skip to the last pipeline step, that is, the machine learning techniques used in the analysis. Then, we will reserve the entire last section of this chapter for an in-depth description of the measures used to quantitatively characterize the data variability.

Machine learning is a cutting-edge research field at the intersection of statistics, artificial intelligence and computer science that allows to extract knowledge from raw data.

In this work we will use some methods from supervised and unsupervised learning with the final aim of classifying neural network activity recordings. We believe that these methods are suitable for dealing with the rich complexity of the biological data, making them a proper tool for testing the robustness of a wide range of measures. For more details about machine learning and useful Python implementation with Sklearn package refer to the textbook [31].

The **principal component analysis** (PCA) is one of the most used dimensionality reduction method. PCA orthogonally transforms the feature space into a set of linearly uncorrelated variables, called principal components, in such a way that the first principal component has the largest variance. In order to perform dimensionality reduction, the first 2 or 3 new features (principal components), the ones with more information contents, are selected for visualizing the dataset. However, the new axes do not correspond to the original feature space axes as they are usually a linear combination of them.

Dimensionality reduction is used to create a more understandable representation of the data, compressing an high-dimensionality dataset into two- or three-dimensional feature space. The reduced space tries to keep most of the information, making it an ideal procedure for inspecting visually the data contents. If the number of features is not that high one could visualize pair plots. However, some interesting aspect of the data could be revealed only by their global interaction. Thus, this method is often used in exploratory or preprocessing steps before applying more precise supervised algorithms.

In the unsupervised learning the right output is unknown so the knowledge has to be automatically extracted from the data. An example of unsupervised learning used here is the clustering, a group of algorithms which try to split the data into clusters according to some intrinsic property of the data (e.g. their spatial disposition in the feature space) without knowing the right class label of the samples. In this sense, clustering may be thought as a classification without *a priori* knowledge about the labels.

One of the simplest and more popular algorithms is the **K-means clustering** which is based on two main steps: assigning each sample to the closest cluster center and then setting a new cluster center as the mean of the data points belonging to that cluster. The initial centers are assigned randomly. The algorithm stops when changes are no longer reported (figure 2.13). K-means can only detect simple shapes as the cluster is just defined by its center, it assumes that the clusters have almost the same size and all the directions have the same importance. These properties will affects the unsupervised classification outcomes as we will discuss in Results.

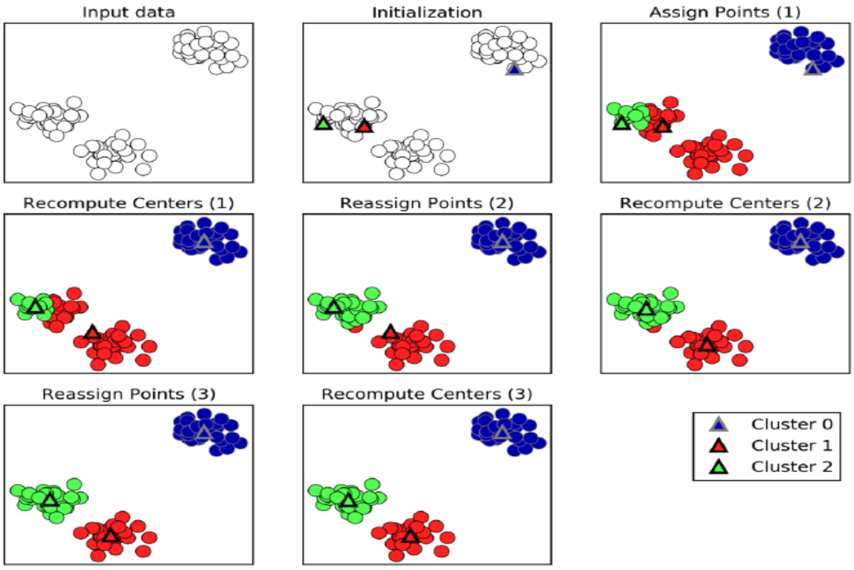

FIGURE 2.13: Input data and three steps of the k-means algorithm. Example taken from [31].

As it will be explained in the next section, we also used the **agglomerative clustering**, an algorithm that starts with the simplified assumption that each point represents a cluster and then merges two similar clusters until a stopping criterion is satisfied. Since we wanted to find the number of clusters, we set a distance threshold as a stopping criterion, that is, the linkage distance threshold above which clusters will not be merged anymore. This value was found as the maximum diameter of the dispersed data points in the feature space (see Section 2.3.2). The ward linkage was set as a similarity rule, i.e., two clusters merge when the variance within all clusters increases the least. This algorithm often leads to almost equally-sized and simple-shaped groups, and it was suitable with the type of clusters we were trying to find.

The supervised counterparts attempt to predict a certain outcome given the input/output pairs from which the algorithm can learn. As the true labels are available, this type of methods are more powerful than the classification based on the unsupervised learning. After the initial training the **supervised algorithm** should be able to make accurate prediction with new unlabelled data. In this work we only implemented a supervised machine for performing classification because our aim was to predict a discrete number of class labels, e.g., dense/sparse, different WIVs and batches. The main goal of a classification algorithm is to generalize from the training set to the test set (that should be made by different data), being careful to not build a too complex model that fit too closely the training set, an issue called **overfitting**. Conversely, **underfitting** problems are met when choosing a simple model that is not able to be accurate on test data. Therefore, in order to find a good trade-off between overfitting and underfitting, selecting the right model complexity is often a delicate task. However, a rule of thumb is that the model complexity depends on the size and variability of the dataset. **Data augmentation** is a popular technique that can be really useful when few samples are available to train the model so it can be helpful against overfitting issues. As we will better discuss in Chapter 3, to overcome the problem associated to a limited amount of data, we generated synthetically more samples by splitting in equal parts the recordings.

Another way to assess higher generalization performance is by **cross-validation**, a statistical method for a more optimized and robust splitting of the data into training and test set. In k-fold cross validation, where k is the number of equal-sized partitions or folds, the data are split k times. Each time a partition is left for testing the model that is trained with the remaining k-1 folds. In this way all the samples are used at least once for training the model, improving the generalization and consequently the classification accuracy. However, the computational cost increases if a large dataset is used. To make the splitting even more efficient and the estimations more reliable, we implemented stratified cross-validation, where in each fold the proportion of the classes is the same of the whole dataset, as illustrated in figure 2.14. In our implementation the number of fold was set to 5 due to the limited amount of samples.

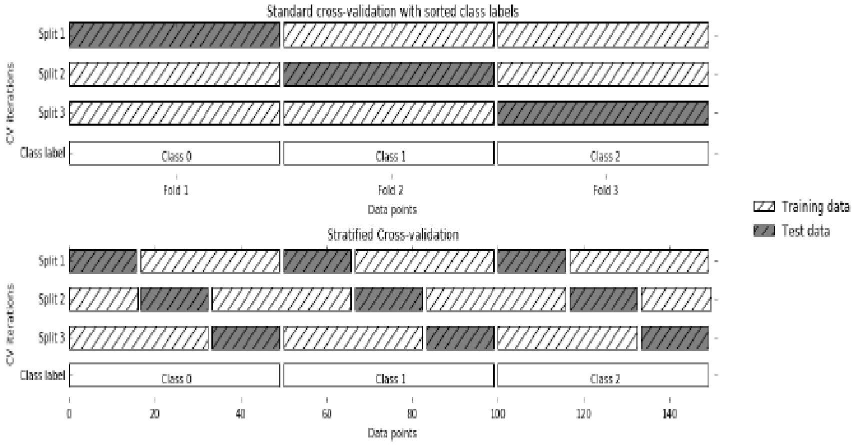

FIGURE 2.14: Comparison of standard cross-validation and stratified cross-validation when the data is ordered by class label. Image taken from [31].

In this thesis we implemented a supervised classifier based on **Random Forest** (RF), an algorithm that was first created by Ho in 1995 [51]. This algorithm is based on **decision trees**, hierarchical partition models where at each test the feature space is split along one axis. The partitioning is repeated recursively until each region, called leaf, contains a wanted target. The region gets the label of the more numerous target that lies inside. If all the samples in that region belong to the same class the leaf is called pure. Usually building a complex model that yield to pure leaf may overfit the training dataset, unless it is quite homogeneous. Hence, stopping the partitioning process earlier, or merging leaves containing little information, could prevent overfitting issue. In our case we used the sklearn in-build method left with the default parameters. Thus, the algorithm did not stop until all pure leaves were obtained. We made this choice because we had few samples and the overfitting issue was already prevented by averaging over many decision trees (number of estimators set at 200), as it will be better described later.

In our implementation the metrics used for spitting the data to test the homogeneity within the subsets is the Gini Impurity, an index that quantify how often an element from the set would be incorrectly labelled if it was randomly labelled according to the distribution of labels in the subset. Decision trees permit also to calculate the **relative feature importances** which score the contribution of each feature in partitioning the data, assigning a number between 0 and 1, the worst and the best score, respectively. However, if a feature has a low feature importance, it does not mean that it is uninformative but more likely that another feature encodes the same information.

Apart from being a model that can be easily visualized, the algorithm is invariant to scaling of the data so it does not need preprocessing steps, as normalization. However, the decision trees on their own tend to overfit so, if the generalization performance has to be improved, they should be used in ensembles, as in RF. In fact, building many decision trees the amount of overfitting is reduced by averaging each single tree's result. The averaged outcome provides a more faithful picture of the data making the RF a powerful method, although can be time consuming if the dataset is large. The higher robustness of the RF outcomes is guaranteed because each tree is randomized by selecting a part of the data points (bootstrap sampling) and of the features. Averaging between more decision trees leads to less overfitting, provides more smooth decision boundaries (see figure 2.15), and more reliable feature importances. We tested the classifier, calculating accuracies and feature importances, with the original dataset and different subsampled versions, both temporally and spatially.

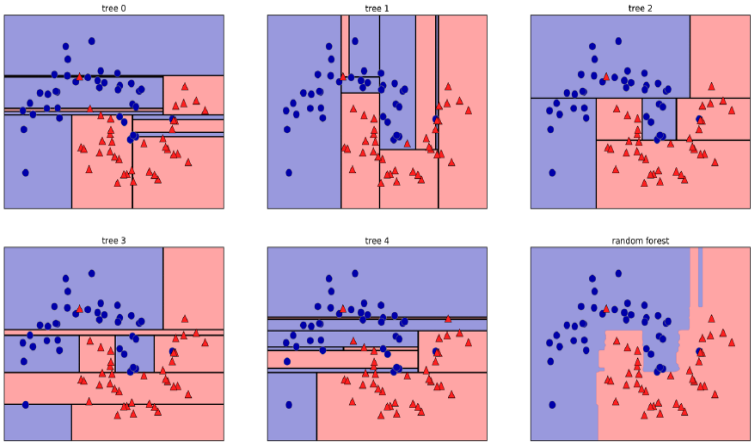

FIGURE 2.15: Decision boundaries found by averaging the predictions of five randomized decision trees. Image taken from [31].

2.3 Measure Extraction

After the network bursts were detected, measures were extracted to characterize the neural activity of the cultures. Afterwards, using the machine learning techniques explained in the previous section, they will be used in a classification task to see which one has the best discriminatory power when dealing with the data's intrinsic variability. This section reports the description of all the measures extracted, explaining both the theoretical background and the procedure of calculation adopted for our recordings. In literature we found an extensive list of measures that attempt to describe in a precise manner the spatiotemporal properties of the neural network dynamics.

MULTI-CHANNEL MEASURES		
Network Burst	**Population Spike**	**NBRP**
Burst Rate	OFR	Autocorrelation 1st Minimum*
Burst Length	ISI CV	First Harmonic*
Falling Time		Mutual Information*
Rising Time		Correlation Dimension*
Maximum Firing Rate		Lyapunov Exponent*
Burst Size		
Active Electrode		
Recruitment Speed		
Burstiness		
Peaks Within Burst*		
Superburstiness*		
IBI CV		
IBI Eigenvalue Ratio*		
IBI Clusters*		
IPI CV*		
IPI Eigenvalue Ratio*		
IPI Clusters*		

SINGLE-CHANNEL MEASURES		
Univariate		**Multivariate**
Burst	**Spike**	**Correlations**
Burst Rate	OFR	Synchrony
Burst Length	ISI CV	Fano Factor
Burst Size		Pearson (entire recording)
Firing Rate within Burst		Pearson (sliding window)
IBI CV		Mutual Information
Bursting Electrodes		Van Rossum Distance
Burstiness		Spike Time Tiling Coefficient

TABLE 2.3: Table with the multi- and single-channel measures extracted from the MEA recordings. For each division we made subgroups (the columns) based on what the measure describes, e.g. NB, burst, spike, NBRP or correlation. Moreover, we divided the measures according to the technique they were extracted with. In black are reported the measures calculated with standard methods, in blue the measures extracted using Poincaré plots and in red the correlations. The asterisk indicates the novel measures. Abbreviations: OFR - overall firing rate, ISI - inter-spike interval, IBI - inter-burst intervals, IPI - inter-peak interval, CV - coefficinet of variation.

In this work we selected a group of heterogeneous measures, covering a huge spectrum of types, as reported in Table 2.3. Computing all the measures we found in literature is out of the scope of this thesis, also because many of them are quite similar and correlated, as they describe similar property of the neural activity, so likely they will not add information in the classification task. Moreover, some of the measures are not easy to implement because they were used for different kind of recordings, with different conditions or culture preparation (e.g. different neural cells). Thus, the adaptation for this dataset is not straightforward to implement.

Therefore, we selected measures taken from different techniques (Standard, Poincaré Plots, Spike Train Synchrony) that try to describe the most comprehensive spectrum of the activity (single spike, population spike, burst, NB, NBRP, correlation) and they were classified according to these properties (see Table 2.3). Specifically, the first division starts from the origin, that is, if the recording comes from all the MEA electrodes or just one single electrode, i.e., multi-channel (MC) or single-channel (SC) measures, respectively. In the former case a measure is chosen according to which neural network activity to characterize: the NB, the overall spiking activity or the NBRP. In the latter case two possibilities are met: the univariate case, where it is possible to use almost the same measures of the MC recordings for describing the spike and burst patterns, and the multivariate case, where the inter-correlation between the electrodes activity is described. The Table 2.3 illustrates a total of 40 measures, divided in 24 MC and 16 SC. Half of the MC measures were not found in the literature we are aware of so they were marked with an asterisk.

This section illustrates the measures dividing them according to the technique used, that is, standard method, Poincaré plots and spike train synchrony.

All the measures were extracted by means of a custom-made software developed in Python 3.7.5, implemented with the usual scientific computing libraries NumPy, SciPy and MatPlotLib. Some methods, in particular the ones related to the machine learning analysis, were taken from Sci-kit Learn package.

2.3.1 Standard Measures

In this section the 'standard' measures are illustrated. With standard are meant the more intuitive and biological features regarding the firing rate, the NB shape, and all the spatial and temporal properties that could characterize the bursting and the spiking activity of a neural network recorded via MEA. These measures are quite widespread in the literature; for example, an exhaustive list can be found in [49, 47, 8].

Let us begin describing the measures related to the NB shape which can be calculated from the Network Burst Rate Profile (NBRP), computed by smoothing the spike counts in the bins, via convolution with a Gaussian kernel (see Preliminary Steps, Section 2.2.1). From figure 2.16 is clear how to calculate the **Maximum Firing Rate** (MFR) within the NB, i.e. the peak of the NB profile that indicates when the NB reaches its maximum firing activity. As far as it is concerned the duration of the NB, it is possible to determine three features:

- **Rising Time** (RT) , the time between the burst onset and the peak of the burst profile;
- **Falling Time** (FT) , the time between the NB peak and the offset;
- **Burst Length** (BL) , the sum of the RT and FT.

The actual calculation of these measures depend on how the onset and the offset of a NB are detected. In our case they are found by intersection of a specific rate threshold used for identifying the NB (cfr Section 2.2.2), a methodology first used in [15].

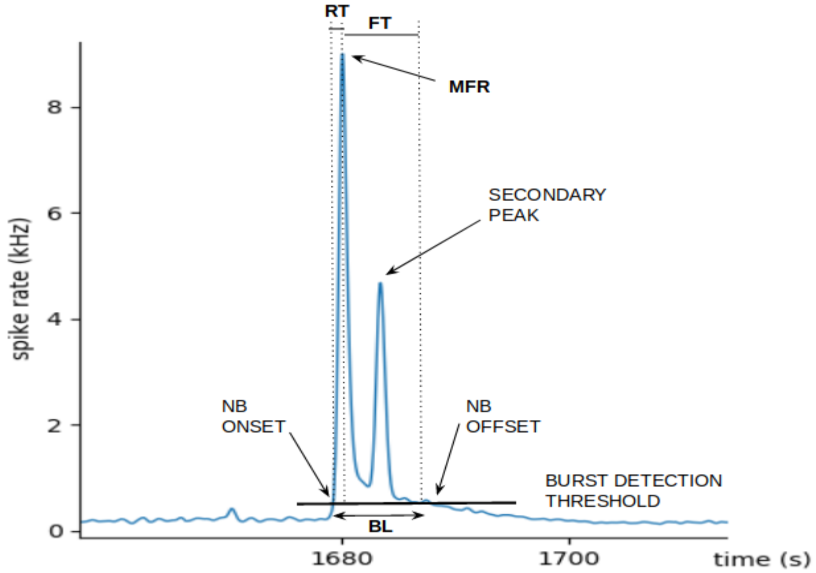

FIGURE 2.16: Sketch of a Network Burst Rate Profile (NBRP). The x axis represents the time and the y axis the instantaneous firing rate. From this construction it is possible to calculate different NB features concerning its shape. Given the burst detection threshold it is possible to individuate the onset and the offset by its intersection with the NBRP curve. The highest peak correspond to the Maximal Firing Rate (MFR). The rising time (RT) is calculated from the onset to the MFR and the falling time (FT) from the MFR until the offset. The sum of RT and FT gives the Burst Length (BL). The example is taken from the dense culture 6-1-13, recorded before the end of the second WIV, a period when superburstiness often occurred. In fact, the NB shows also a secondary smaller peaks.

As far it is concerned the NB shape, once the onset and the offset of a NB are individuated, one can calculate the **Burst Size** (BS) , i.e., the total number of spikes within the NB, a value that is correlated with the area under the curve in figure 2.16. Moreover, the **electrode Recruitment Count** (RC) , i.e., the active electrodes during the NB, can be found. The latter can be used also for normalizing the former in order to have a more suitable measure when comparing different NBs. The number of spikes within a NB can be also normalized with the total number of spikes recorded, obtaining the so called **Burstiness Index** (BI) . We report also the BI version calculated in [55] as in Section 3.1.1 we will try to reproduce their results. The authors in [55] counted the array-wide number of spikes in non-overlapping 1 s windows, and determined what fraction of the total number of spikes was contained in the 15% most active windows. Since NBs always occupied fewer than 10% of 1 s windows, this number, f_{15} , is close to one if most spikes occur in NBs. Conversely, if spikes are evenly spaced in time, f_{15} is close to 0.15. Then, they defined burstiness index as BI = $(f_{15}–0.15)/0.85$, making BI normalized between 0 (no NBs) and 1 (all spikes in NBs).

In order to capture the spatiotemporal organization of the neurons during the NB is interesting to measure the network **recruitment speed** of the active electrodes at the beginning of the NB, that is, how fast the neurons in the network start spiking in a synchronized manner at the NB onset. The recruitment speed was calculated as the maximum number of active electrodes divided by the time needed to achieve the maximum activation of the electrodes, approximated by the rising time.

Furthermore, also the **superburstiness** was taken into account, that is, the number of superbursts normalized with the total number of network bursts detected in one recording. First, in order to calculate this quantity, the **number of peaks within a NB** was found. In fact, as it is also possible to see from figure 2.16, NBs sometimes show smaller secondary peaks. We set a threshold at three peaks, above which a NB was labelled as a superburst. Although superbursts were already studied [54], these two measures were never used before.

Taking the average of NBRP it was possible to calculate the **Overall Firing Rate** (OFR) of one recording. In addition, also the network **Burst Rate** (BR) was calculated dividing the number of detected NBs by the recording time, converted into minutes. The NBRP can be thought as one dimensional signal of the overall activity of the neural network and before applying the more sophisticate approach based on Poincaré plots (see Section 2.3.2) we calculated the **first minimum of the autocorrelation function** and the **first harmonic of the spectrum** that account for the periodicity and the intrinsic frequency of the NBRP, respectively.

Measures that are related to the frequency can be extracted from the interval distributions. For example, the **Inter-spike Intervals** (ISI) distribution is calculated from the time intervals between consecutive spikes. This measure is related to the overall firing rate because when neurons spike more frequently the ISI distribution tends to be peaked in the lower values as the times between spikes are less spaced. The same distribution can be determined for the NB, i.e. the **Inter-Burst Interval** (IBI) , defined as the intervals between two consecutive NBs, more specifically, the time distance between the offset of a NB and the onset of the consecutive one. This measure is related to the Burst Rate. An alternative distribution is the **Inter-Peak Intervals** (IPI) , that is, the frequency distance between two consecutive NB peak. The IPI distribution can indicate how much variability a recording shows in the NB frequency. For example, a flat distribution means that all the NBs have the same MFR. A common way to calculate the variability and compare different distributions is the **Coefficient of Variation** (CV) , the variance normalized with the mean of a distribution.

Analogous definitions have been used for the SC spike- and burst-related measures, that is, the **OFR**, **ISI CV**, **BR**, **BL**, **BS**, **firing rate within burst**, **IBI CV** and **BI**. Here, the only difference can be found in how the bursts were detected because in this case the ISI-based method was used (cfr Section 2.2.2). The only measure which is calculated just for SC type is the **bursting electrodes**, that is, the number of electrodes that show bursting behaviour.

For the sake of completeness, some other measures related to NB are shortly mentioned, although they are not used in this work. In [52] the authors averaged the NBRP of each NB in a recording and fitted the curve obtained with a known function in order to find quantitative parameters that describe its shape. More complex characterization of the spatio-temporal pattern of NBs could be obtained by means of the correlations measures, like in [49] where the authors computed the correlation coefficient (CC) between pairwise-spike-time-difference matrices, or in [46] where the CCs were used to quantify changes between NBs. Finally, in [47] the authors quantified the spectral content of NBs by studying the low-frequency component of the local field potential.

2.3.2 Poincaré Plots

This section illustrates the measures extracted using the Poincaré plots, a tool derived from the chaotic time-series analyses. To better understand this approach, a brief introduction about chaotic dynamical system theory is given.
The chaotic regime has been proved to be an essential property in normal brain functions as it facilitates the quick adaptation to mutable conditions. Thus, chaos theory has turned an important tool for understanding the complex mechanisms of the nervous system and the non-linear dynamics behind the human behaviour [26, 11].
When dealing with non-linear time series, in order to use dynamical system techniques one should embed the time evolution in some phase space [21], a mathematical construction in which the coordinates represent the variables that specify the state of the system. The trajectory in the phase space provides the evolution of the system from which we can study interesting geometrical and dynamical property.
For the sake of simplicity, let us consider just deterministic discrete **dynamical systems** as we are dealing with experimental data. If x is a vector that specifies a state in the phase space, the evolution can be described by a map

$$x_{n+1} = F(x_n),\ n \in \mathbb{Z} \tag{2.1}$$

A sequence of points x_n, solving the above equation is the trajectory of the dynamical system, with initial condition x_0. The simplest examples of attractors are the fixed points and the limit cycles, that determine a stationary state and periodic motion, respectively. If the dynamic is characterized by chaotic behavior the attractor can exhibit complicated fractal structure and it is called strange attractor.

Given the condition stated in the embedding **Takens' theorem** [48], a chaotic dynamic system can be reconstructed from a time series (such as a spiking recording) by the method of delays. In formulas, the scalar measurements can be written as

$$s_n = s(x(n\Delta t)) + \eta_n \tag{2.2}$$

a time series of some quantity x taken at multiples of a fixed sampling time Δt. We look at the system through some measurement functions s and make observation up to some random noise η_n, that we will discard at this level of study. A delay reconstruction in m dimensions is then formed by the vectors s_n , given as $s_n = (s_{n-(m-1)\tau}, s_{n-(m-2)\tau}, ..., s_{n-\tau}, s_n)$, with n > (m - 1)$\tau$. The time difference in number of samples τ (or in time units, $\tau\Delta t$) between adjacent components of the delay vectors is called lag or **delay time**. Under general circumstance the geometrical object embedded in a **m dimensional phase space** formed by the vectors s_n is equivalent to the original sequence x_n if the dimension m of the delay coordinate space is larger than twice of the dimension D of the attractor, i.e. roughly speaking, larger than twice the number of active degrees of freedom. Depending on the application, even smaller m values satisfying D < m < 2D can be sufficient.
However, at the beginning we neither know the attractor dimension nor the time lag. For determining the optimal embedding parameters m and τ one can start the analysis with a guess and then tune them according to the results. Apart to meet the

condition of the Takens theorem, a minimum value of m is desirable for reducing the computational effort and unwanted redundancies. Thus, we started using the minimum value permitted, m=2, and later we checked the goodness of the analysis. As far as it is concerned the time lag, embeddings with the same m but different τ are equivalent in mathematical sense, but in reality a good choice of τ facilitates the analysis. If τ is small compared to the internal time scales of the system, successive elements of the delay vectors are strongly correlated, making vectors s_n clustering around the principal diagonal of the phase space. If τ is very large, successive elements are almost independent, and the points are spread in an uninformative large cloud. However, most of the time, a reasonable choice of τ can be visually verified [21]. Below we will illustrate our choice of m and τ in the two cases taken under study, when building Poincaré plots from IBI/IPI distributions (figure 2.17 lower panels) and from NBRP (figure 2.17 upper panels), a discrete and a continuous signal, respectively.

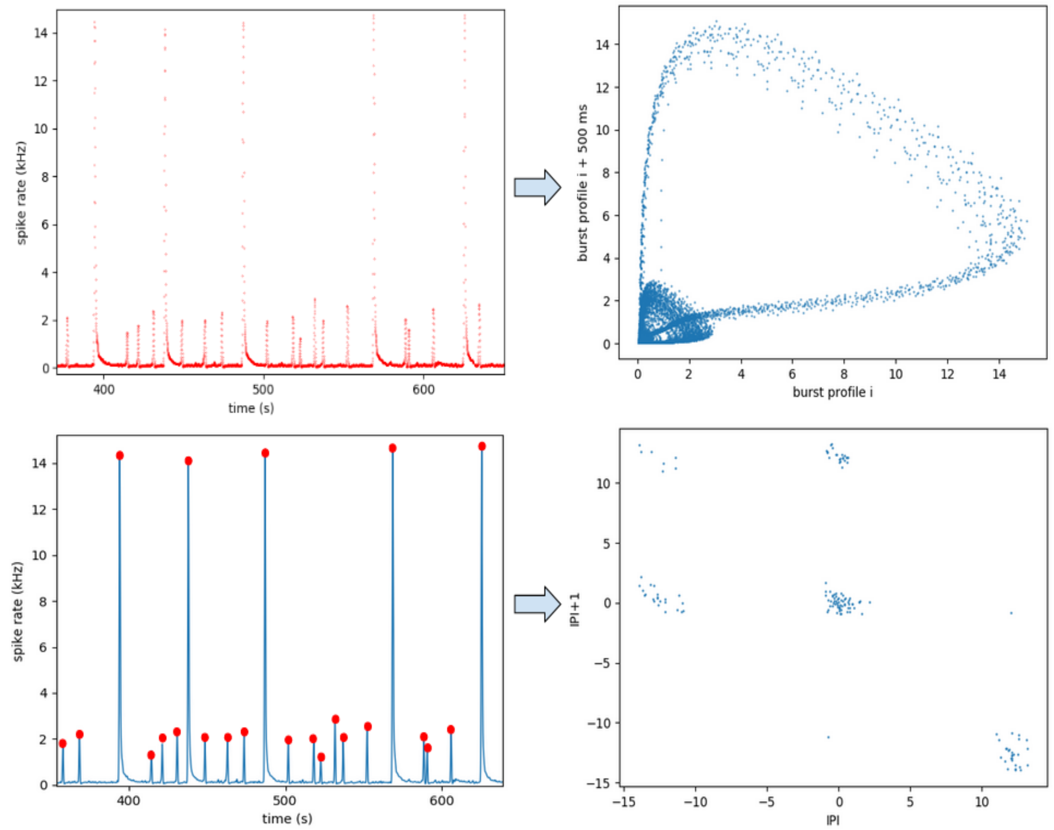

FIGURE 2.17: The upper panels show the case of embedding in a two dimensional phase space the entire NBRP signal (left-hand panel); in fact, all the points (marked in red) are considered for building the Poincaré plot (right-hand panel). The trajectory in a two dimensional phase space is obtained by plotting NBRP against NBRP+τ, with τ=500 ms. The lower plots report the case of a Poincaré plot construction considering the IPI distribution (left-hand panel). Here just the intervals between the points indicating a NB are considered (marked with red dots). Two state variables (m=2) shifted by one interval step (τ=1) are used to draw the trajectory in the phase space (right-hand panel). The IBI Poincaré plot are analogously built. The recording come from the dense culture 6-1-22.

Let us start from the **Poincaré plots** obtained from **IBI** and **IPI** distributions. These measurement sequences were embedded in a two dimensional phase space (m=2) using the second state variable shifted by one interval step (τ=1), that is, plotting the time series X_i, X_{i+1} (see figure 2.17 lower panels), where X can be IBI or IPI. We used a two dimension phase space because it was already possible to see interesting attractor patterns. Thus, in order to reduce the time consumption of the algorithm we did not increase the dimension further. The choice of the time delay is usually the one used for discrete signals, as we wanted to see the relation between consecutive NBs. From the correlation matrix of the two delayed time series, the **eigenvalues ratio** was calculated to evaluate the dispersion of the points. More dispersed points correspond to a more variable signal, meaning that the NBs are irregularly spaced (IBI case) or that they reach different MFR in a single recording (IPI case). As it is shown in figure 2.17 (lower right-hand panel), another way to measure this variability is to quantify the clustering properties, as some points are concentrated on a particular area of the phase space. Then, we calculated the **number of clusters** in the scatter plot by means of the agglomerative clustering algorithm. We did not set the number of clusters but just the maximal distance threshold as the maximum diameter span by the points (cfr Section 2.2.3).

Next, other measures related to the **NBRP** were extracted using the **Poincaré plot** method. We embedded the NBRP continuous signal in a two dimensions phase space (m=2) and we set the time delay between the two state variables at 500 ms, that is, we plotted the trajectory in the space (NBRP,NBRP+τ), with τ=500 ms (see figure 2.17, upper plots). We used a two dimensional embedding space for reducing the computational time, as the attractors already looked well-shaped. Afterward, we calculated the dimension of the trajectory to see if the condition of the Takens theorem holds. In order to calculate the right time delay, the methods explained in [26] were followed. One of the most common method is based on the first minimum of the mutual information function. However, this function is monotonically decreasing with these data, that is, it does not show a sharp minimum, at least for short time delays. Then, an alternative method based on the first zero-crossing of autocorrelation function was tried. Also in this case the method was not applicable, as the autocorrelation function was strictly positive. Next, we calculated the **first minimum of the autocorrelation**, and except for the really young cultures, this value is not suitable because too high. However, we kept this measure for the next analysis. Then, after some visual inspections we decided to take the fix value of 500 ms (same value used in [54]) because the plots shown well defined attractors. Using this time delay, the **mutual information** between NBRP and NBPR+τ was calculated and used as a measure for the subsequent steps.
As it can be seen from figure 2.17 (upper right-hand panel) we obtained well-looking trajectory, that resembled the shape of strange attractors. To characterize the attractor, some basic concepts of chaotic dynamical system theory have been used, such as correlation dimensions and Lyapunov exponents. These parameters are invariant under the evolution operator of the system and thus are independent of changes in the initial conditions of the orbit. In addition, both are independent of the coordinate system in which the attractor is observed, making them suitable to be used with experimental data. Another advantage of these quantities is that each one of them will turn a sequence of data into a single number, which is convenient for comparing different time series [26].

To quantify the fractal dimension characterizing a strange attractor we used the correlation dimension because it can be easily extracted from the data. For calculating the **Correlation Dimension** (CD), we divided the attractor into boxes of radius ϵ and then calculated how many boxes, $N(\epsilon)$, we needed to cover all the points in the dataset. Considering the relative frequency P_i with which the trajectory enters the i-th box of the covering, the CD is defined by

$$CD = \lim_{\epsilon \to 0} \frac{ln \sum_{i=1}^{N(\epsilon)} P_i^2}{ln \epsilon} \tag{2.3}$$

In order to calculate the CD the Grassberger-Procaccia algorithm [14] was used. We used a publicly available Python implementation of the algorithm (see github repository of JC Vasquez-Correa, `https://github.com/jcvasquezc/Corr_Dim/blob/master/Corr_Dim.py`). Let the N points be denoted by $x_1, \dots x_N$, in some metric space with distances $\|x_i x_j\|$ between any pair of points. For any positive number r, the correlation sum C(r) is then defined as the fraction of pairs whose distance is smaller than r

$$C(r) = \frac{2}{N(N-1)} \sum_{i<j} \Theta(r - |x_i - x_j|) \tag{2.4}$$

where $\Theta(x)$ is the Heaviside step function. C(r) is monotonically decreasing to zero as $r \to 0$. If C(r) decreases like a power law, $C(r) \sim r^{CD}$, then CD is the correlation dimension. Formally, the dimension is defined by

$$CD = \lim_{r \to 0} \frac{logC(r)}{log(r)} \tag{2.5}$$

so the simplest and most naive way to estimate CD is to plot C(r) against r on a log-log plot and to fit a straight line to the small-r tail of the curve. CD is then the slope of this line. Calculating the fractal dimension of the attractor is also useful for testing the goodness of the chosen embedding dimension. It came out that the attractors obtained with our data have CD usually lower than 2 (see Section 3.1.2), so the choice of the embedding dimension used to build the Poincaré plots is justified because the condition CD<m<2CD is satisfied.

Lyapunov Exponent (LE) is one of the most important quantity for characterizing chaotic systems because a positive maximal LE is a strong signature of chaos. Conversely, a zero maximal LE denotes a periodic orbit and a negative maximal LE represents a fixed point. Therefore, LE is a measure of exponential divergence of nearby trajectories or, otherwise stated, of the difference between a given trajectory and the path it would have followed in the absence of perturbation. Assuming two points x_1 and x_2 initially separated from each other by a small distance δ_0, and at time t by distance δ_t, then the LE is determined by the relation

$$\delta_{x(t)} = \delta_{x(0)} e^{\lambda t} \tag{2.6}$$

where λ represents the LE. An m-dimensional system has m LE with $\lambda_1, ..., \lambda_m$ in descending order. Then, LE is a measure of sensitive dependence on initial conditions, i.e. how quickly two nearby states diverge. Now consider two points in the time-series, t_i and t_j, whose values are very close. That means the system reached near the same state at the i^{th} and j^{th} iterations. Now consider the two sequences t_i, t_{i+1}, t_{i+2} $\dots$ and t_j, t_{j+1}, t_{j+2} $\dots$ We wish to know how these two sequences diverge from each other. For this, consider the distance between the two sequences after k steps:

$d(k) = \|t_{i+k}, t_{j+k}\|$ (where $\|.\|$ is the Euclidean distance). If the system is chaotic, d(k) will initially rise exponentially with k. For this, one can plot ln(d(k)) against k and apply a linear fit. The slope will be an estimate for the LE. However, since the system is bounded, the two nearby states will not diverge indefinitely though. Their exponential divergence will stop after some length. We must fit the straight line only within this region, so we set the fit just for the first 4 steps (k). Now, this was for a single pair of initial states. The LE is an average of this divergence exponent over all nearby initial pairs. So we defined <d(k)>, the average over all starting pairs t_i, t_j, such that the initial distance d(0) = $\|t_i, t_j\|$ is less than some fixed small value. The algorithm implemented finds all such initial pairs, calculates <d(k)> against k, and the slope of the initial linear part gives us the LE. In order to speed up the calculation, we did not use all the pairs of points but just some of them (the first 1000). This method is described in [4].

In literature the method of studying time series as attractors in an embedding space is also called return plots methods. For example in [52] the authors used this technique for studying the effect of low-frequency electrical stimulation in long-lasting alterations in spontaneous activity of cortical neuronal networks. In [54] Wagenaar et al. used this method for studying the complex spatio-temporal pattern of superbursts. Moreover, another widespread application of Poincaré Plots can be found in Hearth Rate studies. For example in [17] the authors analysed the box counting dimension of heart rate signal in both two- and three-dimensional Poincaré plots in a group of post myocardial infarction patients. Another interesting implementation of the chaotic time-series methods can be found in [18] where the authors extracted different features from Poincaré plots for classifying patients with arrhythmia and healthy controls.

2.3.3 Spike Train Synchrony

When analysing experimental data obtained by recording the neural systems with a multi-channel devise it is fundamental to quantify the correlation among the spike trains. The activity synchronization can give us many important information about neural coding process, the network state of development, or the presence of some functional relations that reflect structural changes (cfr Section 1.3.2).

However, this task is not always so straightforward and some forethought should be kept in mind when performing this kind of analysis. The action potential is not an instantaneous point event but it has a certain extended time structure because the spike is just a construction that we made up for facilitate the analysis. Then, considering also the time delay of signal transmission between neurons (see Section 2.2.1), the synchrony should be calculated with reference to a range of time. Moreover, the spiking activity (approximately from 1 Hz to 15 kHz, from quiescent periods to high-frequency NBs, respectively) is much sparser than the sampling frequency (typically set at 20 kHz). Thus, conventional approaches are usually not well suitable for measuring the spike correlation [9]. In [9] Cutts at al. summarized all the necessary properties of a well-designed correlation measure for spiking data. This measure should be robust to spike rate variability, to the recording duration and to the timescale used to determine the synchronicity.

After an extensive literature research the authors in [9] classified the correlation measures into six categories. Covering all the six categories is out of the scope of the thesis as we wanted to test a wide-range of measures and not just correlations.

However, we managed to extract seven different measures, based on pair-wise comparison of both continuous and discrete time series [24, 23] and on the overall network dynamic synchrony [13]. Below the measures implemented in this work are illustrated.

The simplest and most widely used measure of synchronization is the **Pearson correlation**. Given two random variables X and Y, which correspond to two spiking trains in our case, the coefficient is defined by

$$\rho_{XY} = \frac{cov(X,Y)}{\sigma_X \sigma_Y} \tag{2.7}$$

where cov(X,Y) is the covariance, and σ_X and σ_Y the standard deviation of X and Y, respectively. Its value is symmetric in X and Y and attains a maximum value of 1 for complete synchronization, a minimum value of -1 for completely anticorrelated signals, and values close to 0 for linearly independent signals. In our implementation the Pearson correlation was calculated from the binned spiking matrix (see Section 2.2.1) using the in-build Numpy function, through two different approaches. We took into account the spikes in the entire recording and in sliding windows, with a window width of 10 bins and an overlap of one bin. The latter permits to check how the correlations changed over the time, between the bursting and not bursting period, obtaining a more faithful value of the correlation.

In contrast to the cross correlation, **mutual information** quantifies not only linear but also nonlinear dependencies between spike trains X and Y. It is a measure originating from information theory and is based on the Shannon entropy, a measure which quantifies the uncertainty of a probability distribution. It is defined as

$$I(X,Y) = H(X) + H(Y) - H(X,Y) \tag{2.8}$$

which uses the Shannon entropies of the marginal distributions, e.g.

$$H(X) = -\sum_{i=1}^{M_x} p_x(i) log p_x(i) \tag{2.9}$$

as well as the Shannon entropy of the joint distribution

$$H(X,Y) = -\sum_{i=1}^{M_x} \sum_{j=1}^{M_y} p_{xy}(i,j) log p_{xy}(i,j) \tag{2.10}$$

Here $p_x(i)$ i=1,...,M_x ($p_y(j), j = 1, ..., M_y$) represent the normalized probabilities of the i-th (j-th) state in X-space (Y-space). Their joint probability is denoted by $p_{xy}(i,j)$, while M_x and M_y denote the respective numbers of states. Mutual information is symmetric in X and Y and quantifies the amount of information about X obtained by knowing Y and vice versa. If the logarithms are defined with base 2, it is measured in bits. Mutual information is zero if and only if the two time series are independent. We calculated this measure from the binned spiking matrix using the in-build function in Sklearn library.

Another spike train distance used in our analysis was introduced by **van Rossum** in [43]. Here the discrete spike trains X and Y are transformed into continuous functions by convolving each spike t_k with an exponential kernel. This kernel shape is motivated by its causality and its resemblance to the shape of postsynaptic currents. From the resulting waveforms $\tilde{x}(t)$ and $\tilde{y}(t)$, the van Rossum distance DR can be calculated as

$$DR(\tau_R) = \sqrt{\frac{1}{\tau_R}\int_0^\infty [\tilde{x}(t) - \tilde{y}(t)]^2 dt} \tag{2.11}$$

For this method, the time constant τ_R of the exponential acts as the parameter that sets the timescale, i.e., the temporal relationship between the spikes is evaluated for low τ_R, while for high τ_R the distance is only sensitive to differences in rate. The DR were calculated adapting the code from Elephant (Electrophysiology Analysis Toolkit, `https://elephant.readthedocs.io/en/latest/overview.html`), an open-source library for the analysis of electrophysiological data in Python programming language.

In [9] the authors tested a wide range of correlation measures to see if they fulfilled all the desirable properties they have reported. As none of the measures found in literature passes the test, they ended up defining a novel measure covering all the mentioned hallmarks, called **spike time tiling coefficient** (STTC) . To quantify the correlation between spike trains X and Y, they looked for spikes in X which fall within ±Δt of a spike from Y. They considered the proportion of spikes in X (P_X) which have this property. They account for the amount of correlation expected by chance by making the minimal assumption that one expects the proportion of spikes from X falling within ±Δt of a spike from Y by chance to be the same as the proportion of the total recording time which falls within ±Δt of a spike from Y (T_Y). Any extra spikes in X which have this property are indicative of positive correlation. They therefore used the quantity P_X - T_Y which is positive if spikes in train X are correlated with spikes from train Y, and negative if there is less correlation than expected by chance. Moreover, the normalization factor (1 - $P_X T_Y$) ensures that the coefficient lies in the range [-1, 1]. The coefficient should be symmetric so they considered both (P_X - T_Y) and (P_Y - T_X), combine the contributions from both trains and renormalize to preserve the required range. In formulas:

$$STTC = \frac{1}{2}\Big(\frac{P_X - T_Y}{1 - P_X T_Y} + \frac{P_Y - T_X}{1 - P_Y T_X}\Big) \tag{2.12}$$

The spike time tiling coefficient uses the proportion of the recording which falls within ±Δt of spikes from X to determine whether the proportion of spikes in Y which also have this property is indicative of correlation (i.e., more than is expected by chance). Also this measure was calculated adapting the code from Elephant open-source python library.

Synchrony is a property of the activity of large neuronal networks that can be defined in several way. Here we used the definition given in [13]. One of the simplest cases is a network of N neurons where the coupling between cells does not depend on the distance between them. Such networks can settle into two generic states called asynchronous and synchronous, depending on the temporal fluctuations of a global neural variable, such as the population-average voltage or spiking activity. In the asynchronous state, the variance of such quantity vanishes as N increases. On the other hand, in synchronous states, the temporal fluctuations are on a global scale and do not vanish as N increases. Since synchrony is related to the fluctuations of global variables, it can be defined by averaging these fluctuations over a long time.

To normalize the synchrony measure, this average is divided by the average fluctuations in the variables of single neurons. Here we report the terminology used in [13], where they derived the equation using the membrane potential V although the formulation can be straightforward adapted to the instantaneous activity of neurons. One evaluates at a given time, t , the average quantity $V(t) = (1/N)\sum_{i=1}^{N} V_i(t)$. The variance of the time fluctuations of V(t) is $\sigma_V^2 = \left\langle [V(t)]^2 \right\rangle_t - [\langle V(t)\rangle_t]^2$. After normalization of σ_V to the average over the population of the single cell variable one defines a synchrony measure $\chi(N)$, for the activity of a system of N neurons by:

$$\chi^2(N) = \frac{\sigma_V^2}{\frac{1}{N}\sum_{i=1}^{N}\sigma_{V_i}^2} \tag{2.13}$$

$\chi(N)$ spans between 0 and 1. It is possible to show that $\chi(N)$ is related to the cross correlation (CC) between the activity of pairs of neurons [13]. As we already said, we are not considering the continuous voltage recording but the discrete spiking data. Therefore, in order to calculate $\chi(N)$ of the cultured neural networks, we built a binned spiking matrix reporting the number of spike within 50 ms bin (normalized for obtaining the spike frequency) across the recording time for each electrode. Then, we applied straightforward the equation 2.14 substituting the voltage with the spiking frequency.

In statistics, the **Fano factor** (FF) , like the coefficient of variation, is a measure of the dispersion of a probability distribution and it can be viewed as a kind of noise-to-signal ratio. It is defined as

$$FF = \frac{\sigma_W^2}{\mu_W} \tag{2.14}$$

where σ_W^2 is the variance and μ_W is the mean of a random process in some time window W. As a metric of comparison one can consider the Poisson process, in which the variance is equal to the mean so FF=1. If the time window is chosen to be infinity, FF is similar to the variance-to-mean ratio which in statistics is also known as the index of dispersion. FF, along with the coefficient of variation, has been used in neuroscience to describe variability in recorded spike trains, quantifying the amount of variance in the spiking activity relative to the mean spike rate [10]. Using the same binned spiking matrix as the last measure, FF was calculated as the standard deviation over the mean of the average spiking activity in each electrode.

Chapter 3

Results

This chapter shows the main results of the analysis. All the measures extracted from the neural activity data were systematically explored, checking how they are influenced by different factors, namely, culture age, density and batch. This was conducted at various levels, from preliminary exploratory statistics to some basic distributions comparison. Finally, also more advanced analysis based on machine learning techniques were performed.

3.1 Exploratory Statistic

Before applying sophisticated analysis, it is important to characterize and understand the underlying properties of the data. In this section we are going to perform some basic preliminary statistic, studying the effect of different factors on the *in vitro* neural activity. This task was achieved plotting the measure distributions, dividing them in a systematic way among the different elements that could affect the data, as the age, density and batch. Then, in order to quantify the variability in the data some simple statistical tests were performed.

3.1.1 Reproducibility of the Original Results

First of all, we tried to reproduce some of the results shown in [55], the original paper that describes the dataset of neural network activity used in this work. Specifically, we wanted to obtain a similar trend of the firing rate, the burstiness and lengths (including the rising and falling times), over the different DIVs. These comparisons were also performed for testing the goodness of the previous steps of the pipeline, in particular, the burst detection. Here we focused only on the dense cultures but in the next sections we will also look at the other density condition.

Furthermore, we also checked the bursting variability among different cultures, comparing the recordings with the table reported in figure 2.3. We visually inspected if the burst types observed and detected with our own implementation reflected the ones reported in [55]. As it is already described in section 2.1.2, the authors in [55] classified the bursts observed in the data according to different features, as the burst size, burst rate, tail and 'superburstiness'. In order to visually compare the burst behaviour of the recording, we randomly picked some samples from the dense and sparse dataset, we calculated the NBRP (also called AWSD) and we checked if we could qualitatively classify the activity as in [55]. Hence, we could distinguish the types of burst reported in the figure 2.3 as, for instance, little burst, long-tailed burst, variability in burst rate and different kind of superbursts, both in early and elderly cultures.

Subsequently, it was reproduced some of the scatter plots reported in [55], specifically the figures 4 and 6. The former shows the averaged development of firing (baseline activity) and bursting activity in dense cultures, i.e the ASDR and the Burtiness Index (BI) along the days in vitro, respectively. The figure 3.1 from [55] was visually compared with our own plots reported in figure 3.2. We could not compare them quantitatively, i.e. studying their correlation, because we had just the raw spiking activity and not the processed data.

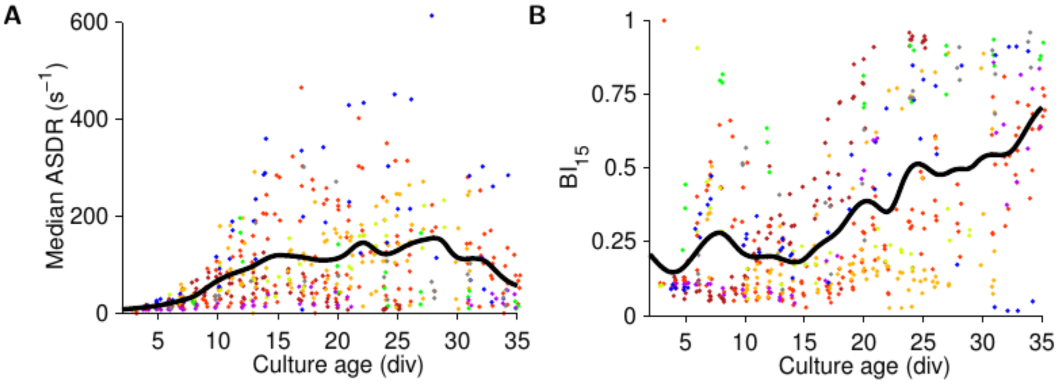

FIGURE 3.1: A) Median ASDR as a function of developmental age. Medians were taken across all 1800 one-second-wide time bins in individual half-hour long recordings. B) Burstiness index as a function of developmental age. Dots in A and B are measurements from individual cultures, colored by plating batch. Black lines are interpolated averages across all cultures, using a Gaussian window with a half-width of 1 day. Dots were horizontally jittered by ± 0.25 days for visual clarity. Image taken from [55].

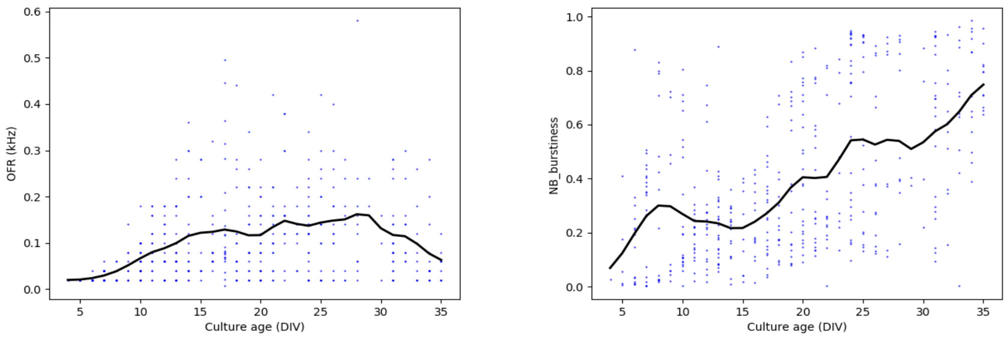

FIGURE 3.2: On the left the OFR (calculated as the ASDR in [55]) and on the right the burstiness index along the DIVs. These scatter plots were reported for reproducing the results shown in fig.3.1. The blue dots represent the values for each culture and the black line is the average over one DIV.

All the plots report the median culture value over the recording (dots) and the overall average value across the different cultures with the same age (black line), smoothed with a Gaussian kernel (SD = 1 DIV). It should be stressed out that the measures are calculated until the 35th DIV, discarding the samples of latter age. The dataset comprises of really few samples at 36-39 DIV, as it can be seen in table 2.1. As far as it is concerned the **firing rate** (plots on the left in figures 3.1 and 3.2), the two graphs are really similar, both in shape and scale. In fact, both the plots show a baseline activity increasing up to 200 Hz until approximately the 28th DIV (with a steady increasing until the 15^{th} DIV where the firing rate reaches almost 150 Hz) and then a slightly decreasing until the 35^{th} DIV.

Also in the case of **burstiness index** it is possible to see a similar rising trend. However, the two curves are not perfectly the same because the definition of burstiness used in this work is quite different from the one in [55] (cfr Section 2.3.1). However, the differences are really tiny. In general, the two curves show a rapid increasing up to $\sim$ 0.3 until the 8^{th} DIV and then they slightly decrease until the 15^{th} DIV. Afterwards, the trend starts to grow again, with some oscillation between the 20^{th} and the 28^{th} DIV, until it reaches $\sim$ 0.75 at the end of the DIVs considered.

The next comparison is about the network **burst lengths**, namely the burst total duration (BL), the rising time (RT) and the falling time (FT). As it can be seen from figure 3.3, in [55] the authors plot the trend across the DIVs of the lengths, onsets and offsets duration of all the bursts detected in all the dense cultures recordings. The black line is the average across all the culture with the same age. They obtained these plots measuring the ASDR as a function of time during the burst, smoothed with a 10 ms Gaussian filter. The 20% and 80% points between baseline and ASDR peak were determined and used to define the burst phases. Thus, besides the different detection method, they also used another definition for RT and FT.

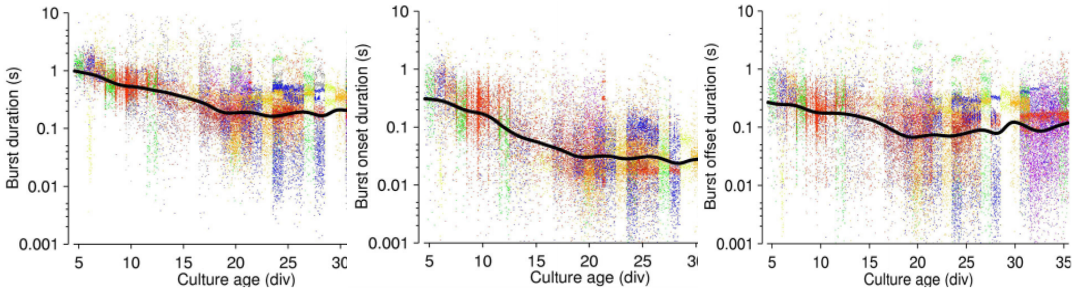

FIGURE 3.3: From the left: the total length of individual bursts, duration of onset and offset phases (Note the y log scale). In all panels, dots represent individual bursts, horizontally jittered for clarity, and colored by plating batch. Lines are interpolated averages, computed in log-space, using a Gaussian window with a half-width of 1 DIV. Adapted from [55].

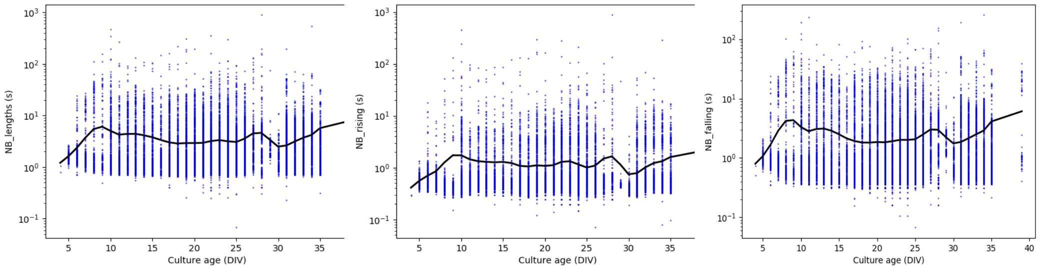

FIGURE 3.4: Scatter plots of burst lengths, rising times and falling times across the DIVs with log y-axis. The blue dots represent the value for each culture sample. For each DIV the average is calculated (black line).

All the plots in figure 3.3 decrease until the 20^{th} DIV and then it follows an almost steady behaviour, with a little rising in BL and FT. The lengths and the offsets lie between 1 s and $\sim$ 0.1 s while the onsets span to $\sim$ 0.01 s. In fact, as it was also demonstrated in other studies [6], usually the burst shows a fast rising time and a slower falling time, explaining the similarity between the BLs and the FTs. Our reproduction of these plots, shown in figure 3.4, used a different definition of onsets and offsets. As it was already explained in Section 2.3.1, the onset and the offset were detected from the base of the burst to the peak. In general, the average lengths are almost one order of magnitude bigger than the ones in [55], as on average the RTs lies between 0.3 s and 2 s and the FTs between 0.8 s and 6 s. Thus, also in this case the RTs are shorter than the FTs. Moreover, contrarily of what is shown in figure 3.3, all the curves show an increment at the early ages, from 3^{th} DIV to $\sim 8^{th}$ DIV, and then a slightly decreasing behaviour until the maturity ($\sim 20^{th}$ DIV). This phenomenon is in line with what is reported in literature (e.g. in [6]), that is, a broadening of bursts duration after few days the dissociated neurons were plated and a shrinking when the cultures approach the maturity. After the 20^{th} DIV the duration seems to undergo to a small increasing with some oscillation between the 25^{th} and the 30^{th} DIV, likely due to the different developmental batch behaviours.

These differences are certainly also due to the burst detection method implemented. In the paper they first looked at single channel burst ('burstlets') and they counted as a network burst if a minimum number of burstlets overlap. In our implementation we analyzed the overall firing rate, looking for peaks above a certain threshold (cfr Section 2.2.2). In this way we discarded really little NBs made by few single bursts than not really affect the overall firing rate, a consequence particularly present in mature cultures whit high baseline activity.

3.1.2 Measurement Trends

In this paragraph is shown a systematic study of the main properties regarding all the measures extracted from the recordings. This will be useful for giving us a general overview of the behaviour in different experimental conditions. It has been reported (see [6]) that *in vitro* neural networks show rich variety of dynamics that depend on density, culture age and the specific biological properties of neurons in the culture (changing from batch to batch). In order to understand this variability is important to graphically illustrate the activity considering each of these factors. Therefore, for each measure two plots are reported, one for each density condition. In figure 3.5 the column on the left reports the dense cultures and the column on the right the sparse cultures and each row shows the trend for a different measure. In these plots the median (black bold curve), the 25^{th} and the 75^{th} percentiles (black dotted curves) of the measures are plotted against the culture age. Moreover, for each batch, the overall average is drawn, showing the variability between different preparations (coloured lines).

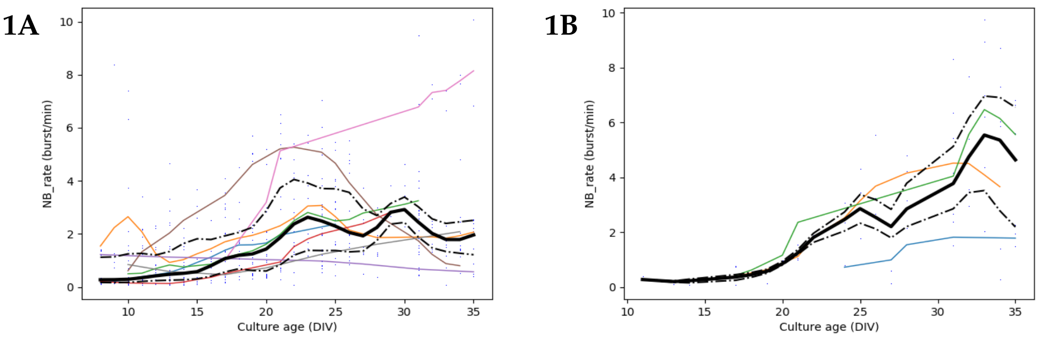

2A

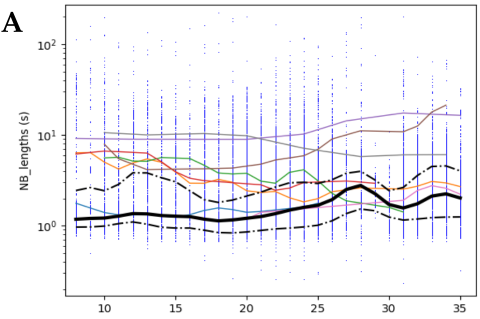

2B

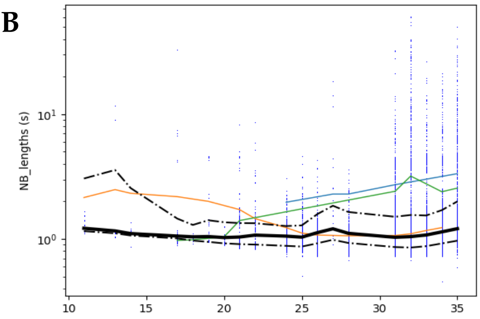

3A

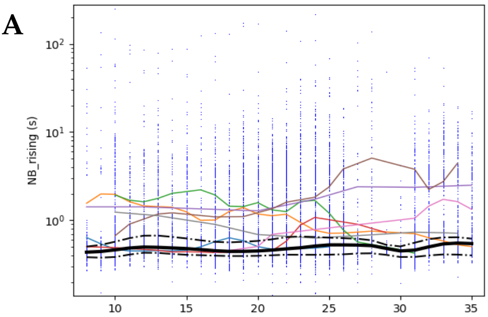

3B

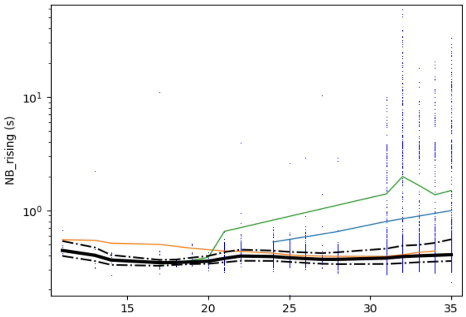

4A

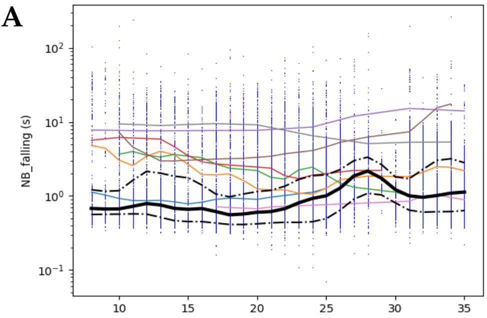

4B

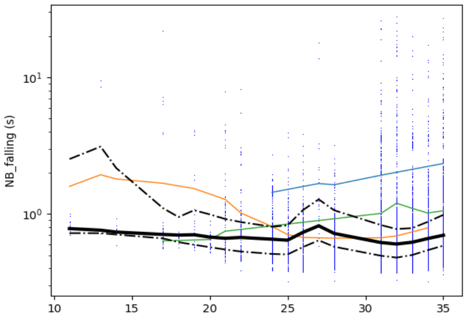

5A

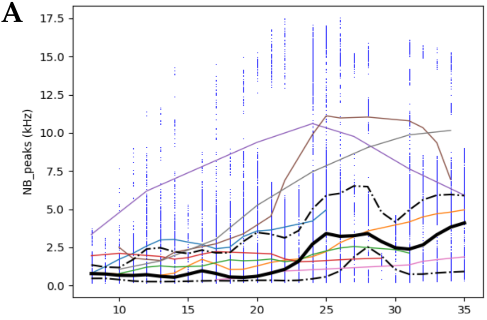

5B

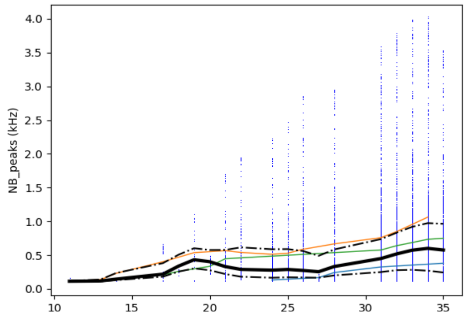

6A

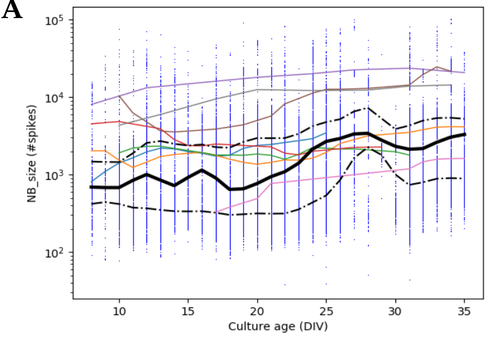

6B

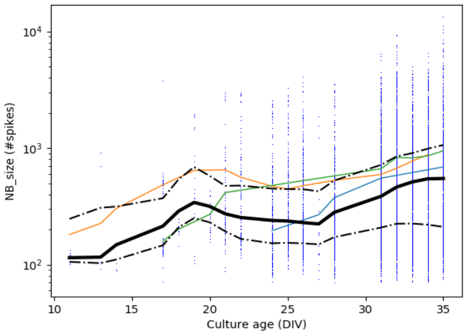

7A

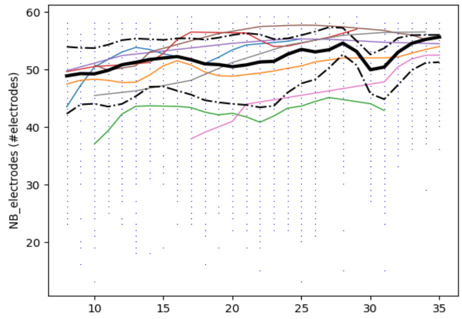

7B

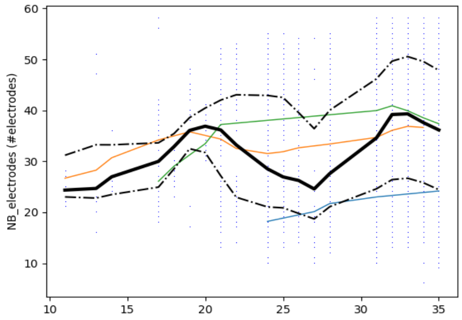

8A

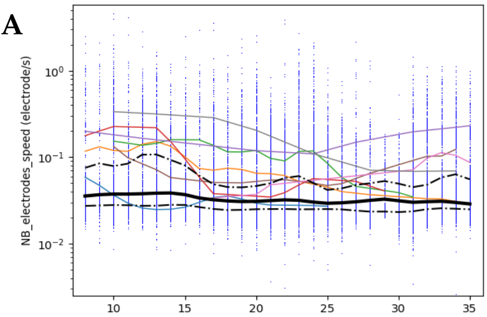

8B

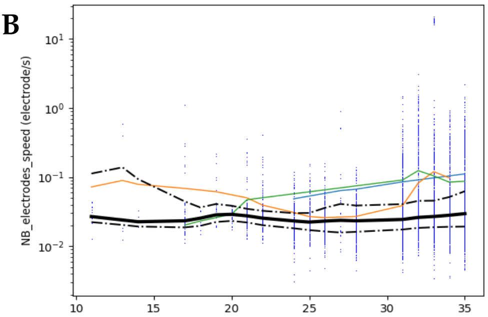

9A

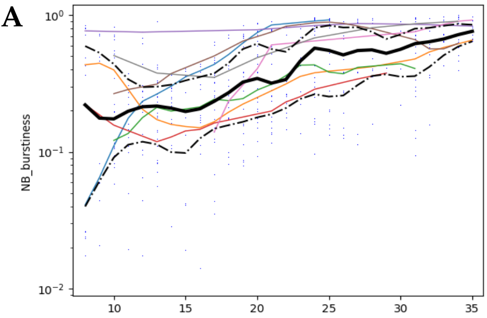

9B

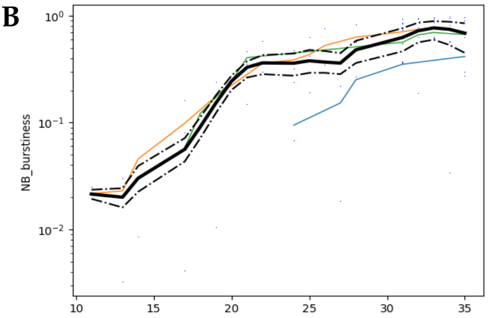

10A

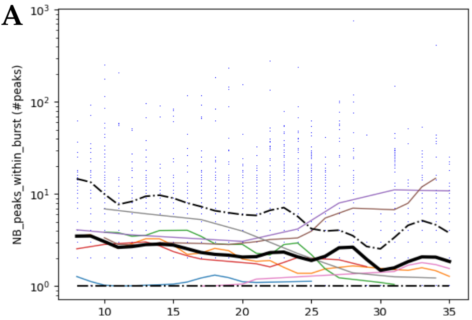

10B

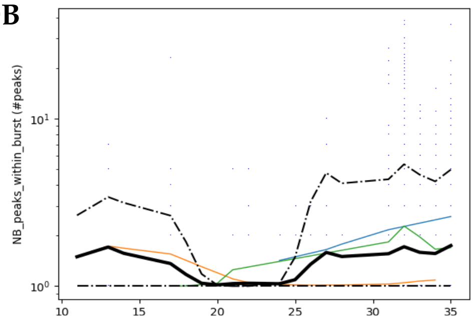

11A

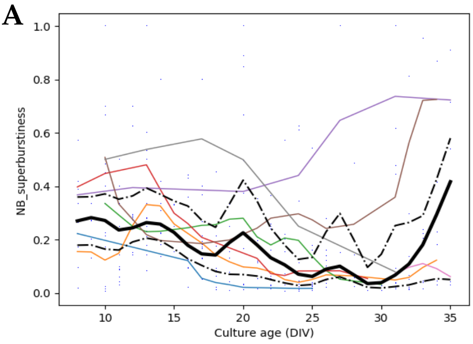

11B

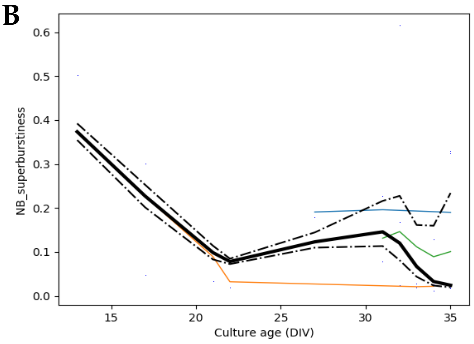

12A

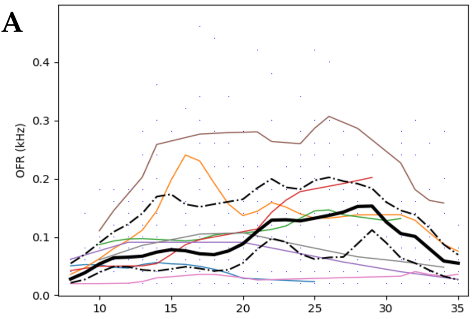

12B

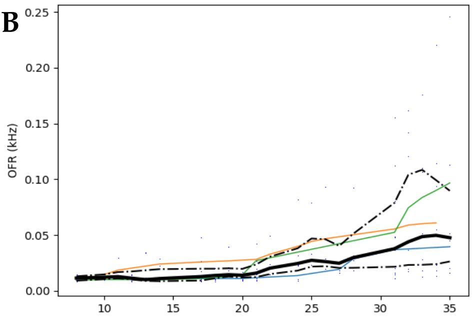

13A

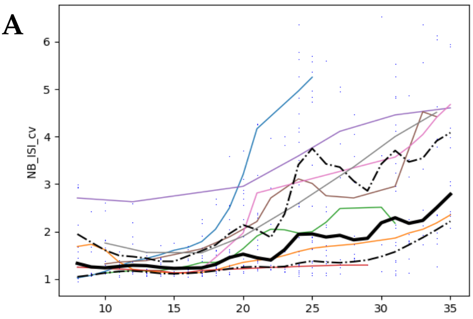

13B

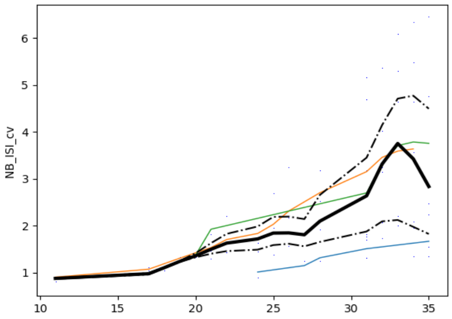

14A

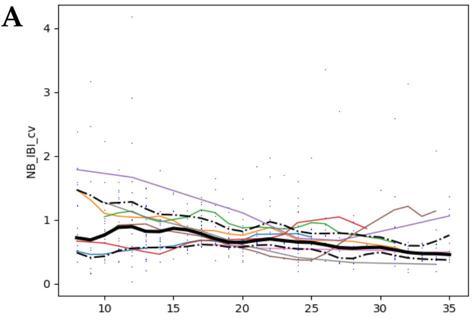

14B

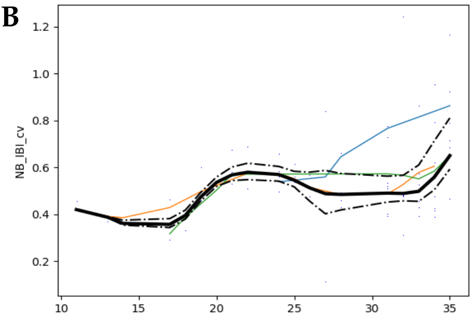

15A

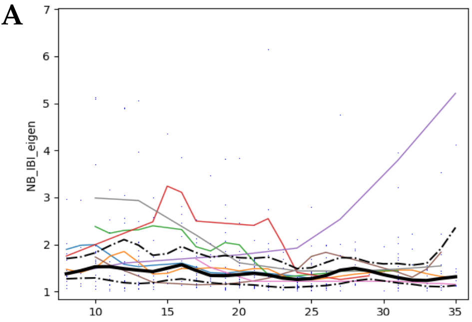

15B

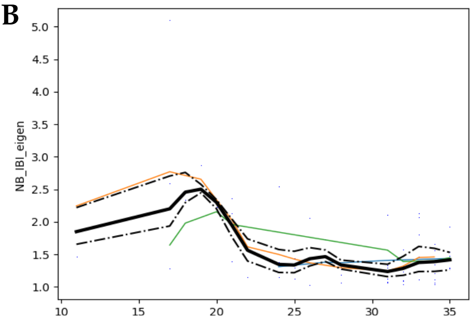

16A

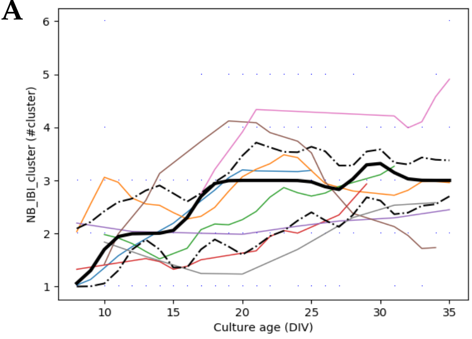

16B

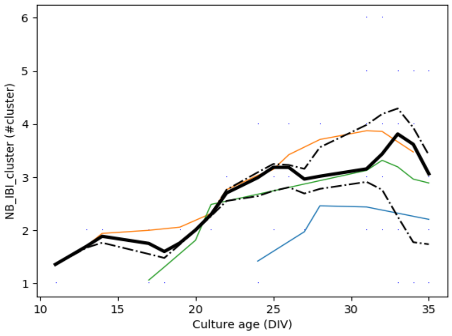

17A

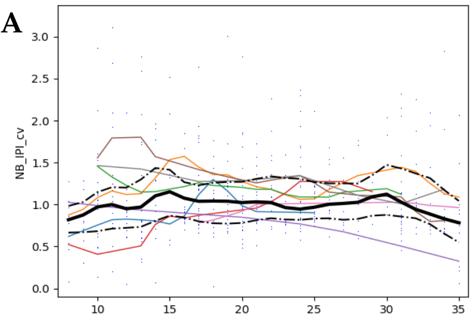

17B

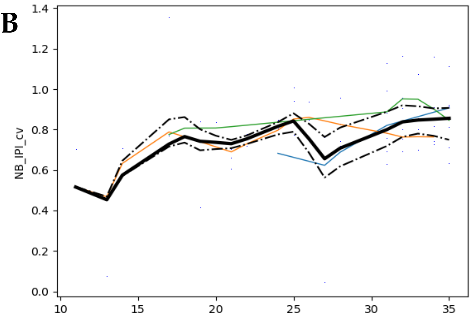

18A

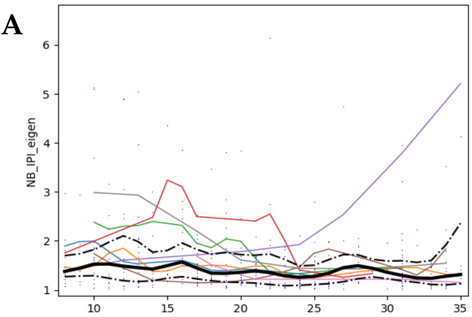

18B

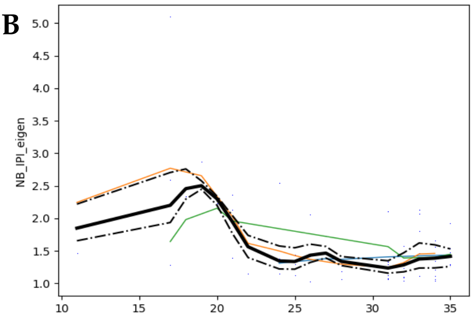

19A

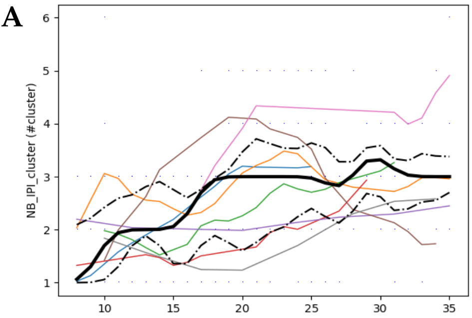

19B

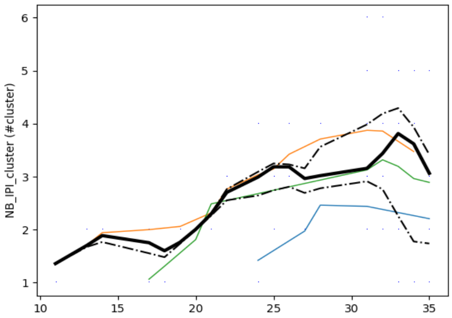

20A

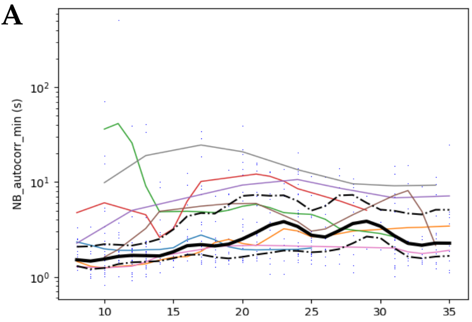

20B

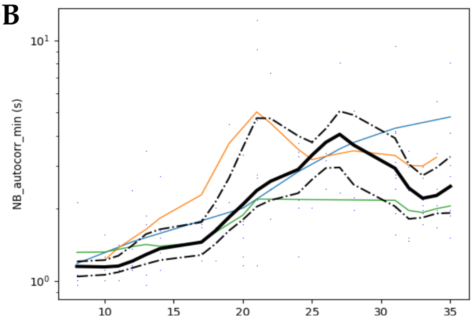

21A

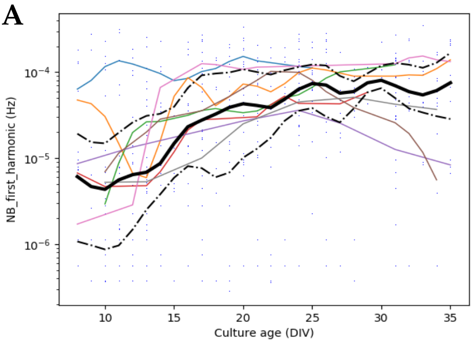

21B

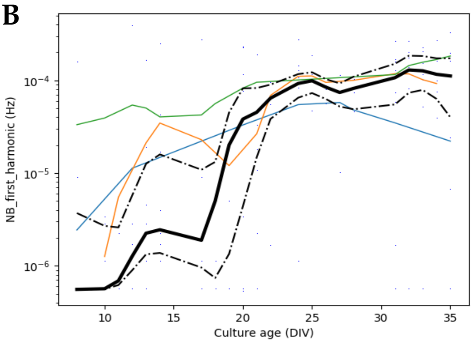

22A

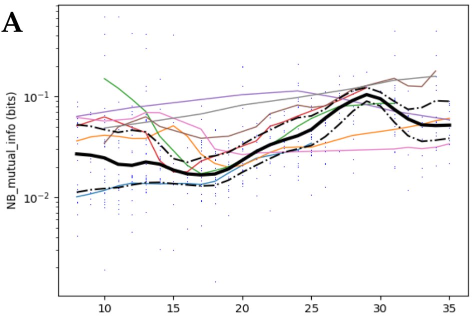

22B

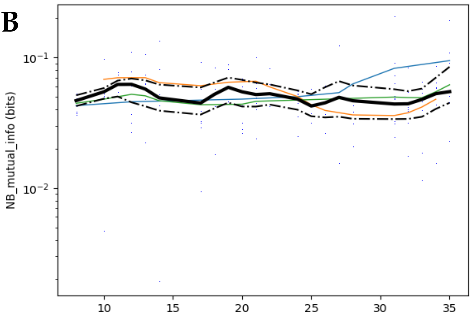

23A

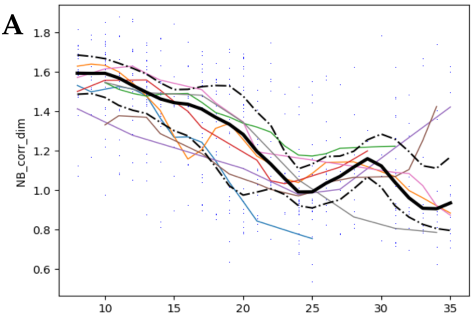

23B

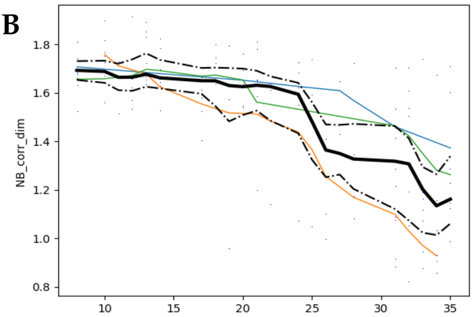

24A

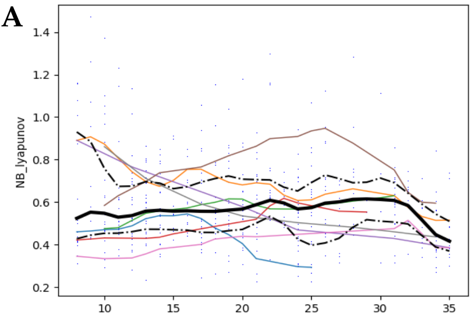

24B

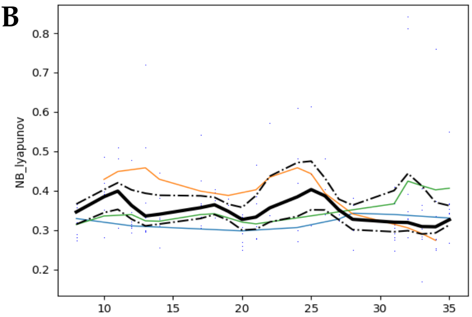

25A

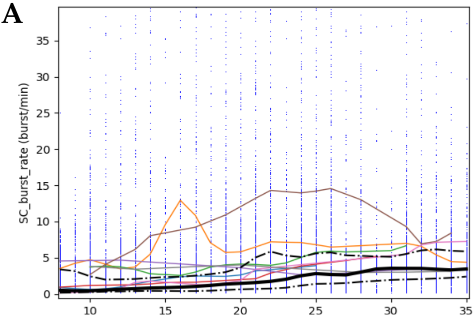

25B

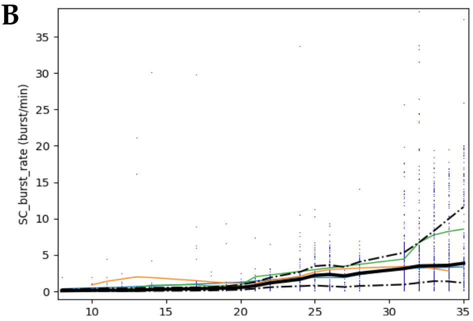

26A

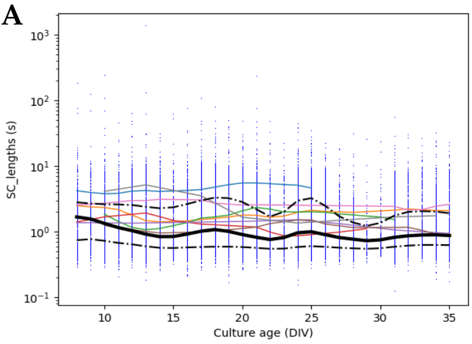

26B

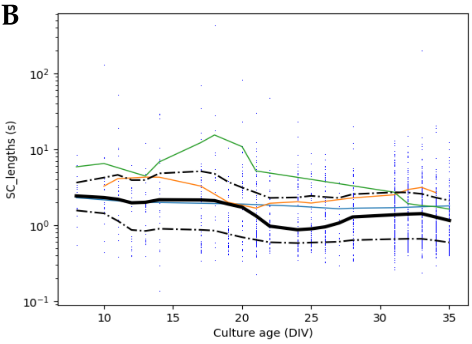

27A

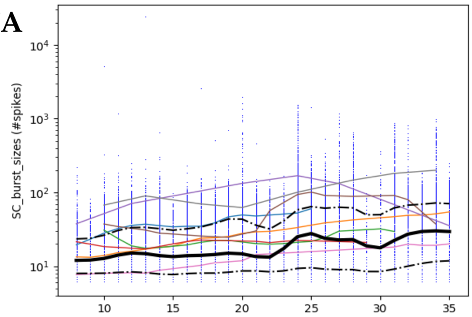

27B

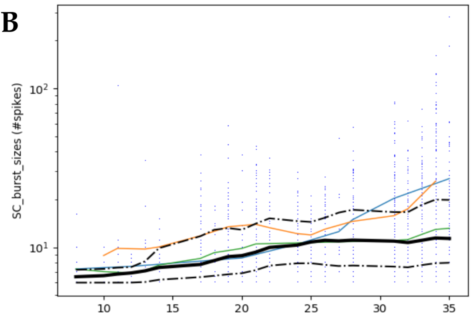

28A

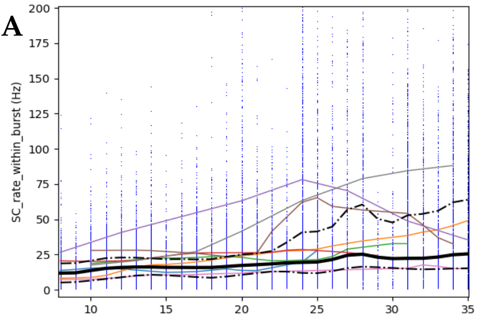

28B

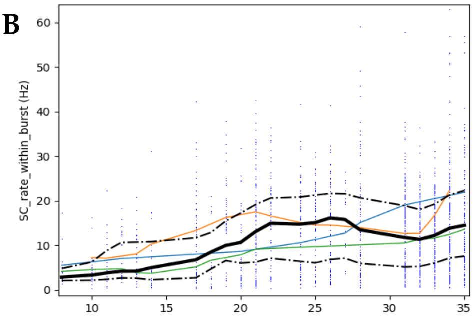

29A

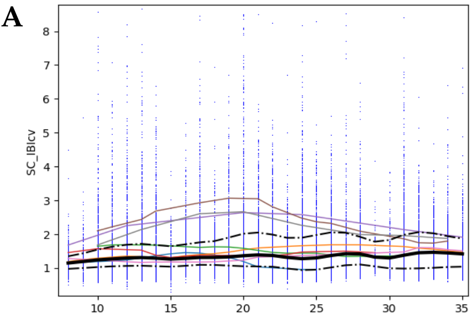

29B

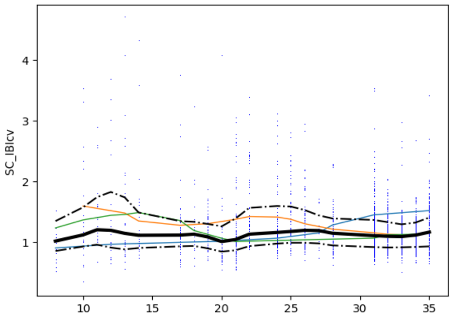

30A

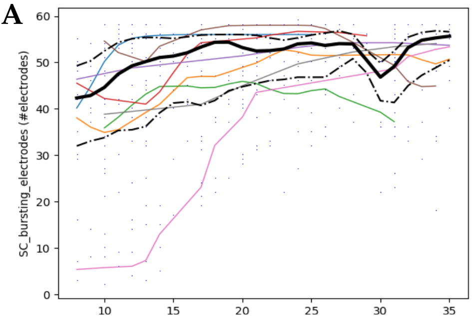

30B

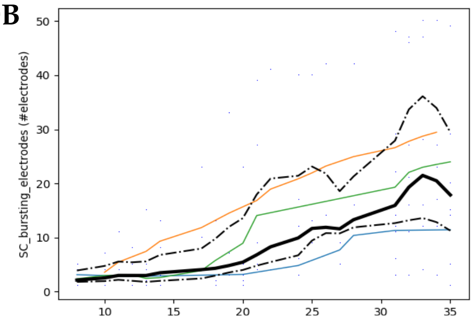

31A

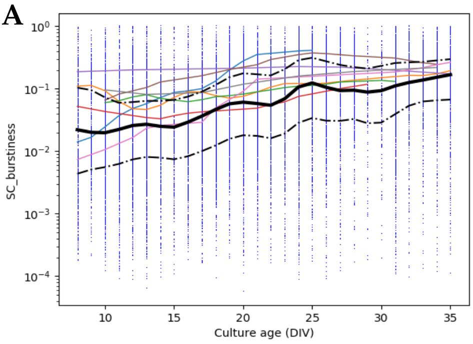

31B

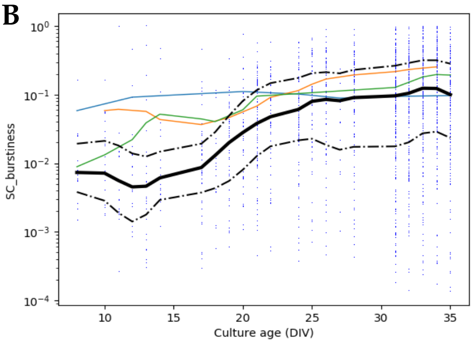

32A

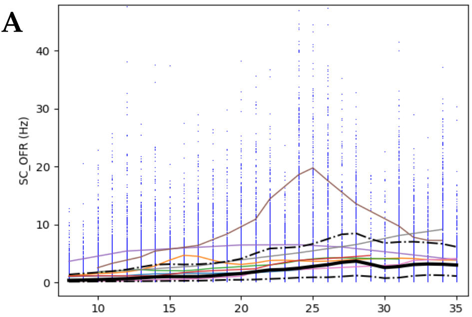

32B

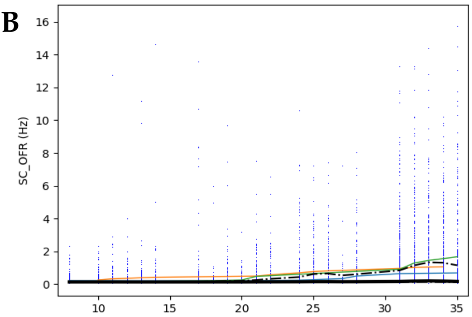

33A

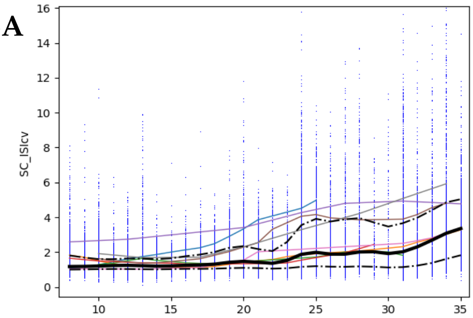

33B

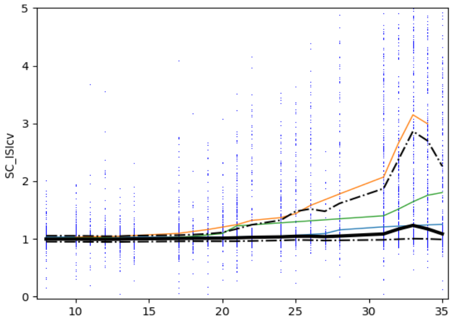

34A

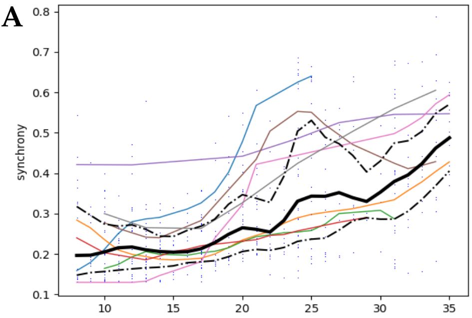

34B

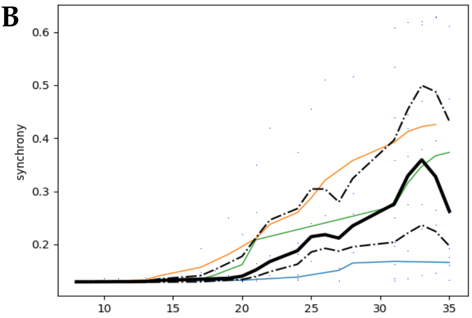

35A

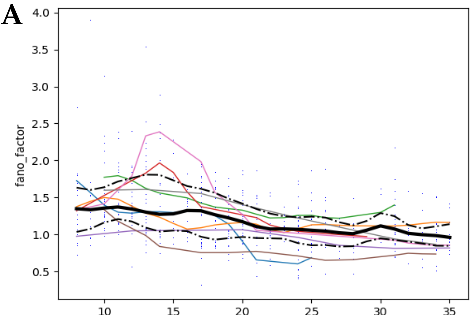

35B

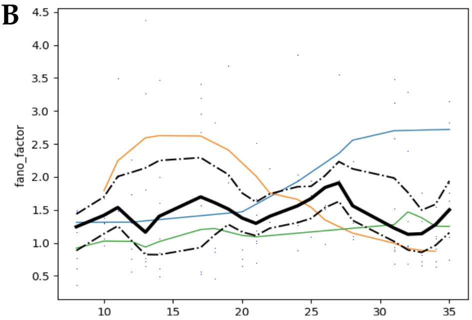

36A

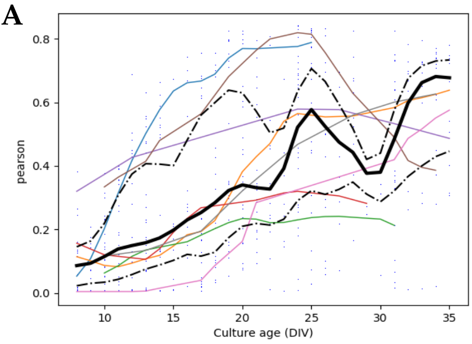

36B

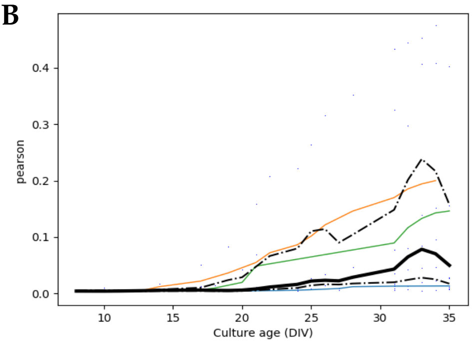

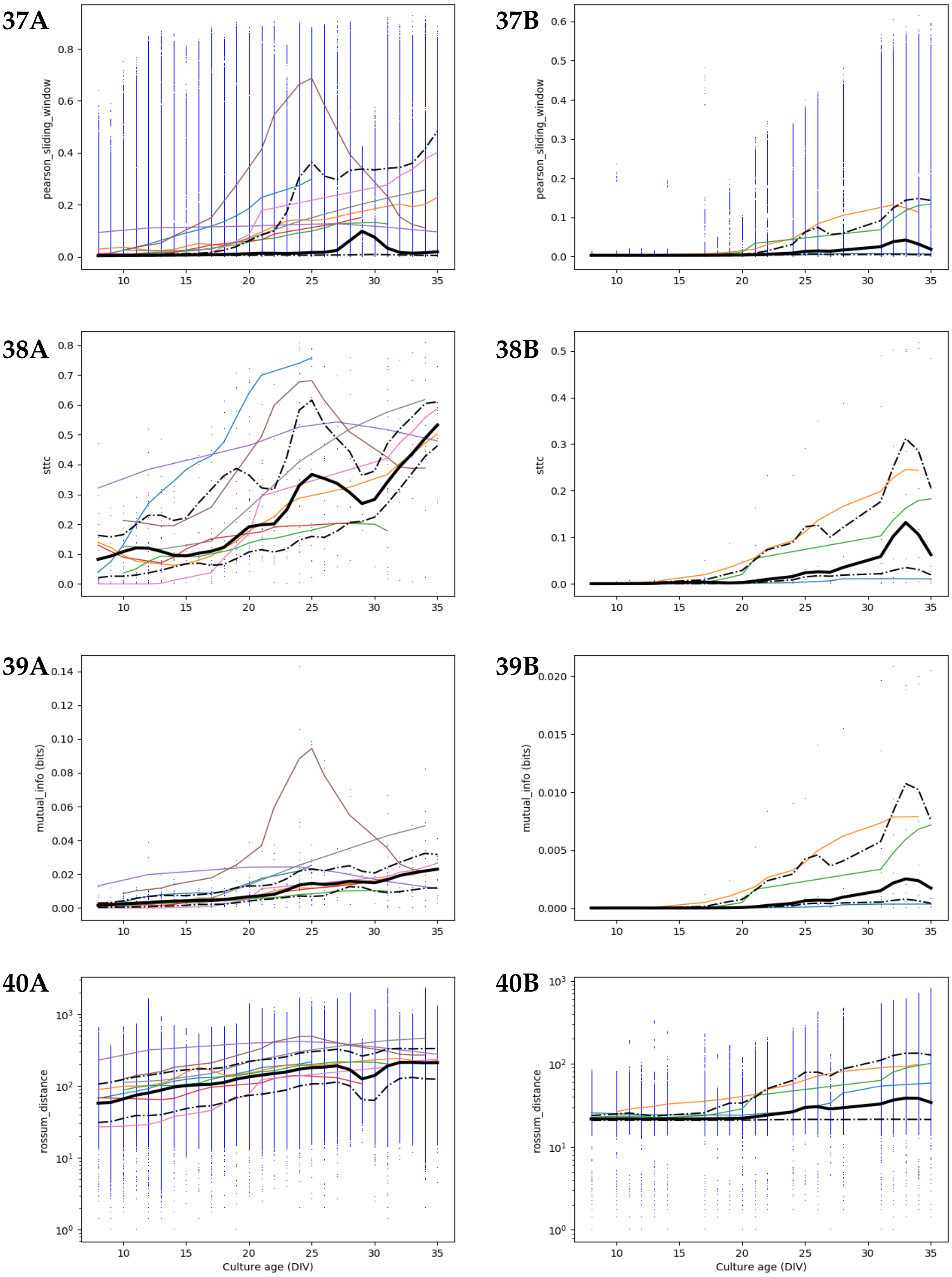

FIGURE 3.5: Plots showing the trends across the DIVs (x-axis) of all the 40 measures extracted (y-axis). The small blue dots are the samples. The black thick line represent the median calculated over all the samples belonging to one DIV and the dotted lines are the 25th and the 75th percentiles. The coloured lines are the average behaviour for each batch. All the lines are smoothed with a Gaussian kernel (SD = 1). On the left column (A) the dense cultures and on the right column (B) the sparse cultures.

Let us start describing how the spiking activity evolves during the culture maturation, focusing on how much differently the preparations behave. In the last section, we already described the **OFR** trend across the DIVs in dense cultures. Here we are going to illustrate the OFR in sparse conditions (figure 3.5.12B). Also in this case the activity increases, at least after the 20^{th} DIV, but it reaches lower averaged values (the maximum is around 0.05 kHz at the 34^{th} DIV). Conversely, the OFR does not decrease in elder cultures but keeps increasing. Moreover, it is interesting to notice how in different batches, both in dense and sparse density, the cultures show a different spiking frequency level but an overall similar trend during the development.

A related measure of the spiking activity is the ISI and the figures 3.5.13A-B show how the intervals between two spikes evolve. The CV says about the regularity of the spiking activity and an evident increasing during the development indicates the presence of more bursts. Both dense and sparse culture show an **ISI CV** increasing but in the latter the difference between young and mature cultures is more prominent because it reaches a maximum value of 4 while in the former the highest value is hardly 3. However, among the batches a diverse trend is shown.

The same measures taken from the **single-channel** recordings show a slightly different behaviour because the overall increasing of the **spike rate** across the DIVs is less accentuated (figures 3.5.32A-B). The most striking difference in the **ISI CV** can be found in the sparse cultures (figure 3.5.33B) because it does not show the same increase as in the multi-channel case.

As we already stated, the increase in ISI CV means that the spikes are more irregularly interspersed. Indeed, the spikes start to be grouped within NBs, the most prominent spatio-temporal pattern of the cultured neural network activity. In what follows we will describe how the NB shape evolves in our cultures. In the previous section, when we tried to reproduce some of the results in [55], we have already discussed about the **NB lengths**, **rising times** and **falling times** in dense cultures. In figures 3.5.2A-3A-4A can be also noticed how much variability is present among the batches since, in general, they show a quite different averaged lengths, sometimes also of an order of magnitude. Conversely, when looking at sparse cultures, no striking differences are found (figures 3.5.2B-3B-4B).

Another property to take into account in NB shape is the size, that is, the number of spikes within the NB, and the related measure of burstiness, i.e. the NB size normalized by the total number of recorded spikes. As expected, the **NB size** shows an overall increase, more evident between the 18^{th} DIV and the 25^{th} DIV in dense cultures. On the other hand, in sparse cultures the trend shows an initial raise before the 18^{th} DIV and after the 27^{th} DIV. Moreover, between the dense and the sparse cultures there is a gap of almost an order of magnitude and in both conditions the batches show different average levels. For instance, in figure 3.5.6A it is possible to see a NB batch with more than 10^4 spikes and another one that stays below 10^3 spikes.

In the normalized case (**burstiness**) the overall spikes augmentation is more evident (figures 3.5.9A-B), proving that the increasing of NB size is not only due to an higher spiking activity but actually the spikes tend to be more concentrated in NBs.

In order to get a complete image of the spatio-temporal properties of the NBs are important to check also the **number of active sites** involved in bursting activity. In figures 3.5.7A-B the overall trend for dense and sparse cultures is reported. In agreement with the NB size measurement, also the number of active electrodes seems to slightly increase. In the dense preparations the electrodes vary on average from 50 to 55, while in sparse cultures they range from 20 to 40, an expected lower number because the neurons are placed farther with respect to the electrodes. Furthermore, the trend of the sparse culture shows an unexpected drop at the 4^{th} WIV, an odd behaviour probably due to the batch variability.

In addition to the number of active sites it is also important to know how fast the electrodes are recruited during a burst, i.e. the **speed of the electrodes recruitment**. This is reported in figures 3.5.8A-B where the two trends are quite similar as both have a steady behaviour around 0.03 electrode/ms. Also in this case the batches show various trends.

Let us now compare the last measures with the **single-channel** (SC) counterparts. The **burst lengths** (figures 3.5.26A-B) show a small decrease across the DIVs and the values are slightly lower than the multi-channel (MC) case. Conversely, the **burst size** plots show an overall rising and also here the sparse cultures have less spikes within the bursts compared to the dense ones (figures 3.5.27A-B). However, if we are considering the **burstiness**, this diversity almost disappear as the values range between 10^2 and 10^1 in both cases (figures 3.5.31A-B). It is also interesting to notice the **number of bursting electrodes** in figures 3.5.30A-B. Analogously at the number of active site in NBs, also here the bursting electrodes tend to increase during the culture development and the sparse condition shows a much lower bursting activity. Also at SC level the measures show a strong batch variability. For example, in the number of bursting electrode in dense cultures, one batch shows a lower value compared to other batches in early ages and another batch tends to decrease instead of keep increasing or be steady in the elder stages of development.

Furthermore, in order to determine the NB shape we quantified not just the number of spikes but also their distribution in time. For example, in figures 3.5.5A-B the **maximum firing rate** (MFR) is reported. We have already mentioned that the number of spikes within bursts tends to increase while the burst lengths diminish. Logically, one would expect an augmentation of the firing rate in the NBs. Indeed, these figures confirm this hypothesis in both dense and sparse cultures. In the former case the NB peaks on average reach a frequency of $\sim$3 kHz (with some batches that overcome 10 kHz) and the higher frequency peak is reached after the $20^t h$ DIV. The sparse trend is lower as it barely reaches 1 kHz, it shows more homogeneity between different preparations and a more constant growing during the development.

In order to quantify the NBs variability of the MFR in one recording, we measured the **IPI CV** (figures 3.5.17A-B). In dense cultures the trend is quite stable around 1, meaning that on average the NB peaks irregularity has a SD close to the mean. Moreover, it shows a slight increase in the 2^{nd} WIV and a little drop in the 5^{th} WIV, with a similar behaviour among the batches. The level of variability in sparse culture is lower, with a more pronounced raising over the DIVs.

Through the Poincare plots we calculated also the **eigenvalue ratio** and the **number of clusters** of the **IPI** embedded in a two-dimensional phase space (cfr Section 2.3.2). The first case, reported in figures 3.5.18A-B, shows a steady behavior in all the stages of development in the dense condition (even though some batches have their own trend) while the sparse cultures show more variability, confirming somewhat the results shown in figures 3.5.17A-B. We tried to catch the variability of the NB peaks also by means of the clustering property of the Poincare plots. In figures 3.5.19A-B both the curves for dense and sparse cultures exhibit an overall increasing across the culture age in a similar range, namely, between 1 and 4.

As we have already reported in Section 2.1.2, quite many recordings present a second level organization of the spikes, i.e., the superbursts. We firstly measured the **number of peaks within a NB**, that is, how many times the overall firing rate increases above the baseline in the time-scale of a burst. The dense cultures show a slightly drop during the development, even if some batches show the opposite behaviour (figure 3.5.10A). The sparse cultures, instead, present three phases: the $2^{nd} - 3^{rd}$ and the 5^{th} WIV report a multi-peaks behaviour while in the 4^{th} WIV this phenomenon is reduced almost to mono-peak burst activity. Surely, this is due to the different behavior reported by the batches (figure 3.5.10B).

If the number of peaks overcame three we called the NB **superburst** (SB). In figures 3.5.11A-B we report the ratio of SBs over all the NBs detected in dense and sparse conditions, respectively. In accordance to what is reported in [55], the SBs are more present in really young or elder cultures although the variability among the batches is quite high.

In the **single-channel** counterpart, the firing rate property of the bursts is illustrated in figures 3.5.28A-B. In both dense and sparse conditions the overall **firing rate within the bursts** tends to slightly increase (more pronounced in sparse cultures) but not as much as it happens in the NB firing rate, confirming one more time how important is the synchronization through the network more than the single neural activity in shaping the NB patterns.

Another interesting feature that could be extracted from the recordings is the **NB rate**, i.e. how many times the network synchronizes its activity showing up the NB pattern. The figures 3.5.1A-B show an overall raising of the NB rate in both dense and sparse cultures, with a similar trend reported in the OFR plots, but unsurprisingly with a different scale as they were measured differently (kHz and burst/minute, respectively). In dense cultures it increases until the maturity (around the 22^{th} DIV) and then it shows some oscillations most likely due to the different batches behaviour. On the other hand, sparse cultures trend shows a more regular increasing across all the DIVs.

One related measure to the NB rate is the **IBI**. As for the case of the IPIs, we measured this quantity in three ways, through the **CV** (figures 3.5.14A-B), the **eigenvalue ratio** (figures 3.5.15A-B) and the **number of clusters** (figures 3.5.16A-B). The last two measures were extracted from the Poincaré plots. In dense cultures the IBIs show a steady variability with respect to the mean while in sparse culture seems to slightly increase during the culture development. This behavior is also reflected in the eigenvalue ratio trends. The number of clusters tend to increase across the DIVs in both dense and sparse cultures, with a higher rising slope in the young cultures. Hence, the rate of the bursts seem to increase during the development with an almost constant IBI variability or with a small increment, in particular in early ages.

As for the spiking frequency, also the **SC burst frequency** does not show an abrupt increment during the development (figures 3.5.25A-B); in fact, the ontogeny of the NB patterns in the network is mostly due to the more coordinated activity of the neurons, as we will also see later when analysing the correlation measures. Likewise, the **IBI CV in single electrodes** shows similar constant trend around 1 in both density conditions (figures 3.5.29A-B), trend not in accordance with the MC case.

In order to get the whole picture of the bursting dynamics in an one dimensional time series we calculated the **NBRP**, i.e. the global instantaneous activity of the network. From the NBRP we extracted some more 'sophisticated' measures, as the **first minimum of the autocorrelation** (figures 3.5.20A-B) and the **first harmonic of the power spectra** (figures 3.521.A-B). The autocorrelation is the similarity between two slided copies of the time series as a function of the time lag between them. Hence, the first minimum indicates after how much time the signal will lose much of the self-similarity and, eventually, the periodicity of the signal. Both in dense and sparse cultures this value increases until the maturity of the culture to around 5 s in both conditions, and then is subjected to a small drop. The first harmonic indicates the intrinsic frequency of the signal and, in agreement with the rate results already reported, its value raises all over the development with a more abrupt increment from the 3^{rd} to the 4^{th} WIV, where in the sparse cultures the frequency makes a jump of almost two order of magnitude (from 10^{-6} to 10^{-4} Hz), one order more than in dense cultures (from 10^{-5} to 10^{-4} Hz).

Moreover, we embedded the NBRP signal in a two dimensional phase space, building the so called **Poincare plots**, and we extracted other measures using some tools adapted from chaos theory that permitted us to quantify the neural network activity from a dynamical system's point of view. Firstly, we calculated the **mutual information** between the original and the 500 ms delayed signal (figures 3.5.22A-B), telling us how much correlation exists between them. In dense culture the value shows an increment between the 18^{th} and the 30^{th} DIV while in sparse cultures we did not report any relevant changes during the development.

Afterwards, from the attractor obtained in the phase space we extracted two measures, the correlation dimension and the Lyapunov exponent, useful to quantify the geometrical and dynamical properties of the attractors, respectively. In figures 3.5.23A-B the **correlation dimensions** decrease across the DIVs in both dense and sparse cultures, but the latter seems to have a slightly higher overall fractal dimension of the attractors (dense cultures span from 1.6 to 1.0 while sparse from 1.7 to 1.2). In figures 3.5.24A-B the **Lyapunov exponents** are reported and in both density conditions the values seem to be almost steady during culture development without any striking overall changes. Just the level in sparse cultures, which ranges between 0.3 and 0.4, is little bit lower than in dense cultures, which is instead around 0.5.

One of the most important factors in the NB activity is the synchronization of the neural activity among the network. The following measures try to quantitative estimate this pivotal mechanism in neural networks that is at the base of all the main brain functions. One simple measure that try to quantify the activity synchrony is the **Fano factor**. However, as it is possible to see in figures 3.5.35A-B, it does not seem to catch the right evolution of the network as the value is quite steady across all the DIVs, contrary to what we have seen from other NB measures.

On the other hand, the **synchrony** measure taken form [13] behaves as expected because in both dense and sparse cultures the general synchrony level increases during the culture maturation (figures 3.5.34A-B). The major difference between the two culture densities can be found at the beginning of the development where the sparse neural networks do not show any coordinate activity until the 20^{th} DIV while the dense cultures present a little level of synchrony already at early DIVs.

Then, we also checked the conventional **Pearson correlation** coefficient, calculated from the entire recording (figures 3.5.36A-B) and with a sliding window pattern (figures 3.5.37A-B). The former tends to increase even if at the last two WIVs shows some irregularity due to the anomalous decreasing behaviour of some batches. The latter slightly increases, mostly in the last two WIVs and the values are always quite low, as they barely reach a correlation of 0.1. Indeed, the Pearson correlation is usually not suitable for sparse data like the spiking recordings, whose have long period of really low activity between two consecutive NBs. This drawback is particularly visible in the sliding window approach where the correlations are quite low because the NB is present only in a small percentage of all the recording while most of the time neurons are uncorrelatedly firing.

As already mentioned in Section 2.3.3, a more suitable measure for this kind of data is the **spike time tiling coefficient** (STTC), shown in figures 3.5.38A-B. It has a similar behavior of the synchrony, at least in dense cultures because in the sparse condition the coefficient just achieves a value of 0.1 in the elder cultures.

The last two considered correlation measures are the **mutual information** (figures 3.5.39A-B) , a measure similar to the Pearson correlation but that it takes into account also non-linear terms, and the **van Rossum distance** (figures 3.5.40A-B). In both cases the measures do not show a great variability across the DIVs but only a small increment in the elder cultures. Moreover, also the difference between dense and sparse cultures is moderate, although the dense counterpart reaches higher values, as expected.

3.1.3 Class Separability

After have qualitatively characterized all the extracted measures, now we will check if the classes present in the data, namely density, WIV for dense and sparse cultures, batch for dense and sparse cultures, are linearly separable. Specifically, the distribution differences and the PCA technique will be used for this scope. However, first we need to choose the samples for each class. The table 3.1 reports the number of samples for each class in every condition. In the bucket list below it is summarized how the samples where chosen based on the confounding factors present in the data. For a better understanding of how the choice were made refer to the table 2.3.

- When considering the density condition, namely dense and sparse cultures, we included the samples from the 8^{th} to the 35^{th} DIV and the batches 5,6,7 which are both present in sparse and dense cultures. For reducing the confounding factors we considered just the last two WIVs ($22^{th} - 35^{th}$ DIVs) and only the batch 6, the one with more samples.

- In the case of culture age, we divided all the DIVs in 4 classes, one for each WIV. In each density condition we considered all the batches or just one (batch 2 for dense and batch 6 for sparse) when trying to reduce the confounding factors.

- When the classes were divided according to their batch (batch 1-8 in dense condition and 5-7 in sparse condition), we chose the samples in two ways: 1) with all DIVs in the data base; 2) with only the last two WIVs.

When we wanted to reduce the confounding factors (CF) in the density and batch classes we picked only the samples in the last two WIVs because it is usually believed that from the third WIV the cultures are mature. It should be noticed that when the data are strongly stratified, as in our case, in order to reduce the variability for obtaining a more realistic and faithful classification accuracy we would meet another problem, the overfitting due to the scarcity of samples. However, determining the minimum number of necessary samples is hard because it depends on the complexity of the classifier and the number of features. In fact, if we look at table 3.1, the number of samples in the case without CFs is between one half and one fifth of the subsets with CFs. Also for this reason we could not stratify anymore the data, for example just considering few DIVs in density and batch classes.

	Density	**WIV Dense**	**Batch Dense**	**WIV Sparse**	**Batch Sparse**
Samples per class (w/ CF)	dense: 86 sparse: 125	2nd wiv: 141 3rd wiv: 123 4th wiv: 101 5th wiv: 72	batch 1: 69 batch 2: 137 batch 3: 96 batch 4: 26 batch 5: 21 batch 6: 37 batch 7: 28 batch 8: 23	2nd wiv: 38 3rd wiv: 28 4th wiv: 21 5th wiv: 38	batch 5: 21 batch 6: 48 batch 7: 56
Total	221	437	437	125	125
Samples per class (w/o CF)	dense: 18 sparse: 27	2nd wiv: 40 3rd wiv: 37 4th wiv: 30 5th wiv: 30	batch 1: 10 batch 2: 60 batch 3: 41 batch 4: 10 batch 5: 12 batch 6: 18 batch 7: 10 batch 8: 12	2nd wiv: 12 3rd wiv: 9 4th wiv: 15 5th wiv: 12	batch 5: 12 batch 6: 27 batch 7: 20
Total	45	137	173	48	59

TABLE 3.1: For each class the number of samples is reported. The upper and the lower part of the table report the samples with and without the confounding factors, respectively.

The first step of the statistical characterization of the dataset is to check the class separability by determining the distribution differences between the classes. We calculated the p-value through the **Kolmogorov-Smirnoff test** (KS). In table 3.2 the results are reported for each class. In order to get more faithful results, the confidence level (0.05) was divided by the number of comparisons (Bonferroni correction). The most striking outcome is that the majority of the distributions do not show any significant differences (p-value higher than the corrected level of confidence) and, in general, when the confounding factors are discarded the distributions do not tend to be more dissimilar. This can be explained by the fact that the samples are not linearly separable (as we will see better when visualizing the sample in the feature space), when considering one measure at once. In order to separate the class we need to consider more features together and just their interplay will enable us to classify the data. Moreover, we should also remember that when removing the variability factors the number of samples is drastically reduced and this can affect the distributions, biasing the results. Afterwards, we will discuss more specifically about the measures that seem to separate some distributions. Hence, in what will follow we will not talk about the measures that do not show any discriminatory power.

In general the single-channel measures seem to have more discriminatory power maybe because at the electrode level the activity can be more variable and thus distinguish our classes. At network level the activity is somehow averaged out and the differences between the classes could be more tricky to detect using just one measure. As far as it is concerned the spiking activity measures, as the OFR, the distributions seem to be diverse in density and batch in the case with the CFs, while also the WIVs classes are separable when we took out part of the CFs. The ISI CV shows some promising results only in the latter case.

MEASURE	**Density**	**WIV Dense**	**Batch Dense**	**WIV Sparse**	**Batch Sparse**
Class	2 (1)	4 (6)	8 (28)	4 (6)	3 (3)
OFR	1 | 0	0 | 0	3 | 1	1 | 0	0 | 0
NB ISI CV	0 | 0	0 | 0	0 | 0	0 | 0	0 | 0
NB Peaks	1 | 1	0 | 0	2 | 1	0 | 0	0 | 0
NB Lengths	0 | 1	0 | 0	0 | 0	4 | 2	0 | 1
NB Rising	0 | 1	0 | 2	0 | 5	3 | 0	1 | 1
NB Falling	1 | 1	0 | 0	0 | 1	4 | 3	0 | 0
NB Electrodes	1 | 1	0 | 0	0 | 0	3 | 3	0 | 0
NB Rate	0 | 0	0 | 0	0 | 0	2 | 0	1 | 0
NB Elect. Speed	0 | 0	3 | 3	10 | 6	3 | 0	0 | 0
NB Size	1 | 1	0 | 0	0 | 2	4 | 3	0 | 0
NB Burstiness	1 | 0	0 | 0	0 | 2	2 | 0	1 | 0
NB S.burstiness	1 | 1	0 | 0	1 | 0	0 | 0	0 | 0
NB n. Peaks	0 | 0	0 | 0	0 | 0	3 | 0	1 | 1
NB IBI CV	0 | 0	0 | 0	0 | 0	0 | 0	0 | 0
NB IPI CV	1 | 0	0 | 0	0 | 0	0 | 0	0 | 0
NB IBI Eigen. Ratio	0 | 0	0 | 0	0 | 0	0 | 0	0 | 0
NB IBI Clusters	0 | 0	0 | 0	0 | 0	0 | 0	0 | 0
NB IPI Eigen. Ratio	0 | 0	0 | 0	0 | 0	0 | 0	0 | 0
NB IPI Clusters	0 | 0	0 | 0	0 | 0	0 | 0	0 | 0
NB 1st Harmonic	0 | 0	0 | 0	4 | 0	0 | 0	0 | 0
NB Autocorr. 1st min	0 | 0	0 | 0	0 | 0	0 | 0	0 | 0
NB Lyapunov	1 | 0	0 | 0	1 | 0	0 | 0	0 | 0
NB Corr. Dim.	0 | 0	0 | 0	0 | 6	0 | 0	0 | 0
NB Mutual Info	0 | 0	0 | 0	0 | 0	0 | 0	0 | 0
SC ISI CV	0 | 0	2 | 1	2 | 1	3 | 3	2 | 2
SC OFR	1 | 1	1 | 0	6 | 7	1 | 0	0 | 0
SC Lengths	0 | 0	0 | 0	0 | 0	0 | 0	0 | 0
SC Burst Rate	1 | 1	2 | 2	16 | 14	2 | 0	0 | 1
SC in-Burst Rate	1 | 1	3 | 3	12 | 10	1 | 1	0 | 0
SC Burst Size	1 | 1	0 | 0	0 | 3	1 | 2	0 | 0
SC Burstiness	0 | 0	0 | 0	1 | 0	2 | 2	0 | 0
SC IBI CV	1 | 1	0 | 0	14 | 8	1 | 0	0 | 0
SC Bursting Elect.	0 | 0	2 | 0	1 | 0	0 | 0	0 | 0
Synch	1 | 0	1 | 0	5 | 0	2 | 0	2 | 0
Fano Factor	1 | 0	0 | 0	0 | 0	0 | 0	0 | 0
Pearson	1 | 0	3 | 1	8 | 2	1 | 0	0 | 0
Pearson (SW)	1 | 0	2 | 0	1 | 0	2 | 1	2 | 2
Mutual Info	1 | 0	0 | 0	0 | 0	0 | 0	0 | 0
STTC	1 | 0	0 | 0	0 | 0	0 | 0	1 | 1
van Rossum	1 | 1	3 | 1	19 | 19	3 | 3	0 | 1

TABLE 3.2: Table with the number of different distributions for each classes. The first row reports the number of distributions for each condition and in the brackets the number of comparisons, used in the Bonferroni correction when performing the pair-wise Kolmogorov-Smirnoff test . The remaining rows show the number distribution pairs with p-values lower than 0.05 divided by the number of comparison. Two cases were reported, with and without confounding factors, on the left and on the right, respectively.

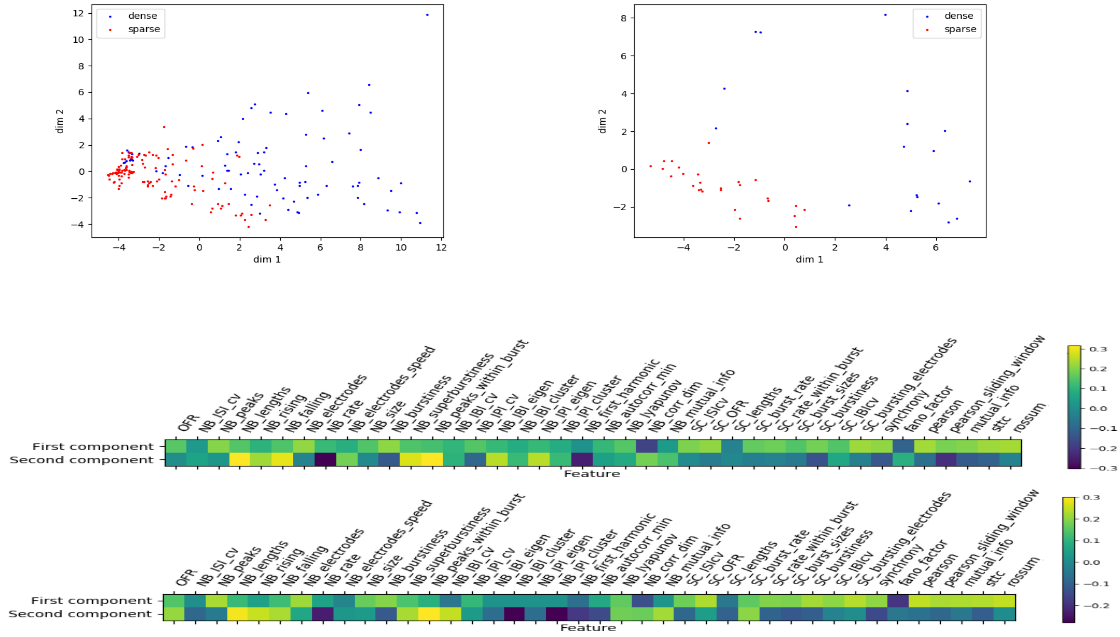

FIGURE 3.6: Upper plots: The first two Principal Components. The samples are divided according to the density. On the left the plot with the confounding factors , on the right with reduced confounding factors. Lower part: the correlation of the measures that contribute to the first two principal components for two conditions, with (upper) and without (lower) CFs.

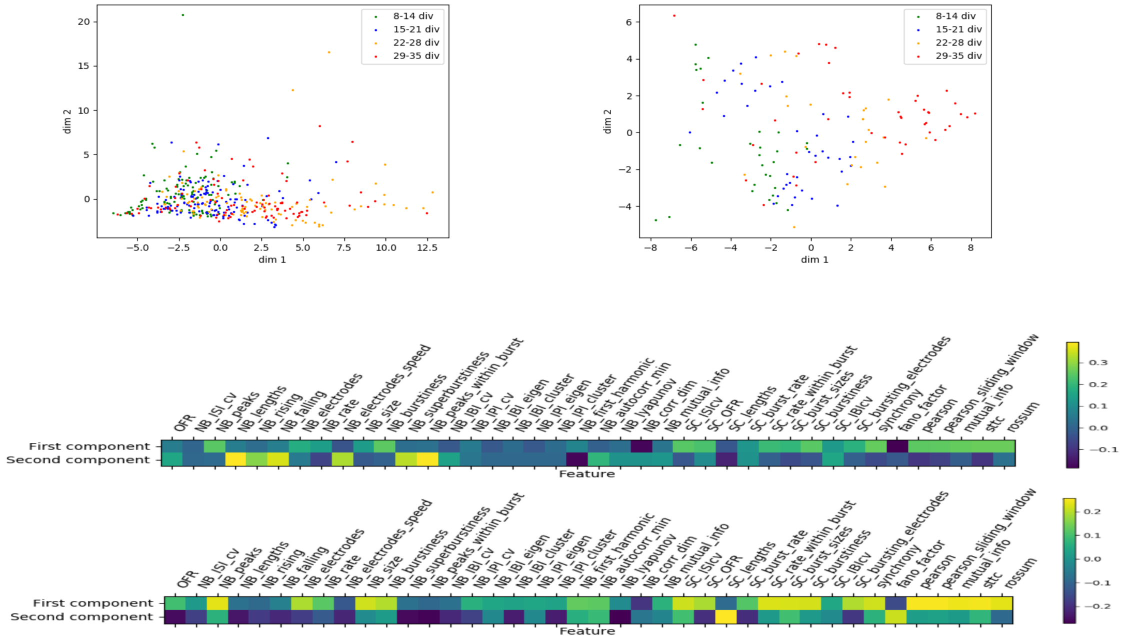

FIGURE 3.7: Upper plots: The first two Principal Components. The samples are divided according to their WIV in dense cultures. On the left the plot with the confounding factors, on the right with reduced confounding factors. Lower part: the correlation of the measures that contribute to the first two principal components for two conditions, with (upper) and without (lower) CFs.

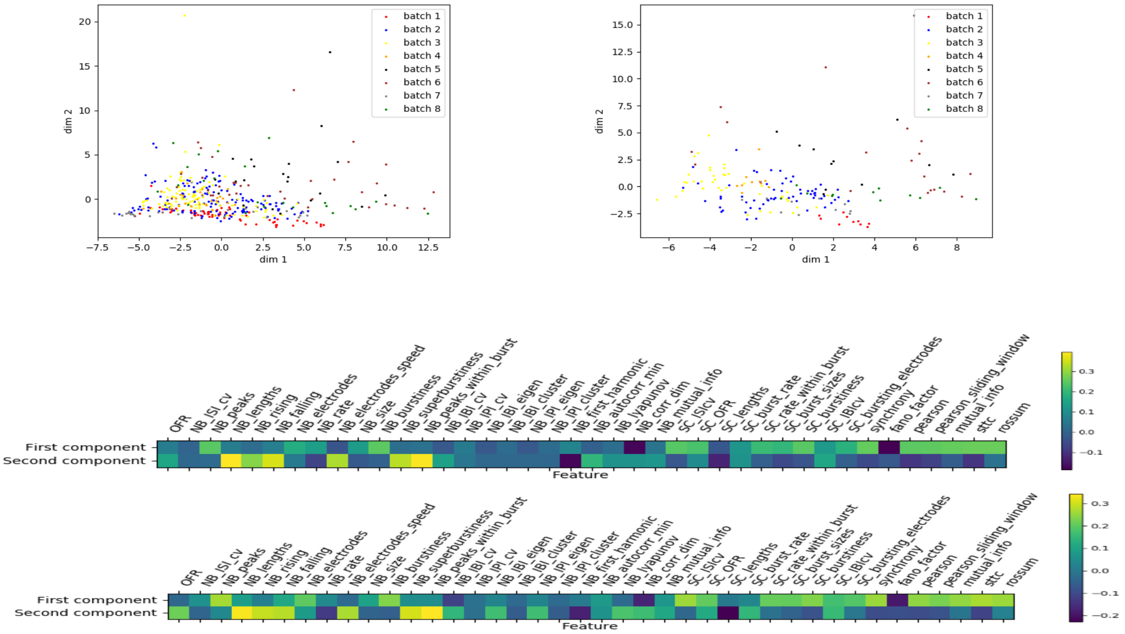

FIGURE 3.8: Upper plots: The first two Principal Components. The samples are divided according to their batch in dense cultures. On the left the plot with the confounding factors, on the right with reduced confounding factors. Lower part: the correlation of the measures that contribute to the first two principal components for two conditions, with (upper) and without (lower) CFs.

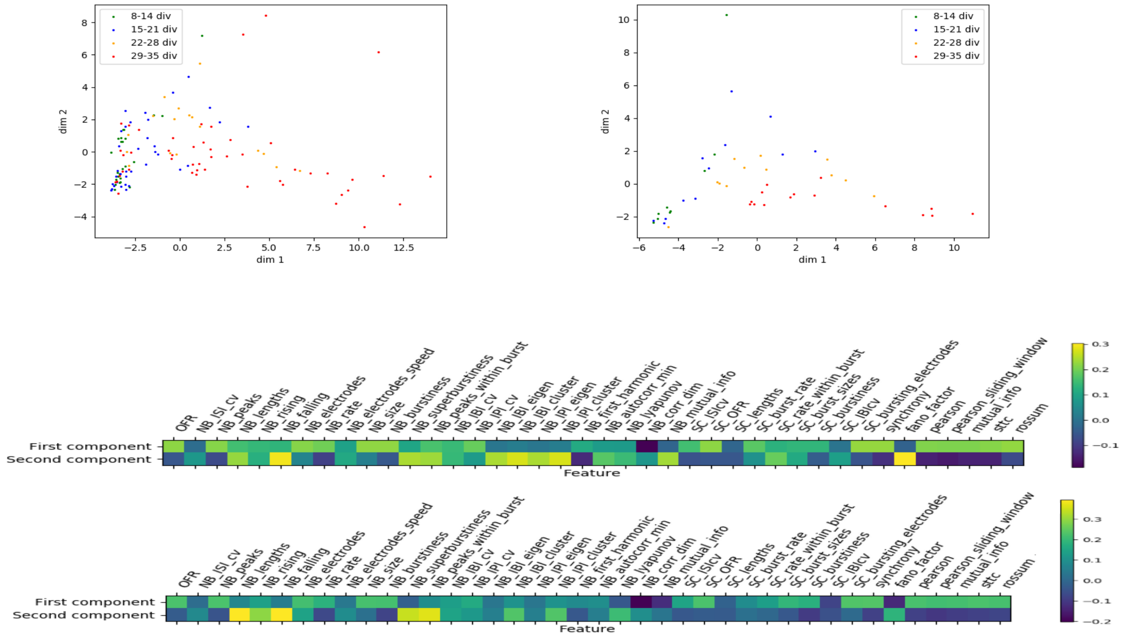

FIGURE 3.9: Upper plots: The first two Principal Components. The samples are divided according to their WIV in sparse cultures. On the left the plot with the confounding factors, on the right with reduced confounding factors. Lower part: the correlation of the measures that contribute to the first two principal components for two conditions, with (upper) and without (lower) CFs.

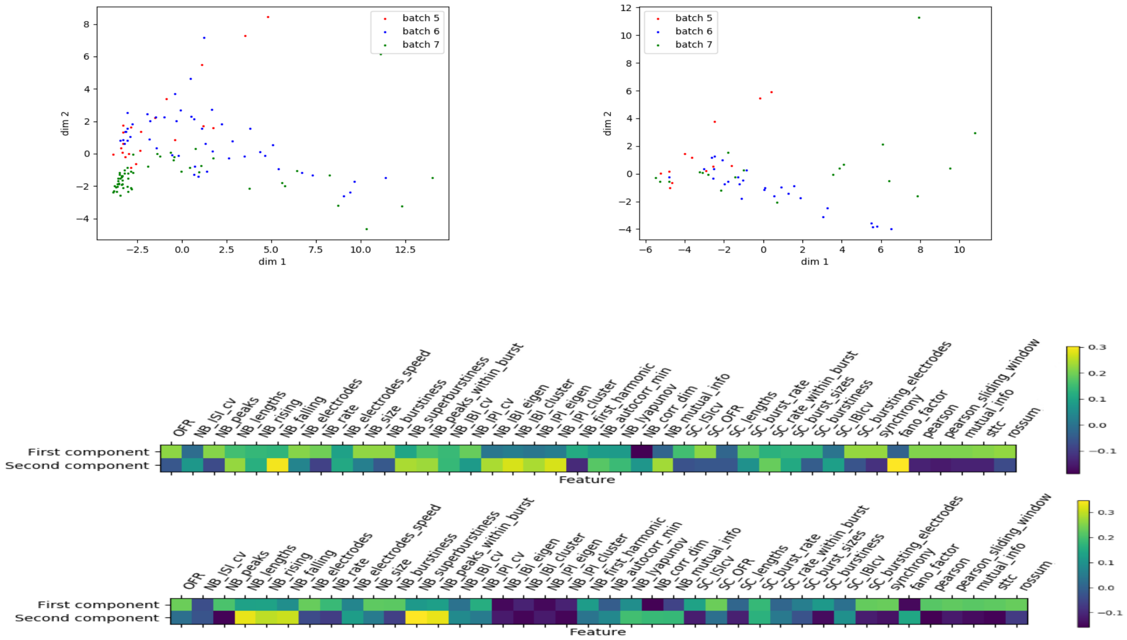

FIGURE 3.10: Upper plots: The first two Principal Components. The samples are divided according to their batch in sparse cultures. On the left the plot with the confounding factors, on the right with reduced confounding factors. Lower part: the correlation of the measures that contribute to the first two principal components for two conditions, with (upper) and without (lower) CFs.

It is interesting to notice how the IBI- and IPI-related measures (CV, eigenvalue ratio and number of clusters) in the multi-channel case show the worst results. Also the NBRP-related measure do not seem good in significantly distinguish the classes, as just in the batch dense class we calculated some p-values below the level of confidence. Better results are given by the measures that describe the shape of a NB (e.g. size, length) even if we do not consider the CFs the distributions do not show considerable improvements. For example, good results are shown by the electrode speed measure in dividing the WIV and Batch (only dense) classes. However, the single-channel counterparts show better results in all the classification type but not in the batch sparse case. For instance, the burst rate and the frequency within the burst present good discriminatory power in all the classes unless the batch sparse case. Moreover, the multivariate measures (e.g. correlations) present quite well separated distribution, with the van Rossum distance showing the best results and the Fano factor and the mutual information the worst ones.

The first classification approach was to look at the distributions, studying individual contribution of each measure. However, we could not come up with any satisfactory results seen the complexity of the data we are dealing with. Below, the results obtained with **PCA** are illustrated. PCA was mostly useful to see if when considering all the measures together the samples were linearly separable. Therefore, we plotted the samples in the N dimensional space, where N is the total number of features, and then projected the data in the first two dimensions that show more variability (Principal Components), to visually see if the samples clustered in their belonging classes.

In figure 3.6 the two upper plots show the scatter of the samples divided by their **density** condition, that is, between dense and sparse cultures. On the left the classes slightly overlap while on the right the classes are more separated although the number of samples is highly reduced. The lower plots show the level of correlation between the measures involved in the first two principal components. The two cases, with or without the confounding factors, are quite similar. In the first component the measures seem to be almost all positively correlated, in particular the multivariate measures. However some measures present anticorrelation, such as the correlation dimension and Fano factor. The second component is more complex, having some features that are correlated, as the NB lengths, superburstiness and the peak within the bursts and some that show opposite behaviour, e.g. NB rate and the first harmonic. Also in this case the multivariate measures have similar trend.

The PCA dimensional reduction for the **WIV dense** classes is reported in figure 3.7. In the presence of the CFs the four classes are hardly distinguishable and when we removed the CFs the classes seem to be more separated even if the overlapping did not completely disappear. As far as it is concerned the contribution of each measures in the first two principal components, in the first component the measures do not show a strong correlation between them except for the multivariate measures that are positively correlated, and correlation dimension and Fano factor that are negatively correlated. In the second component we could find a group of measures, as the NB lengths and superburstiness that are correlated, and a second group of anticorrelated measures, as the multivariate ones and the first harmonic. In the case without CFs the trend just slightly changes. The multivariate and some NB measures (peaks, size, burstiness) show correlation and other anticorrelation (Fano factor, SC length and correlation dimension) and in the second component almost all the measures present the same trend (anticorrelation) with some exception (e.g. Fano factor and SC length).

The figure 3.8 illustrates the first two principal components in case of **batch dense** classes. Also here the different batch classes are overlapping with some reduction in the case with lower CF levels. However, the lower number of samples and the higher number of the classes (8) do not permit a good definition of the class clusters. The graphs that show the features contribution in the first two components for the sample choice with and without CFs, are quite similar. Similarly at the previous plots, in the first principal component the multivariate and some of the single-channel measures are positively correlated with an opposite trend for the Fano factor and the correlation dimension. In the second component we could identify two groups of measures with different correlation, the NB measures (lengths and superburstiness) and the multivariate with the SC length and the first harmonic.

Then we looked at the sparse recordings and it held the same considerations made for the dense classes. In figure 3.9 it is possible to notice the usual overlapping of the four **WIV sparse** classes with an improvement when discarding the CFs. The two principal components show the correlation for the multivariate measures with the opposite behaviour of the Fano factor. In the first component we see also a similar trend for the NB measures with a discording behaviour of the correlation dimension, while in the second component we notice a similar correlation just for the IPI- and IBI-related measures and no underlying patterns in the other NB measures. When reducing the CFs the correlation differences seem to be smoother, that is, the measures tend to be more uncorrelated with respect to the case with more

CFs, although the usual motives are still present.

The last figure 3.10 reports the **batch sparse** classes. The dimensionality reduction shows that some classes (e.g. batch 7) are quite separated from the rest of the samples. When removing the CFs the situation does not show a significant improvement, probably due to the lack of enough samples. The relation between the measures shows the already reported patterns, i.e. same correlation for the multivariate measures (except for the Fano factor), positively correlation for the NB measures with different trend for the IBI- and IPI-related measures and a stronger deviation for the correlation dimension. In the second component the main difference can be found in the fact that the NB-related measures seem to be more uncorrelated. Similar behaviors are present in the case with reduced CFs in which a slightly increasing of the anticorrelated measures is reported.

In summary, in all the classification types we could identify a strong correlation between the multivariate measures (with the exception of the Fano factor that shows a discordant behaviour also in the developmental trends reported in section 3.1.2) as expected because all of them quantify the level of the synchrony in the spiking activity. Moreover, an expected result was the correlation among the IBI- and IPI-related measures and among the measures that characterize the size and shape of the NB, as the NB length, rising time and falling time. It is also interesting the opposite behavior often shows by the correlation dimension of the Poincare plot attractors, that can be explained looking at the figures 3.5.23 where clearly the correlation dimension tends to decrease.

Class	density	wiv dense	batch dense	wiv sparse	batch sparse
w/ CF	50.97%	42.28%	42.28%	54.95%	54.95%
w/o CF	54.78%	48.88%	43.53%	55.25%	54.93%

TABLE 3.3: The percentage of variability explained by the first two principal components in each type of classification. The first and the second row report the values for the classes with and without confounding factors, respectively.

The table 3.3 reports the percentage of variability explained by the first two principal components. The best score is given by the sparse cases even if they do not show an improvement when the CFs are taken out. Conversely, the samples chosen to classify the densities, the WIVs and the batches dense class show higher percentages of explained variability without the CFs. This confirm also what we visually inspected from the PCA plots in figures 3.6-10. In fact, in the sparse cases the classes separability did not visually improved in the reduced CFs plots. As we already stated, this problem is likely due to the lack of data, an issue more intense in sparse cultures.

3.2 Classification

Using the same sample choices of the previous section for studying the distributions and the class segregation, we will show the classification results, performed with two methods, the K-means clustering (KMC) and the Random Forest (RF), an unsupervised and supervised technique, respectively.

3.2.1 K-Means Clustering and Random Forest

Firstly, we tried to classify the data using an unsupervised method, the **k-means clustering**. In table 3.4 the classification accuracies are reported. We checked the degree of similarity between the clusters determined by the algorithm and the real classes. The clusters were found without any hint about the real structure of the classes but just studying the closeness of the samples in the features space. Hence, in order to compute the accuracy, we assigned the predicted label to the k-means clusters the same label of the nearest sample to the cluster centers. We also compared this results with the probability to individuate the correct class by chance, reported in the first row of table 3.4. The initialization of the cluster centers is random so we set different seeds and run again the clustering algorithm to see how the performance changed. However, the accuracy did not show different values with different initialization seeds, so for this reason in table 3.4 is not reported any accuracy error.

In the table two values for each classification are shown, one with CFs and one with reduced CFs, the same sample subsets used in the previous section. In general, the accuracies are not really good compared to classification by chance. For example, in the density classification the accuracy is below 0.5 and in the other cases the results are only slightly higher than the random accuracy. When discarding most of the CFs one would expect a better result but actually the accuracies did not improve that much or, as in the case of WIVs classification it got worst. This can be due to the low amount of data after removing the CFs. In fact, given the number of features and the number of classes, the samples could not be enough numerous to correctly distinguish the classes. For example, in the case of the WIV sparse the accuracy drop from 0.49 to 0.19, below the accuracy given by chance. Just when we try to classify dense and sparse samples the accuracy increased, passing from 0.41 to 0.76, above the value given by chance.

Class	density	wiv dense	batch dense	wiv sparse	batch sparse
by chance	0.5	0.25	0.13	0.25	0.33
KMC (CF)	0.41	0.33	0.16	0.49	0.32
KMC (no CF)	0.76	0.28	0.27	0.19	0.46
RF (CF)	0.91 ± 0.05	0.74 ± 0.05	0.89 ± 0.02	0.70 ± 0.05	0.90 ± 0.07
RF (no CF)	1.0 ± 0.0	0.80 ± 0.07	0.93 ± 0.04	0.76 ± 0.09	0.80 ± 0.14

TABLE 3.4: Accuracies of the k-Means clustering (KMC) and random forest (RF) classifications, for the samples with and without CFs. The first row reports the accuracy for classifying the samples by chance. In the RF classification the accuracies are written in the form mean ± SD, determined after running the algorithm for 5 times.

Subsequently, in order to predict with more precision the classes we performed the **random forest classification**. We followed the analysis unrolled in [8] where the authors examined the neural network ontogeny studying the recordings made in multi-well MEA over the first 12 DIVs. They selected only 12 features to describe the network activity and built a random forest classifier to predict the age of each well. In this case a supervised method should yield higher value of accuracy. In fact, as it is possible to see in the last two rows of table 3.4 we fulfilled better performances, with values ranging from 0.7 to 1, all clearly above the accuracy given by chance. We set up the random forest classifier fixing the random state for reproducibility aims, and the number of decision tree at 200 to get rid as much as possible of overfitting issues.

For the same reason, we repeated the classification partitioning the data between training and test sets using a stratified 5-fold cross validation method. That is, we repeated the classification for five times, each time we randomly split the samples in five parts containing the same proportionality of the samples for each class. This technique should lead to a less biased results. In these 5 subsets, four were used for training the classifier and one for testing it. We did not use an higher k-fold because our dataset was not big enough. Already with k=5 we could average out the biases due to a wrong train-test portioning, containing to a low level the computational times. As we iterated the RF five times, the mean and SD was computed.

The accuracies are around 0.9 for the density and batch classification, while for the WIVs around 0.7. This is probably due to the higher variability within this classes that comprise cultures belonging to different DIVs. This is a proof of how the cultures are subjected to variability even in short range of DIVs. However, due to the lack of recordings we could not shrink the dataset anymore, for example, trying to classify specific culture ages. In the last row of table 3.4 the results with reduced CFs are illustrated. Except for the odd behaviour of batch sparse classes, the classification performances improved. Interestingly, the density classification show a perfect output, with accuracy equal to one, but this is not always a good sign as usually means overfitting issues, likely due to the scarcity of data. In the next section we will see how data augmentation will affect the RF classification.

Following the example in [8] we also calculated the **relative feature importances** (FIs) in each of the ten classifications performed, determined according to how much they reduced the Gini index in the decision trees. This will give us an idea of how the measures are involved in the segregation of the data, i.e. how much they define the class separability in each condition. This method could be useful as a feature selection if other classifiers were used (e.g. support vector machines as in [8]).

In figure 3.11 the FIs in **density** classification are reported. In the presence of the CFs, the first three measures are the SC bursting electrode, the number of active electrodes in NBs and the OFR in single-channel (SC) activity. When we discarded the CFs the measure ranking slightly changed, with a higher importance for the length's measures (NB rising, falling and lengths). However, the SC OFR and the NB electrodes are still in the first places. Another interesting difference is that many measures in the case without CFs do not influence at all the classification, reporting almost a null value of FI. For example, the IPI cluster dropped from the sixth spot to zero FI.

The left side of figure 3.12 shows the FIs in **WIV dense** classification with CFs. All the measures show similar FIs score but the first three are the NB rate, the Pearson correlation (SW) and the mutual information of the Poincare plots. After the CFs were removed most of the FIs tend to be more concentrate in fewer measures and the ranking changed completely, at least for the first places. Now most of the importance is held by the NB peaks. However, the worst measures did not shift as the IBI and IPI clusters remained in the last positions.

In figure 3.13 the FIs derived from the **batch dense** classification is illustrated. Here the relative values did not undergo to a lot of derangement after the Cfs were taken out. In fact, the SC bursting electrodes and the NB ISI CV kept the higher level of FIs. Conversely, the features positioned in the last places show more changes because the NB IPI and IBI cluster from mid ranking positions became the worst features.

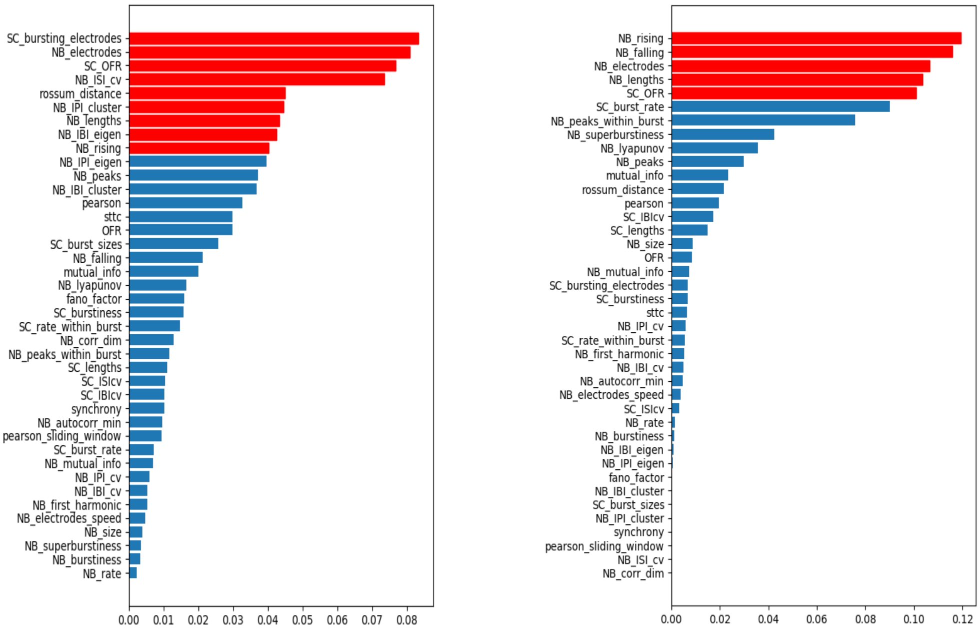

FIGURE 3.11: Relative feature importances (FI) in RF classification between dense and sparse cultures. The FIs were determined based on the amount they reduced the Gini index. The horizontal bars coloured by red indicate the features that count for the half of the importance. Left: FIs with CFs; Right: FIs without CFs.

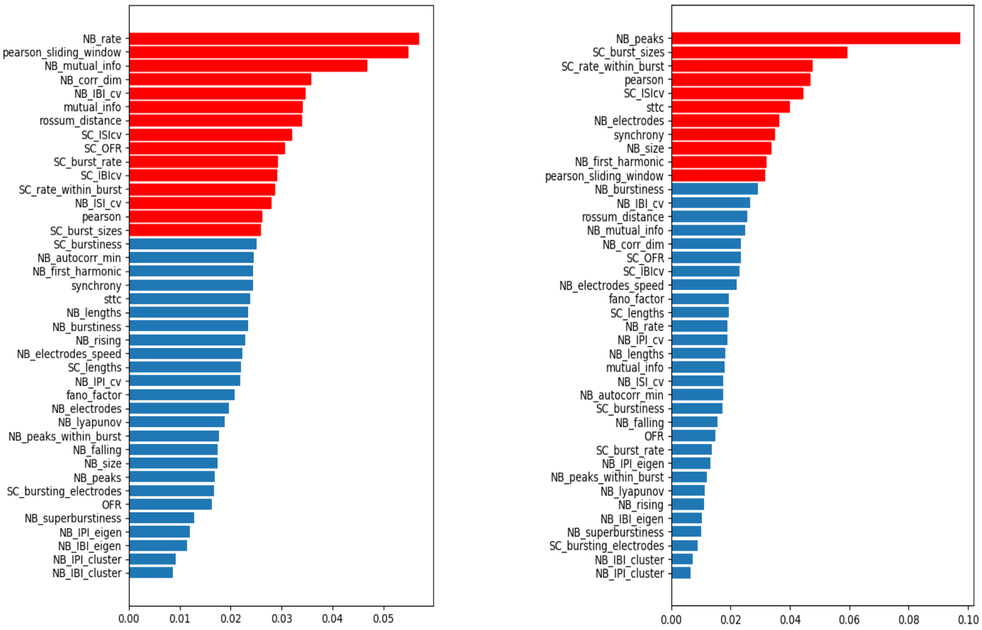

FIGURE 3.12: Relative feature importances (FI) in RF classification among different WIVs in dense cultures. The FIs were determined based on the amount they reduced the Gini index. The horizontal bars coloured by red indicate the features that count for the half of the importance. Left: FIs with CFs; Right: FIs without CFs.

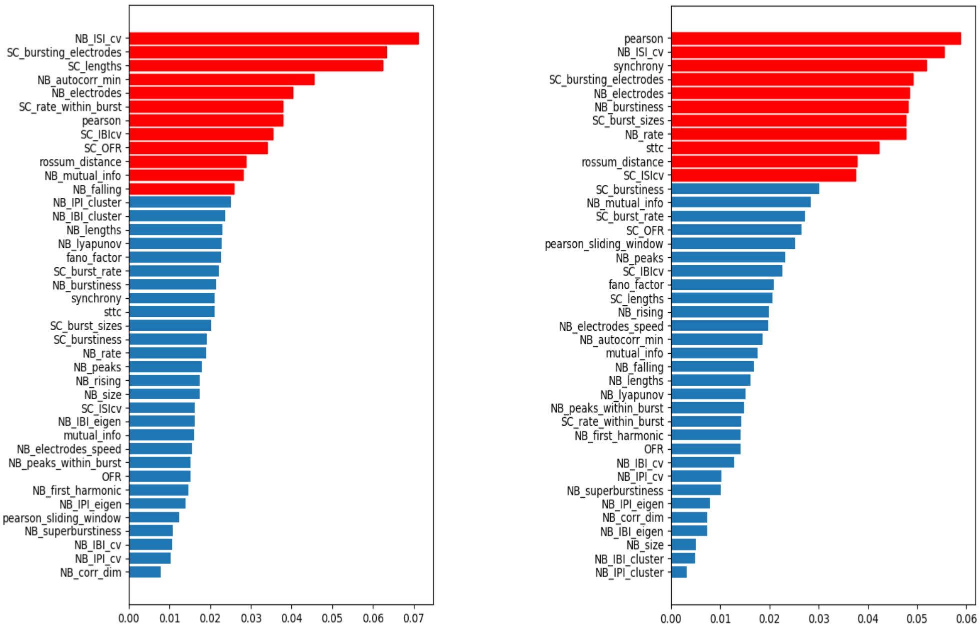

FIGURE 3.13: Relative feature importances (FI) in RF classification among different batches in dense cultures. The FIs were determined based on the amount they reduced the Gini index. The horizontal bars coloured by red indicate the features that count for the half of the importance. Left: FIs with CFs; Right: FIs without CFs.

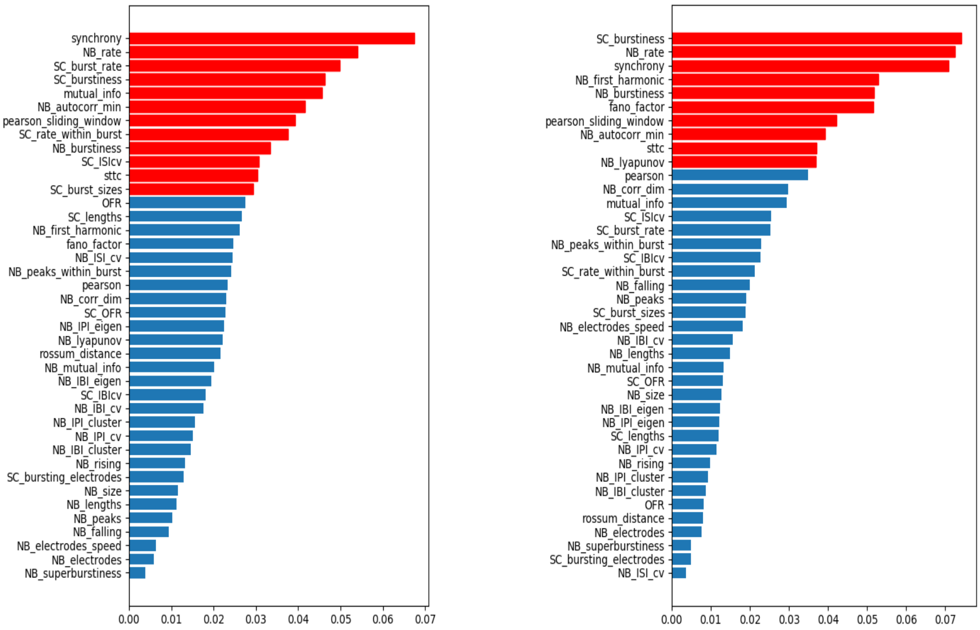

FIGURE 3.14: Relative feature importances (FI) in RF classification among different WIVs in sparse cultures. The FIs were determined based on the amount they reduced the Gini index. The horizontal bars coloured by red indicate the features that count for the half of the importance. Left: FIs with CFs; Right: FIs without CFs.

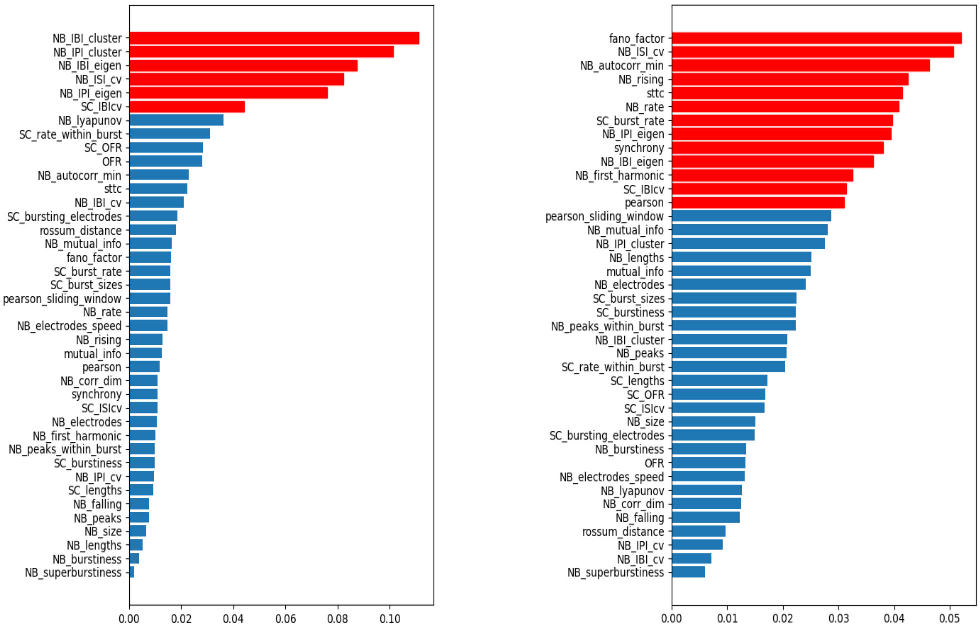

FIGURE 3.15: Relative feature importances (FI) in RF classification among different batches in sparse cultures. The FIs were determined based on the amount they reduced the Gini index. The horizontal bars coloured by red indicate the features that count for the half of the importance. Left: FIs with CFs; Right: FIs without CFs.

The next plots (figure 3.14) shows the FIs of the **WIV sparse** classification. Also in this case the changes after the exclusion of the CFs are not that relevant, at least for the measures with higher level of FI. As a matter of fact, the synchrony, the NB rate and the SC burstiness keep being important, also with some score gaining with respect to the other measures. Just the SC burst rate dropped from the second position to the 15^{th} ranking spot. As far as it is concerned the measures with the worst FIs, it is worthy to notice how the NB ISI CV shifted from a mid position to the last place.

Finally, we described the case of the **batch sparse** classification (figure 3.15). In this case, removing the CFs brought to a drastic alteration of the ranking. When the CFs were taken into account most of the FIs were due to the first measures, namely, the IBI- and IPI-related measures. After reducing the CFs, the FIs were more distributed over more measures and the first places were occupied by the Fano factor and the NB ISI CV (that was important also before) and the IPI and IBI CV dropped to the last ranking spots. Conversely, the superburstiness stayed in both cases with the worst FI score.

In general, we can state that there is not any specific measure or a class of measure (NB, SC or correlations) that is more important in classification purpose because it strongly depends on which type of class we wanted to individuate ad if we considered the CFs. Although, sometimes some features seemed to be more robust when underwent to the reduction of the CFs. This is a different result that the conclusions reported in [8] where the IBI CV and the ISI CV were found to be the more important features. However, in that study they classified just the first DIVs and they obtained the recordings from another type of MEA. We will come back on the overall FI in the last section, after we will test the subsampling effects.

In addition, we could not find a small group of measures detaining the majority of the FI in almost all the classification because the FI differences among the measures were usually tiny, meaning that, in order to achieve a good accuracy, the classifier needed many measures and not just a bunch of them. In figures 3.11-15 the red bars show the measures contributing for half of the total FI. The number of this measures ranges from 5 (in density classification with no CFs) to 15 (WIV classification in dense cultures with CFs) so, in general, there is no preference into few features.

Moreover, we could notice a general trend: the number of features holding the 50% of the importance decreased when the CFs were reduced. The only exception is reported in the batch sparse classification, an odd behaviour in agreement with the drop of the accuracy illustrated in table 3.4.

In conclusion, one has to pick quite many measures (both in quantity and variety) when dealing with this kind of data as for example in drug screening or to classify healthy and pathological neural networks in order to achieve good classification performances and get meaningful results.

3.2.2 Subsampling Effects

This section shows the results of the Random Forest classification under the effect of subsampling, both temporal and spatial. As far as it is concerned the **temporal subsampling**, we split the recordings in equal parts mainly for data augmentation purpose. In fact, when we reduced the CFs the remained samples were not enough to ensure a good classification performance without risking to meet overfitting drawbacks. Since the recordings are quite long (around 30 minutes) we checked how the accuracy changed by splitting the recordings by one half, one third and one quarter, in order to double, triplicate and quadruplicate the number of samples, respectively. In other words, we calculated again each measure for every piece of the shorter recording obtained from partitioning in equal length the 30-minutes-long spiking time-series. In this way it was possible to check if reducing the recording length we still included enough spikes and bursts for extracting meaningful measures that were used to get a more faithful classification accuracy, bypassing overfitting issue due to lack of data.

Furthermore, we studied the effects of classification performance after reducing the number of electrodes, checking in this way the robustness of the measures under **spatial subsampling**. We sequentially took out from the recordings the spikes coming from 10, 20, 30, 40 and 50 channels, which were picked up randomly. Rather than run the recording again using different devices or switching off part of the electrodes, we simulated the subsampled recording by randomly removing all data coming from a given number of electrodes, computing again all the measures, and then repeating the RF classification to see how well the classes could be discriminated in subsampled conditions. Studying the spatial subsampling effect in this kind of data is fundamental because recording spiking activity from a neural network *in vitro* or in a living brain with the current technology, only a very small fraction of all neurons can be actually accessed. Hence, to infer global properties, it is necessary to extrapolate from this small sampled fraction to the full system. Then we tested the validity of the measures against this issue by further subsampling the already subsampled recordings. As far as it is concerned the MEA device, it can evaluate recordings from 59 multi-units. This is only a small fraction of the entire cultured neural network, which comprised around 50,000 neurons. To investigate this phenomenon, we computed each measure applying a further subsampling, that is, evaluating a subset of the recorded units, following the analysis on the spatial subsampling reported in [25] where the authors used the same neural network *in vitro* dataset. However, in that study the authors used experimental data to test the validity of their novel analytical approach of the effect of spatial subsampling on the distributions of the neural avalanches, a phenomenon that we did not take into account, though strongly related to the NB pattern.

The plots in figure 3.16 illustrate how the **classification accuracy** is affected by the temporal and spatial subsampling, that is, by shortening the recording time and removing the electrodes, respectively. In order to quantitatively determine accuracy differences between each of the subsampled classification and the normal result, we performed t-test statistic. In figure 3.16 we changed the point marker into a cross if the p-value was below the level of confidence (set at 0.05), divided by the number of comparisons (Bonferroni correction), that are three and five for the temporal and spatial subsampling, respectively.

The first two plots report the accuracy in **density** classification. As expected, when affected by temporal subsampling the accuracy steadily increased, at least in the case with CFs, even if the changes are not statistically significant. In the classification with reduced CFs the accuracy is almost always the maximum possible, with an out-of-trend behaviour when the recordings were split by half. It would be interesting to test the accuracy while further splitting the recordings to check if the case with CFs will reach similar values of the case of reduced CFs, or at some point the accuracy will start to decrease because the recordings become too short for extracting measures (e.g. shorter than a typical NB duration). We did not perform this analysis because of computational time issue. A similar steady trend is reported in the spatial subsampling case, where the classification accuracies considering CFs do not show significant changes if electrodes were removed. Unexpectedly, also the case with reduced CFs was not affected by the spacial subsampling, being the accuracy around 1 in each subsampled condition. All in all, in density classifications we could not observe significant differences maybe because sparse and dense cultures are conditions that can be easily distinguished, as it was already visible in the exploratory statistic analysis.

In the second row of plots of figure 3.16 the **WIV dense** classification accuracies are shown. Starting from the temporal condition with reduced CFs, although the accuracy passed from 0.80 to 0.85, we did not notice a significant increment when splitting the recordings. However, when the CFs were considered, the accuracy significantly increased from 0.74 to 0.85, reaching the same performance of the classification of samples without CFs. As we already said, classifying the WIVs in normal condition was a little tricky because the cultures show high day-by-day variability, at least in the range of time we considered, as the cultures were under the influence of the fast initial development. In fact, in this case the accuracy shown the worst performance but we could not stratify more the dataset because the number of samples was too low for the number of features we were testing. As we obtained more samples after performing data augmentation, it could be interesting to see how the performance would change if shrinking the DIVs interval up to the ideal case of comparison between two single DIVs. However, for this purpose probably the recordings have to be split even more. Looking at the plot showing the spatial subsampling effect, no relevant alteration can be noticed, as the accuracies are constant in both the two different CFs cases, although in the last point (10 electrodes) the accuracy for the reduced CFs seems to decrease approaching the value of the full CFs case, around 0.70.

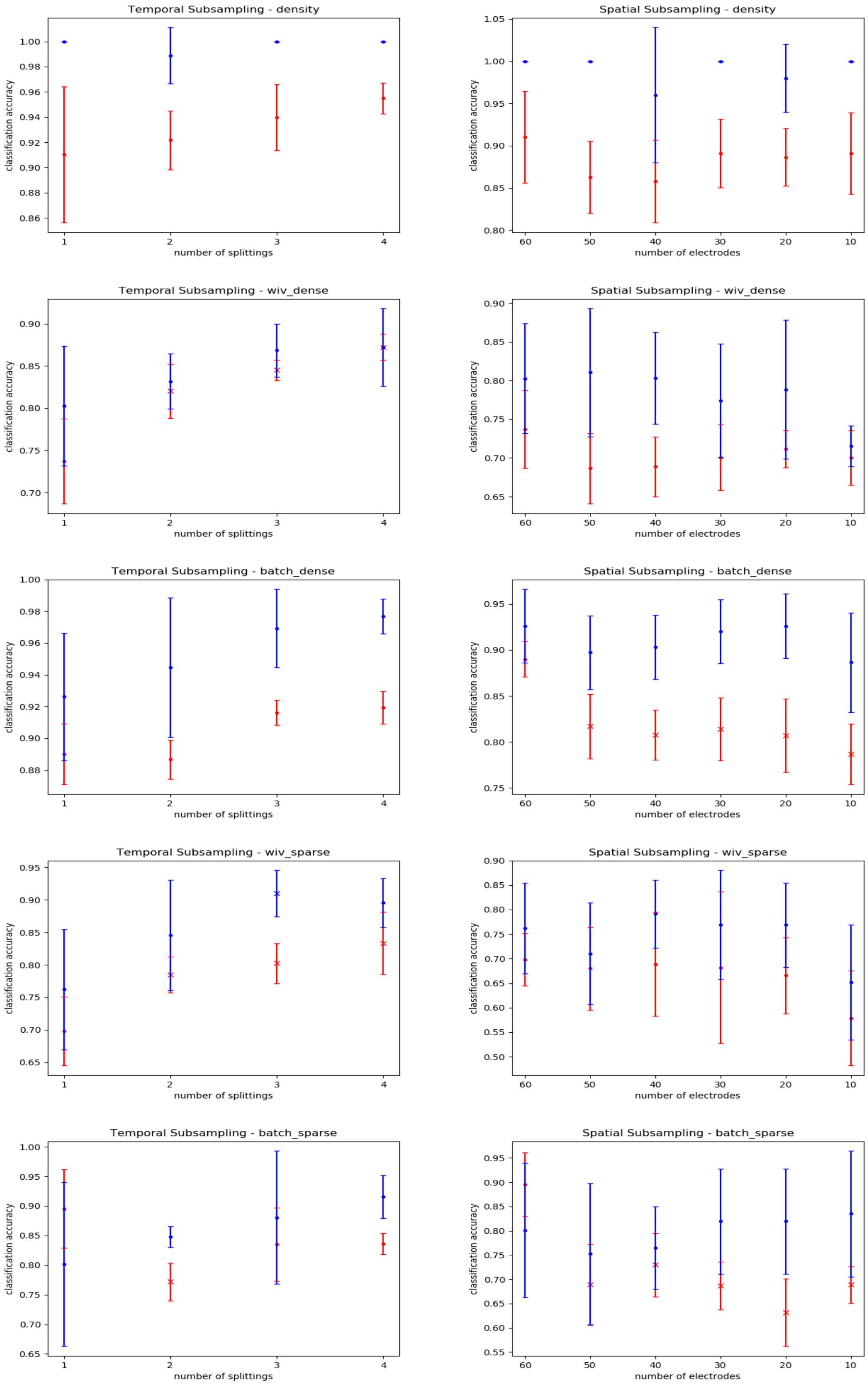

FIGURE 3.16: The accuracy trends of RF classifications using subsampled measures, both temporally (left column) and spatially (right column). All ten classifications are shown, i.e., density, WIV dense, batch dense, WIV sparse and batch sparse for the sample choice with CFs (red) and without CFs (blue). As a 5-fold cross validation was used for splitting training and test set, the standard deviation of the accuracy is also reported. If the accuracy is significantly different with respect to the not subsampled case, the dot is replaced by a cross.

As far as it is concerned the **batch dense** classification, when we split the recordings the accuracy slightly raised, from 0.89 to 0.92 in the case with CFs and from 0.93 to 0.98 in the condition with reduced CFs. However, after performing the t-test it came out that these changes are not significant. Considering the trend maybe we would find significant increment if we would further partition the recordings unless the measures will be affected by the temporal subsampling. On the other hand, the classification performance affected by spatial subsampling shown significant decreasing, for each subsampled condition, at least when considering full CFs, as the accuracy drop from almost 0.89 to values around 0.80. The case with reduced CFs did not show significant changes, as the accuracies oscillate in the range 0.92-0.89, thus, showing more robustness with respect to the case including full CFs.

Next, let us describe the plot reporting the classifications involving the sparse samples. The **WIV sparse** classifications affected by temporal subsampling clearly reported an accuracy improvement due to data augmentation effect. In the case with full CFs all the subsampled accuracy shown a significant increment, up to 0.83, when the recordings are split in four equal parts. In the case with reduced CFs, only when the number of splitting is three, it was possible to notice a significant difference with the non-subsampled condition, even if a general improvement is visible since all the accuracies are above 0.85 while the non-subsampled counterpart is 0.76. In the spatial subsampling the accuracies did not show significant differences. Just in the last case, when only ten electrodes were considered in the measure extraction, the accuracy shows a little drop to 0.58 and 0.65 for the CFs and reduced CFs case, respectively. Conversely, the other accuracies range in the interval 0.65-0.70 in the former case and 0.70-0.80 in the latter case.

Lastly, the **batch sparse** classification in the normal condition without subsampling reported an odd behaviour because the case with reduced CFs has a lower accuracy than the case with full CF. We speculated that this strange outcomes could be due to overfitting. Indeed, when performing data augmentation the normal trend was restored. The subsampled accuracies have a slightly increasing trend reaching a value of 0.84 and 0.92 for the case with CFs and with reduced CFs, respectively. However, also in the case of the spatial subsampling the accuracies switched position, so probably the odd high-accuracy classification level reached with the CFs is due to other external factors. If this accuracy value is discarded, in the last plot the accuracies did not seem to be strongly affected by the spatial subsamplig as they oscillate between 0.65 and 0.75 (CFs) or 0.75 and 0.85 (reduced CFs) since the significant differences reported in the plot by a cross are due to the outlier first value.

Summing up, we show the overall patterns came out after studying the accuracy trends under the effect of subsampling. We can state that, as expected, the classification performance benefits from the splitting of the recordings in multiple parts, in particular, when including CFs in the samples selection. This improvement was more prominent in the WIVs classification in which, due to the high variability during development and the lack of data, the accuracy shown the worst scores. As far as it is concerned the spatial subsampling, removing the electrodes did not have a strong effect on the classification performance since the accuracy did not report significant changing, except for the extreme case of recordings extracted only from ten electrodes where in some conditions the accuracy shown a significant decline.

Nevertheless, to obtain more meaningful insights from this analysis is important to look at the role of single feature in different subsampled conditions. Below, we will discuss about the **feature ranking** determined by their importance in classification, focusing on the changes due to the subsampling. In particular, we will describe the features that count for the half of the importance (reported in the red cells in the tables below) and with the worst scores. Also, we will stress out the alteration between the two CFs conditions, a discussion already started in the previous section. Moreover, for the sake of clarity, we just reported the feature names without the actual FI value. This choice was also determined by the fact that the FI value is relative to one particular classification so it would not be meaningful compare directly the FI belonging to different subsampled classification. Thus, we will analyse their relative ranking order and the number of features holding half of the importance, a threshold arbitrarily chosen for facilitating the comparisons.

In figure 3.17 the case of **density** classifications is illustrated. The upper table reports the feature rankings in the case with CFs. Let us start from the temporal subsampling. In the first three place we can notice the SC OFR, the MC OFR and the number of active electrode in NB, and below, but still in the red area, the bursting electrode (previously in the first place), van Rossum distance and STTC. It is also interesting to check the last places that are occupied by the number of cluster and eigenvalues ratio of IBI and IPI which in normal condition were placed in the first half of the ranking. Moreover, the NB ISI CV is drop out from the red area. However, apart this changes, the ranking seems to be quite robust under temporal subsampling. Similar behavior can be seen in the spatial subsampling case, although here the features counting for half of the importance is reduced when the number of removed electrodes increases. When considering reduced CFs, the number of features in the red area is constant in all the subsampled condition. The features occupying the first places are similar to the previous case, e.g. OFR, SC OFR and number of active electrodes. However, here it seems to be important also the duration of the NB (NB length, NB rising, NB falling). Interestingly, in the last column, when only 10 electrodes are considered, the Lyapunov exponent and the van Rossum distance are robust. As far as it is concerned the worst positions, also here the IBI/IPI related measures did not much contribute in the RF classification. Also other features show low scores, as NB rate, NB mutual info for the temporal subsampling and NB ISI CV, superburstiness, NB correlation dimension and SC bursts size for the spatial subsampling.

In figure 3.18 the feature rankings obtained from the **WIV dense** classification are illustrated. In the case with full CFs almost half of the measures lie in the red area. As we already said, due to high variability within cultures with few DIVs of difference, classify different WIVs is a non-trivial task. Thus, the classifier needed as many features as possible. In all the cases, the most important measure is the NB rate that is always placed in the top of the ranking. Then, also the NB mutual information was always well ranked, together with van Rossum distance, Pearson (siding window), and NB correlation dimension in the spatial subsampling classifications. Some features that were important for the density classification keep being in the red area also in this case, as the OFR, both SC and MC. Analogously, the IBI and IPI related measures, in particular the number of cluster and the eigenvalue ratio, were found in the lower part of the ranking, together with the superburstiness, the number of peak within a NB, and, in the case of spatial subsampling, the number of bursting electrodes, that in the density classification occupied higher positions. A similar trend for the worst scored features is also found in the case with reduced CFs. Conversely, the top-ranked features are different in this case. Now, the most important features are the NB peaks, SC burst size, NB ISI CV, SC rate within burst and the NB burstiness, where the latter gained importance at the most spatially subsampled conditions. Though in the temporally subsampled case OFR and SC OFR are in the red area, in the spatially subsampled ranking they lost importance.

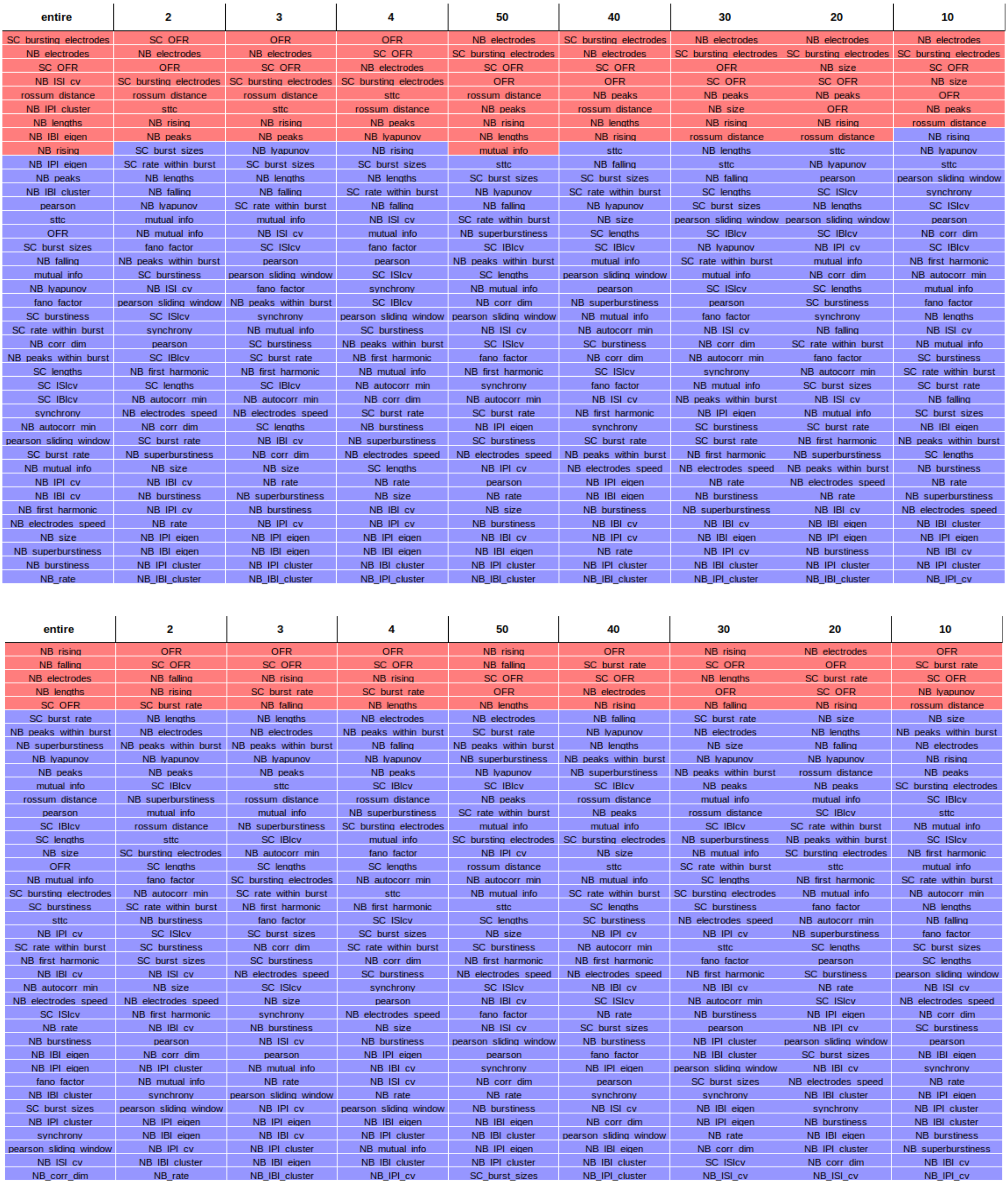

entire	2	3	4	50	40	30	20	10
SC bursting electrodes	SC OFR	OFR	OFR	NB electrodes	SC bursting electrodes	NB electrodes	NB electrodes	NB electrodes
NB electrodes	NB electrodes	NB electrodes	SC OFR	SC bursting electrodes	NB electrodes	SC bursting electrodes	SC bursting electrodes	SC bursting electrodes
SC OFR	OFR	SC OFR	NB electrodes	SC OFR	SC OFR	OFR	NB size	SC OFR
NB ISI cv	SC bursting electrodes	SC bursting electrodes	SC bursting electrodes	OFR	OFR	SC OFR	SC OFR	NB size
rossum distance	rossum distance	rossum distance	sttc	rossum distance	NB peaks	NB peaks	NB peaks	OFR
NB IPI cluster	sttc	sttc	rossum distance	NB peaks	rossum distance	NB size	OFR	NB peaks
NB lengths	NB rising	NB rising	NB peaks	NB rising	NB lengths	NB rising	NB rising	rossum distance
NB IBI eigen	NB peaks	NB peaks	NB lyapunov	NB lengths	NB rising	rossum distance	rossum distance	NB rising
NB rising	SC burst sizes	NB lyapunov	NB rising	mutual info	sttc	NB lengths	sttc	NB lyapunov
NB IPI eigen	SC rate within burst	SC burst sizes	SC burst sizes	sttc	NB falling	sttc	NB lyapunov	sttc
NB peaks	NB lengths	NB lengths	NB lengths	SC burst sizes	SC burst sizes	NB falling	pearson	pearson sliding window
NB IBI cluster	NB falling	NB falling	SC rate within burst	NB lyapunov	SC rate within burst	SC lengths	SC ISIcv	synchrony
pearson	NB lyapunov	SC rate within burst	NB falling	NB falling	NB lyapunov	SC burst sizes	NB lengths	SC ISIcv
sttc	mutual info	mutual info	NB ISI cv	SC rate within burst	NB size	pearson sliding window	pearson sliding window	pearson
OFR	NB mutual info	NB ISI cv	mutual info	NB superburstiness	SC lengths	SC IBIcv	SC IBIcv	NB corr dim
SC burst sizes	fano factor	SC ISIcv	fano factor	SC IBIcv	SC IBIcv	NB lyapunov	NB IPI cv	SC IBIcv
NB falling	NB peaks within burst	pearson	pearson	NB peaks within burst	mutual info	SC rate within burst	mutual info	NB first harmonic
mutual info	SC burstiness	pearson sliding window	SC ISIcv	SC lengths	pearson sliding window	mutual info	NB corr dim	NB autocorr min
NB lyapunov	NB ISI cv	fano factor	synchrony	NB mutual info	pearson	SC ISIcv	SC lengths	mutual info
fano factor	pearson sliding window	NB peaks within burst	SC IBIcv	NB corr dim	NB superburstiness	pearson	SC burstiness	fano factor
SC burstiness	SC ISIcv	synchrony	pearson sliding window	pearson sliding window	NB mutual info	fano factor	synchrony	NB lengths
SC rate within burst	synchrony	NB mutual info	SC burstiness	NB ISI cv	NB autocorr min	NB ISI cv	NB falling	NB ISI cv
NB corr dim	pearson	SC burstiness	NB peaks within burst	SC ISIcv	SC burstiness	NB corr dim	SC rate within burst	NB mutual info
NB peaks within burst	SC IBIcv	SC burst rate	NB first harmonic	fano factor	NB corr dim	NB autocorr min	fano factor	SC burstiness
SC lengths	NB first harmonic	NB first harmonic	NB mutual info	NB first harmonic	SC ISIcv	synchrony	NB autocorr min	SC rate within burst
SC ISIcv	SC lengths	SC IBIcv	NB autocorr min	synchrony	fano factor	NB mutual info	SC burst sizes	SC burst rate
SC IBIcv	NB autocorr min	NB autocorr min	NB corr dim	NB autocorr min	NB ISI cv	NB peaks within burst	NB ISI cv	NB falling
synchrony	NB electrodes speed	NB electrodes speed	SC burst rate	SC burst rate	NB first harmonic	NB IPI eigen	NB mutual info	SC burst sizes
NB autocorr min	NB corr dim	SC lengths	NB burstiness	NB IPI eigen	synchrony	SC burstiness	SC burst rate	NB IBI eigen
pearson sliding window	SC burst rate	NB IBI cv	NB superburstiness	SC burstiness	SC burst rate	SC burst rate	NB first harmonic	NB peaks within burst
SC burst rate	NB superburstiness	NB corr dim	NB electrodes speed	NB electrodes speed	NB peaks within burst	NB first harmonic	NB superburstiness	SC lengths
NB mutual info	NB size	NB size	SC lengths	NB IPI cv	NB electrodes speed	NB electrodes speed	NB peaks within burst	NB burstiness
NB IPI cv	NB IBI cv	NB rate	NB rate	pearson	NB IPI eigen	NB rate	NB electrodes speed	NB rate
NB IBI cv	NB burstiness	NB superburstiness	NB size	NB rate	NB IBI eigen	NB burstiness	NB rate	NB superburstiness
NB first harmonic	NB IPI cv	NB burstiness	NB IBI cv	NB size	NB burstiness	NB superburstiness	NB IBI cv	NB electrodes speed
NB electrodes speed	NB rate	NB IPI cv	NB IPI cv	NB burstiness	NB IBI cv	NB IBI cv	NB IBI eigen	NB IBI cluster
NB size	NB IPI eigen	NB IPI eigen	NB IPI eigen	NB IBI cv	NB IPI cv	NB IBI eigen	NB IPI eigen	NB IPI eigen
NB superburstiness	NB IBI eigen	NB IBI eigen	NB IBI eigen	NB IBI eigen	NB rate	NB IPI cv	NB burstiness	NB IBI cv
NB burstiness	NB IPI cluster	NB IPI cluster	NB IBI cluster	NB IPI cluster	NB IPI cluster	NB IBI cluster	NB IPI cluster	NB IPI cluster
NB_rate	NB_IBI_cluster	NB_IBI_cluster	NB_IPI_cluster	NB_IBI_cluster	NB_IBI_cluster	NB_IPI_cluster	NB_IBI_cluster	NB_IPI_cv

entire	2	3	4	50	40	30	20	10
NB rising	OFR	OFR	OFR	NB rising	OFR	NB rising	NB electrodes	OFR
NB falling	SC OFR	SC OFR	SC OFR	NB falling	SC burst rate	SC OFR	OFR	SC burst rate
NB electrodes	NB falling	NB rising	NB rising	SC OFR	SC OFR	NB lengths	SC burst rate	SC OFR
NB lengths	NB rising	SC burst rate	SC burst rate	OFR	NB electrodes	OFR	SC OFR	NB lyapunov
SC OFR	SC burst rate	NB falling	NB lengths	NB lengths	NB rising	NB falling	NB rising	rossum distance
SC burst rate	NB lengths	NB lengths	NB electrodes	NB electrodes	NB falling	SC burst rate	NB size	NB size
NB peaks within burst	NB electrodes	NB electrodes	NB peaks within burst	SC burst rate	NB lyapunov	NB electrodes	NB lengths	NB peaks within burst
NB superburstiness	NB peaks within burst	NB peaks within burst	NB falling	NB peaks within burst	NB lengths	NB size	NB falling	NB electrodes
NB lyapunov	NB lyapunov	NB lyapunov	NB lyapunov	NB superburstiness	NB peaks within burst	NB lyapunov	NB lyapunov	NB rising
NB peaks	NB peaks	NB peaks	NB peaks	NB lyapunov	NB superburstiness	NB peaks within burst	rossum distance	NB peaks
mutual info	SC IBIcv	sttc	SC IBIcv	SC IBIcv	SC IBIcv	NB peaks	NB peaks	SC bursting electrodes
rossum distance	NB superburstiness	rossum distance	rossum distance	NB peaks	rossum distance	mutual info	mutual info	SC IBIcv
pearson	mutual info	mutual info	NB superburstiness	SC rate within burst	NB peaks	rossum distance	SC IBIcv	sttc
SC IBIcv	rossum distance	NB superburstiness	SC bursting electrodes	mutual info	mutual info	SC IBIcv	SC rate within burst	NB mutual info
SC lengths	sttc	SC IBIcv	mutual info	SC bursting electrodes	SC bursting electrodes	NB superburstiness	NB peaks within burst	SC ISIcv
NB size	SC bursting electrodes	NB autocorr min	fano factor	NB IPI cv	NB size	NB mutual info	SC bursting electrodes	NB first harmonic
OFR	SC lengths	SC lengths	SC lengths	rossum distance	sttc	SC rate within burst	sttc	mutual info
NB mutual info	fano factor	SC bursting electrodes	NB autocorr min	NB autocorr min	NB mutual info	SC lengths	NB first harmonic	SC rate within burst
SC bursting electrodes	NB autocorr min	SC rate within burst	sttc	NB mutual info	SC rate within burst	SC bursting electrodes	NB mutual info	NB autocorr min
SC burstiness	SC rate within burst	NB first harmonic	NB first harmonic	sttc	SC lengths	SC burstiness	fano factor	NB lengths
sttc	NB burstiness	fano factor	SC ISIcv	SC lengths	SC burstiness	NB electrodes speed	NB autocorr min	NB falling
NB IPI cv	SC ISIcv	SC burst sizes	SC burst sizes	NB size	NB IPI cv	NB IPI cv	NB superburstiness	fano factor
SC rate within burst	SC burstiness	NB corr dim	SC rate within burst	SC burstiness	NB autocorr min	sttc	SC lengths	SC burst sizes
NB first harmonic	SC burst sizes	SC burstiness	NB corr dim	NB first harmonic	NB first harmonic	fano factor	pearson	SC lengths
NB IBI cv	NB ISI cv	NB electrodes speed	SC burstiness	NB electrodes speed	NB electrodes speed	NB first harmonic	SC burstiness	pearson sliding window
NB autocorr min	NB size	SC ISIcv	synchrony	SC ISIcv	NB IBI cv	NB IBI cv	NB rate	NB ISI cv
NB electrodes speed	NB electrodes speed	NB size	pearson	NB IBI cv	SC ISIcv	NB autocorr min	SC ISIcv	NB electrodes speed
SC ISIcv	NB first harmonic	synchrony	NB electrodes speed	fano factor	NB rate	NB burstiness	NB IPI eigen	NB corr dim
NB rate	NB IBI cv	NB burstiness	NB size	NB ISI cv	SC burst sizes	pearson	NB IPI cv	SC burstiness
NB burstiness	pearson	NB ISI cv	NB burstiness	pearson sliding window	NB burstiness	NB IPI cluster	pearson sliding window	pearson
NB IBI eigen	NB corr dim	pearson	NB IPI eigen	pearson	fano factor	NB IBI cluster	SC burst sizes	NB IBI eigen
NB IPI eigen	NB IPI cluster	NB mutual info	NB IBI cv	synchrony	NB IPI eigen	pearson sliding window	NB IBI cv	synchrony
fano factor	NB mutual info	NB rate	NB ISI cv	NB corr dim	pearson	SC burst sizes	NB electrodes speed	NB rate
NB IBI cluster	synchrony	pearson sliding window	NB rate	NB rate	synchrony	synchrony	NB IBI cluster	NB IPI eigen
SC burst sizes	pearson sliding window	NB IPI cv	pearson sliding window	NB burstiness	NB ISI cv	NB IBI eigen	synchrony	NB IPI cluster
NB IPI cluster	NB IPI eigen	NB IPI eigen	NB IBI eigen	NB IBI eigen	NB corr dim	NB IPI eigen	NB burstiness	NB IBI cluster
synchrony	NB IBI eigen	NB IBI cv	NB IPI cluster	NB IBI cluster	pearson sliding window	NB rate	NB IBI eigen	NB burstiness
pearson sliding window	NB IPI cv	NB IPI cluster	NB mutual info	NB IPI eigen	NB IBI eigen	NB corr dim	NB IPI cluster	NB superburstiness
NB ISI cv	NB IBI cluster	NB IBI eigen	NB IBI cluster	NB IPI cluster	NB IBI cluster	SC ISIcv	NB corr dim	NB IBI cv
NB_corr_dim	NB_rate	NB_IBI_cluster	NB_IPI_cv	SC_burst_sizes	NB_IPI_cluster	NB_ISI_cv	NB_ISI_cv	NB_IPI_cv

FIGURE 3.17: Table illustrating the feature importance ranking in density RF classification with CF (upper plot) and with reduced CF (lower plot). Every subsampled condition is reported, both temporally (columns 2,3,4) and spatially (columns 50,40,30,20,10). For clarity, also the ranking without subsampling is shown in the first column. The red area represents the features that count for half of the importance in the classification.

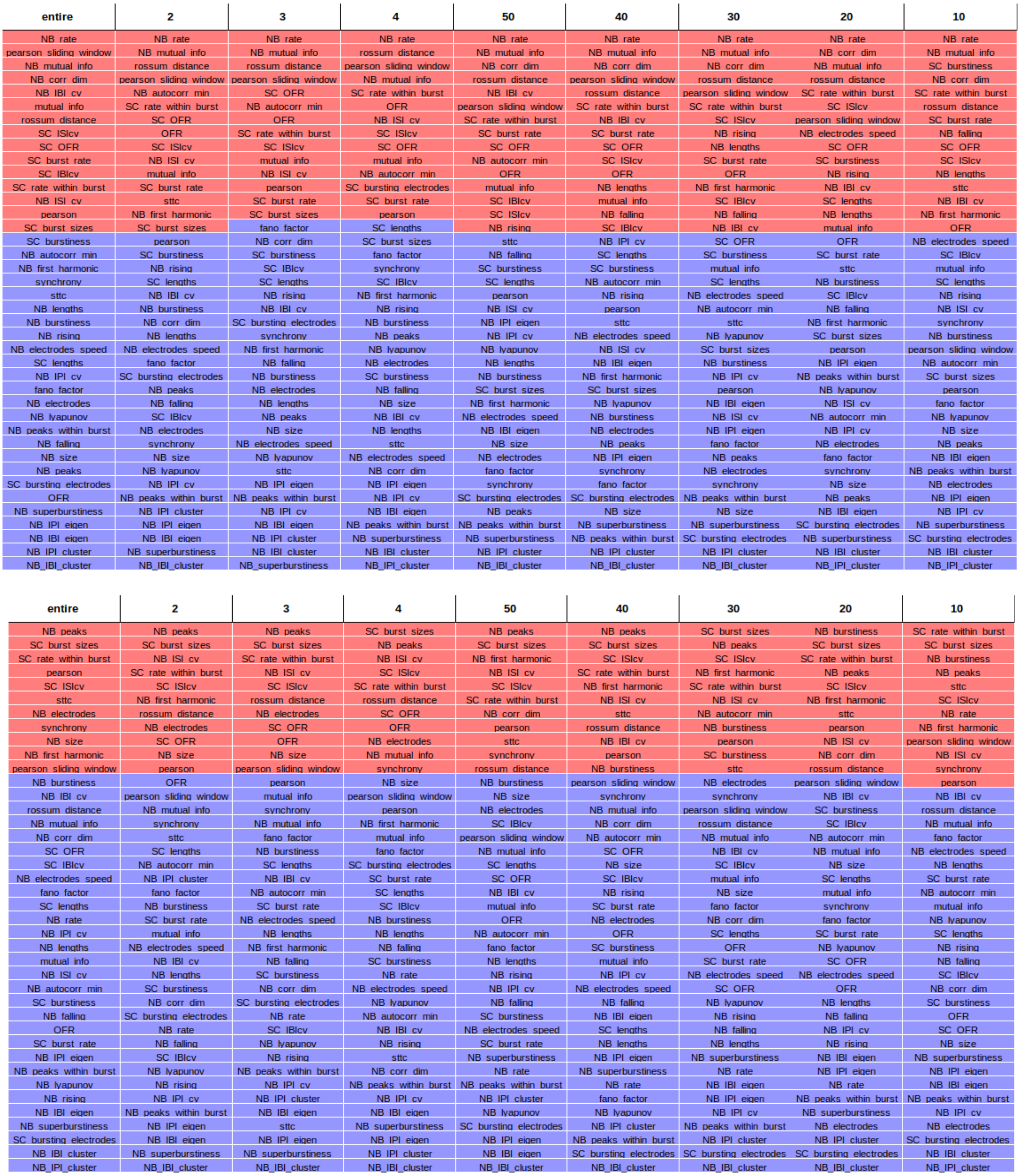

entire	2	3	4	50	40	30	20	10
NB rate	NB rate	NB rate	NB rate	NB rate	NB rate	NB rate	NB rate	NB rate
pearson sliding window	NB mutual info	NB mutual info	rossum distance	NB mutual info	NB mutual info	NB mutual info	NB corr dim	NB mutual info
NB mutual info	rossum distance	rossum distance	pearson sliding window	NB corr dim	NB corr dim	NB corr dim	NB mutual info	SC burstiness
NB corr dim	pearson sliding window	pearson sliding window	NB mutual info	rossum distance	pearson sliding window	rossum distance	rossum distance	NB corr dim
NB IBI cv	NB autocorr min	SC OFR	SC rate within burst	NB IBI cv	rossum distance	pearson sliding window	SC rate within burst	SC rate within burst
mutual info	SC rate within burst	NB autocorr min	OFR	pearson sliding window	SC rate within burst	SC rate within burst	SC ISIcv	rossum distance
rossum distance	SC OFR	OFR	NB ISI cv	SC rate within burst	NB IBI cv	SC ISIcv	pearson sliding window	SC burst rate
SC ISIcv	OFR	SC rate within burst	SC ISIcv	SC burst rate	SC burst rate	NB rising	NB electrodes speed	NB falling
SC OFR	SC ISIcv	SC ISIcv	SC OFR	SC OFR	SC OFR	NB lengths	SC OFR	SC OFR
SC burst rate	NB ISI cv	mutual info	mutual info	NB autocorr min	SC ISIcv	SC burst rate	SC burstiness	SC ISIcv
SC IBIcv	mutual info	NB ISI cv	NB autocorr min	OFR	OFR	OFR	NB rising	NB lengths
SC rate within burst	SC burst rate	pearson	SC bursting electrodes	mutual info	NB lengths	NB first harmonic	NB IBI cv	sttc
NB ISI cv	sttc	SC burst rate	SC burst rate	SC IBIcv	mutual info	SC IBIcv	SC lengths	NB IBI cv
pearson	NB first harmonic	SC burst sizes	pearson	SC ISIcv	NB falling	NB falling	NB lengths	NB first harmonic
SC burst sizes	SC burst sizes	fano factor	SC lengths	NB rising	SC IBIcv	NB IBI cv	mutual info	OFR
SC burstiness	pearson	NB corr dim	SC burst sizes	sttc	NB IPI cv	SC OFR	OFR	NB electrodes speed
NB autocorr min	SC burstiness	SC burstiness	fano factor	NB falling	SC lengths	SC burstiness	SC burst rate	SC IBIcv
NB first harmonic	NB rising	SC IBIcv	synchrony	SC burstiness	SC burstiness	mutual info	sttc	mutual info
synchrony	SC lengths	SC lengths	SC IBIcv	SC lengths	NB autocorr min	SC lengths	NB burstiness	SC lengths
sttc	NB IBI cv	NB rising	NB first harmonic	pearson	NB rising	NB electrodes speed	SC IBIcv	NB rising
NB lengths	NB burstiness	NB IBI cv	NB rising	NB ISI cv	pearson	NB autocorr min	NB falling	NB ISI cv
NB burstiness	NB corr dim	SC bursting electrodes	NB burstiness	NB IPI eigen	sttc	sttc	NB first harmonic	synchrony
NB rising	NB lengths	synchrony	NB peaks	NB IPI cv	NB electrodes speed	NB lyapunov	SC burst sizes	NB burstiness
NB electrodes speed	NB electrodes speed	NB first harmonic	NB lyapunov	NB lyapunov	NB ISI cv	SC burst sizes	pearson	pearson sliding window
SC lengths	fano factor	NB falling	NB electrodes	NB lengths	NB IBI eigen	NB burstiness	NB IPI eigen	NB autocorr min
NB IPI cv	SC bursting electrodes	NB burstiness	SC burstiness	NB burstiness	NB first harmonic	NB IPI cv	NB peaks within burst	SC burst sizes
fano factor	NB peaks	NB electrodes	NB falling	SC burst sizes	SC burst sizes	pearson	NB lyapunov	pearson
NB electrodes	NB falling	NB lengths	NB size	NB first harmonic	NB lyapunov	NB IBI eigen	NB ISI cv	fano factor
NB lyapunov	SC IBIcv	NB peaks	NB IBI cv	NB electrodes speed	NB burstiness	NB ISI cv	NB autocorr min	NB lyapunov
NB peaks within burst	NB electrodes	NB size	NB lengths	NB IBI eigen	NB electrodes	NB IPI eigen	NB IPI cv	NB size
NB falling	synchrony	NB electrodes speed	sttc	NB size	NB peaks	fano factor	NB electrodes	NB peaks
NB size	NB size	NB lyapunov	NB electrodes speed	NB electrodes	NB IPI eigen	NB peaks	fano factor	NB IBI eigen
NB peaks	NB lyapunov	sttc	NB corr dim	fano factor	synchrony	NB electrodes	synchrony	NB peaks within burst
SC bursting electrodes	NB IPI cv	NB IPI eigen	NB IPI eigen	synchrony	fano factor	synchrony	NB size	NB electrodes
OFR	NB peaks within burst	NB peaks within burst	NB IPI cv	SC bursting electrodes	SC bursting electrodes	NB peaks within burst	NB peaks	NB IPI eigen
NB superburstiness	NB IPI cluster	NB IPI cv	NB IBI eigen	NB peaks	NB size	NB size	NB IBI eigen	NB IPI cv
NB IPI eigen	NB IPI eigen	NB IBI eigen	NB peaks within burst	NB peaks within burst	NB superburstiness	NB superburstiness	SC bursting electrodes	NB superburstiness
NB IBI eigen	NB IBI eigen	NB IPI cluster	NB superburstiness	NB superburstiness	NB peaks within burst	SC bursting electrodes	NB superburstiness	SC bursting electrodes
NB IPI cluster	NB superburstiness	NB IBI cluster	NB IBI cluster	NB IPI cluster	NB IPI cluster	NB IPI cluster	NB IBI cluster	NB IBI cluster
NB_IBI_cluster	NB_IBI_cluster	NB_superburstiness	NB_IPI_cluster	NB_IBI_cluster	NB_IBI_cluster	NB_IBI_cluster	NB_IPI_cluster	NB_IPI_cluster

entire	2	3	4	50	40	30	20	10
NB peaks	NB peaks	NB peaks	SC burst sizes	NB peaks	NB peaks	SC burst sizes	NB burstiness	SC rate within burst
SC burst sizes	SC burst sizes	SC burst sizes	NB peaks	SC burst sizes	SC burst sizes	NB peaks	SC burst sizes	SC burst sizes
SC rate within burst	NB ISI cv	SC rate within burst	NB ISI cv	NB first harmonic	SC ISIcv	SC ISIcv	SC rate within burst	NB burstiness
pearson	SC rate within burst	NB ISI cv	SC ISIcv	NB ISI cv	SC rate within burst	NB first harmonic	NB peaks	NB peaks
SC ISIcv	SC ISIcv	SC ISIcv	SC rate within burst	SC ISIcv	NB first harmonic	SC rate within burst	SC ISIcv	sttc
sttc	NB first harmonic	rossum distance	rossum distance	SC rate within burst	NB ISI cv	NB ISI cv	NB first harmonic	SC ISIcv
NB electrodes	rossum distance	NB electrodes	SC OFR	NB corr dim	sttc	NB autocorr min	sttc	NB rate
synchrony	NB electrodes	SC OFR	OFR	pearson	rossum distance	NB burstiness	pearson	NB first harmonic
NB size	SC OFR	OFR	NB electrodes	sttc	NB IBI cv	pearson	NB ISI cv	pearson sliding window
NB first harmonic	NB size	NB size	NB mutual info	synchrony	pearson	SC burstiness	NB corr dim	NB ISI cv
pearson sliding window	pearson	pearson sliding window	synchrony	rossum distance	NB burstiness	sttc	rossum distance	synchrony
NB burstiness	OFR	pearson	NB size	NB burstiness	pearson sliding window	NB electrodes	pearson sliding window	pearson
NB IBI cv	pearson sliding window	mutual info	pearson sliding window	NB size	synchrony	synchrony	NB IBI cv	NB IBI cv
rossum distance	NB mutual info	synchrony	pearson	NB electrodes	NB mutual info	pearson sliding window	SC burstiness	rossum distance
NB mutual info	synchrony	NB mutual info	NB first harmonic	SC IBIcv	NB corr dim	rossum distance	SC IBIcv	NB mutual info
NB corr dim	sttc	fano factor	mutual info	pearson sliding window	NB autocorr min	NB mutual info	NB autocorr min	fano factor
SC OFR	SC lengths	NB burstiness	fano factor	NB mutual info	SC OFR	NB IBI cv	NB mutual info	NB electrodes speed
SC IBIcv	NB autocorr min	SC lengths	SC bursting electrodes	SC lengths	NB size	SC IBIcv	NB size	NB lengths
NB electrodes speed	NB IPI cluster	NB IBI cv	SC burst rate	SC OFR	SC IBIcv	mutual info	SC lengths	SC burst rate
fano factor	fano factor	NB autocorr min	SC lengths	NB IBI cv	NB rising	NB size	mutual info	NB autocorr min
SC lengths	NB burstiness	SC burst rate	SC IBIcv	mutual info	SC burst rate	fano factor	synchrony	mutual info
NB rate	SC burst rate	NB electrodes speed	NB burstiness	OFR	NB electrodes	NB corr dim	fano factor	NB lyapunov
NB IPI cv	mutual info	NB lengths	NB lengths	NB autocorr min	OFR	SC lengths	SC burst rate	SC lengths
NB lengths	NB electrodes speed	NB first harmonic	NB falling	fano factor	SC burstiness	OFR	NB lyapunov	NB rising
mutual info	NB IBI cv	NB falling	SC burstiness	NB lengths	mutual info	SC burst rate	SC OFR	NB falling
NB ISI cv	NB lengths	SC burstiness	NB rate	NB rising	NB IPI cv	NB electrodes speed	NB electrodes speed	SC IBIcv
NB autocorr min	SC burstiness	NB corr dim	NB electrodes speed	NB IPI cv	NB electrodes speed	SC OFR	OFR	NB corr dim
SC burstiness	NB corr dim	SC bursting electrodes	NB lyapunov	NB falling	NB falling	NB lyapunov	NB lengths	SC burstiness
NB falling	SC bursting electrodes	NB rate	NB autocorr min	SC burstiness	NB IBI eigen	NB rising	NB falling	OFR
OFR	NB rate	SC IBIcv	NB IBI cv	NB electrodes speed	SC lengths	NB falling	NB IPI cv	SC OFR
SC burst rate	NB falling	NB lyapunov	NB rising	SC burst rate	NB lengths	NB lengths	NB rising	NB size
NB IPI eigen	SC IBIcv	NB rising	sttc	NB superburstiness	NB IPI eigen	NB superburstiness	NB IBI eigen	NB superburstiness
NB peaks within burst	NB lyapunov	NB peaks within burst	NB corr dim	NB rate	NB superburstiness	NB rate	NB IPI eigen	NB IPI eigen
NB lyapunov	NB rising	NB IPI cv	NB peaks within burst	NB peaks within burst	NB rate	NB IBI eigen	NB rate	NB IBI eigen
NB rising	NB IPI cv	NB IPI cluster	NB IPI cv	NB IPI cluster	fano factor	NB IPI eigen	NB peaks within burst	NB peaks within burst
NB IBI eigen	NB peaks within burst	NB IBI eigen	NB IBI eigen	NB lyapunov	NB lyapunov	NB IPI cv	NB superburstiness	NB IPI cv
NB superburstiness	NB IPI eigen	sttc	NB superburstiness	SC bursting electrodes	NB IPI cluster	NB peaks within burst	NB electrodes	NB electrodes
SC bursting electrodes	NB IBI eigen	NB IPI eigen	NB IPI eigen	NB IPI eigen	NB peaks within burst	NB IPI cluster	NB IPI cluster	SC bursting electrodes
NB IBI cluster	NB superburstiness	NB superburstiness	NB IPI cluster	NB IBI eigen	SC bursting electrodes	SC bursting electrodes	SC bursting electrodes	NB IBI cluster
NB_IPI_cluster	NB_IBI_cluster	NB_IBI_cluster	NB_IBI_cluster	NB_IBI_cluster	NB_IBI_cluster	NB_IBI_cluster	NB_IBI_cluster	NB_IPI_cluster

FIGURE 3.18: Table illustrating the feature importance ranking in WIV dense RF classification with CF (upper plot) and with reduced CF (lower plot). Every subsampled condition is reported, both temporally (columns 2,3,4) and spatially (columns 50,40,30,20,10). For clarity, also the ranking without subsampling is shown in the first column. The red area represents the features that count for half of the importance in the classification.

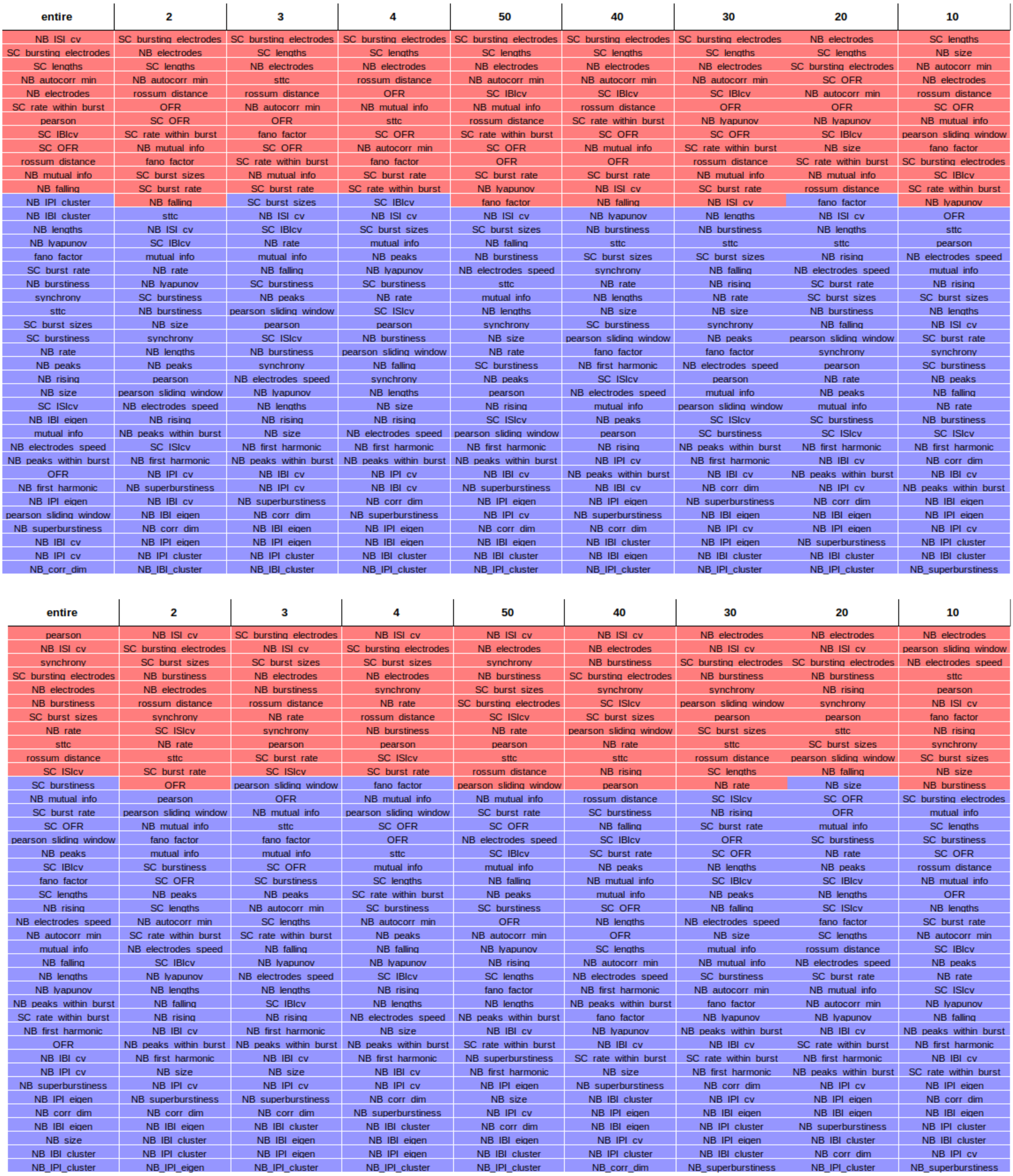

entire	2	3	4	50	40	30	20	10
NB ISI cv	SC bursting electrodes	SC bursting electrodes	SC bursting electrodes	SC bursting electrodes	SC bursting electrodes	SC bursting electrodes	NB electrodes	SC lengths
SC bursting electrodes	NB electrodes	SC lengths	SC lengths	SC lengths	SC lengths	SC lengths	SC lengths	NB size
SC lengths	SC lengths	NB electrodes	NB electrodes	NB electrodes	NB electrodes	NB electrodes	SC bursting electrodes	NB autocorr min
NB autocorr min	NB autocorr min	sttc	rossum distance	NB autocorr min	NB autocorr min	NB autocorr min	SC OFR	NB electrodes
NB electrodes	rossum distance	rossum distance	OFR	SC IBIcv	SC IBIcv	SC IBIcv	NB autocorr min	rossum distance
SC rate within burst	OFR	NB autocorr min	NB mutual info	NB mutual info	rossum distance	OFR	OFR	SC OFR
pearson	SC OFR	OFR	sttc	rossum distance	SC rate within burst	NB lyapunov	NB lyapunov	NB mutual info
SC IBIcv	SC rate within burst	fano factor	SC OFR	SC rate within burst	SC OFR	SC OFR	SC IBIcv	pearson sliding window
SC OFR	NB mutual info	SC OFR	NB autocorr min	SC OFR	NB mutual info	SC rate within burst	NB size	fano factor
rossum distance	fano factor	SC rate within burst	fano factor	OFR	OFR	rossum distance	SC rate within burst	SC bursting electrodes
NB mutual info	SC burst sizes	NB mutual info	SC burst rate	SC burst rate	SC burst rate	NB mutual info	NB mutual info	SC IBIcv
NB falling	SC burst rate	SC burst rate	SC rate within burst	NB lyapunov	NB ISI cv	SC burst rate	rossum distance	SC rate within burst
NB IPI cluster	NB falling	SC burst sizes	SC IBIcv	fano factor	NB falling	NB ISI cv	fano factor	NB lyapunov
NB IBI cluster	sttc	NB ISI cv	NB ISI cv	NB ISI cv	NB lyapunov	NB lengths	NB ISI cv	OFR
NB lengths	NB ISI cv	SC IBIcv	SC burst sizes	SC burst sizes	NB burstiness	NB burstiness	NB lengths	sttc
NB lyapunov	SC IBIcv	NB rate	mutual info	NB falling	sttc	sttc	sttc	pearson
fano factor	mutual info	mutual info	NB peaks	NB burstiness	SC burst sizes	SC burst sizes	NB rising	NB electrodes speed
SC burst rate	NB rate	NB falling	NB lyapunov	NB electrodes speed	synchrony	NB falling	NB electrodes speed	mutual info
NB burstiness	NB lyapunov	SC burstiness	SC burstiness	sttc	NB rate	NB rising	SC burst rate	NB rising
synchrony	SC burstiness	NB peaks	NB rate	mutual info	NB lengths	NB rate	SC burst sizes	SC burst sizes
sttc	NB burstiness	pearson sliding window	SC ISIcv	NB lengths	NB size	NB size	NB burstiness	NB lengths
SC burst sizes	NB size	pearson	pearson	synchrony	SC burstiness	synchrony	NB falling	NB ISI cv
SC burstiness	synchrony	SC ISIcv	NB burstiness	NB size	pearson sliding window	NB peaks	pearson sliding window	SC burst rate
NB rate	NB lengths	NB burstiness	pearson sliding window	NB rate	fano factor	fano factor	synchrony	synchrony
NB peaks	NB peaks	synchrony	NB falling	SC burstiness	NB first harmonic	NB electrodes speed	pearson	SC burstiness
NB rising	pearson	NB electrodes speed	synchrony	NB peaks	SC ISIcv	pearson	NB rate	NB peaks
NB size	pearson sliding window	NB lyapunov	NB lengths	pearson	NB electrodes speed	mutual info	NB peaks	NB falling
SC ISIcv	NB electrodes speed	NB lengths	NB size	NB rising	mutual info	pearson sliding window	mutual info	NB rate
NB IBI eigen	NB rising	NB rising	NB rising	SC ISIcv	NB peaks	SC ISIcv	SC burstiness	NB burstiness
mutual info	NB peaks within burst	NB size	NB electrodes speed	pearson sliding window	pearson	SC burstiness	SC ISIcv	SC ISIcv
NB electrodes speed	SC ISIcv	NB first harmonic	NB first harmonic	NB first harmonic	NB rising	NB peaks within burst	NB first harmonic	NB first harmonic
NB peaks within burst	NB first harmonic	NB peaks within burst	NB peaks within burst	NB peaks within burst	NB IPI cv	NB first harmonic	NB IBI cv	NB corr dim
OFR	NB IPI cv	NB IBI cv	NB IPI cv	NB IBI cv	NB peaks within burst	NB IBI cv	NB peaks within burst	NB IBI cv
NB first harmonic	NB superburstiness	NB IPI cv	NB IBI cv	NB superburstiness	NB IBI cv	NB corr dim	NB IPI cv	NB peaks within burst
NB IPI eigen	NB IBI cv	NB superburstiness	NB corr dim	NB IPI eigen	NB IPI eigen	NB superburstiness	NB corr dim	NB IBI eigen
pearson sliding window	NB IBI eigen	NB corr dim	NB superburstiness	NB IPI cv	NB superburstiness	NB IBI eigen	NB IBI eigen	NB IPI eigen
NB superburstiness	NB corr dim	NB IBI eigen	NB IPI eigen	NB corr dim	NB corr dim	NB IPI cv	NB IPI eigen	NB IPI cv
NB IBI cv	NB IPI eigen	NB IPI eigen	NB IBI eigen	NB IBI eigen	NB IBI cluster	NB IPI eigen	NB superburstiness	NB IPI cluster
NB IPI cv	NB IPI cluster	NB IPI cluster	NB IBI cluster	NB IBI cluster	NB IBI eigen	NB IBI cluster	NB IBI cluster	NB IBI cluster
NB_corr_dim	NB_IBI_cluster	NB_IBI_cluster	NB_IPI_cluster	NB_IPI_cluster	NB_IPI_cluster	NB_IPI_cluster	NB_IPI_cluster	NB_superburstiness

entire	2	3	4	50	40	30	20	10
pearson	NB ISI cv	SC bursting electrodes	NB ISI cv	NB ISI cv	NB ISI cv	NB electrodes	NB electrodes	NB electrodes
NB ISI cv	SC bursting electrodes	NB ISI cv	SC bursting electrodes	NB electrodes	NB electrodes	NB ISI cv	NB ISI cv	pearson sliding window
synchrony	SC burst sizes	SC burst sizes	SC burst sizes	synchrony	NB burstiness	SC bursting electrodes	SC bursting electrodes	NB electrodes speed
SC bursting electrodes	NB burstiness	NB electrodes	NB electrodes	NB burstiness	SC bursting electrodes	NB burstiness	NB burstiness	sttc
NB electrodes	NB electrodes	NB burstiness	synchrony	SC burst sizes	synchrony	synchrony	NB rising	pearson
NB burstiness	rossum distance	rossum distance	NB rate	SC bursting electrodes	SC ISIcv	pearson sliding window	synchrony	NB ISI cv
SC burst sizes	synchrony	NB rate	rossum distance	SC ISIcv	SC burst sizes	pearson	pearson	fano factor
NB rate	SC ISIcv	synchrony	NB burstiness	NB rate	pearson sliding window	SC burst sizes	sttc	NB rising
sttc	NB rate	pearson	pearson	pearson	NB rate	sttc	SC burst sizes	synchrony
rossum distance	sttc	SC burst rate	SC ISIcv	sttc	sttc	rossum distance	pearson sliding window	SC burst sizes
SC ISIcv	SC burst rate	SC ISIcv	SC burst rate	rossum distance	NB rising	SC lengths	NB falling	NB size
SC burstiness	OFR	pearson sliding window	fano factor	pearson sliding window	pearson	NB rate	NB size	NB burstiness
NB mutual info	pearson	OFR	NB mutual info	NB mutual info	rossum distance	SC ISIcv	SC OFR	SC bursting electrodes
SC burst rate	pearson sliding window	NB mutual info	pearson sliding window	SC burst rate	SC burstiness	NB rising	OFR	mutual info
SC OFR	NB mutual info	sttc	SC OFR	SC OFR	NB falling	SC burst rate	mutual info	SC lengths
pearson sliding window	fano factor	fano factor	OFR	NB electrodes speed	SC IBIcv	OFR	SC burstiness	SC burstiness
NB peaks	mutual info	mutual info	sttc	SC IBIcv	SC burst rate	SC OFR	NB rate	SC OFR
SC IBIcv	SC burstiness	SC OFR	mutual info	mutual info	NB peaks	NB lengths	NB peaks	rossum distance
fano factor	SC OFR	SC burstiness	SC lengths	NB falling	NB mutual info	SC IBIcv	SC IBIcv	NB mutual info
SC lengths	NB peaks	NB peaks	SC rate within burst	NB peaks	mutual info	NB peaks	NB lengths	OFR
NB rising	SC lengths	NB autocorr min	SC burstiness	SC burstiness	SC OFR	NB falling	SC ISIcv	NB lengths
NB electrodes speed	NB autocorr min	SC lengths	NB autocorr min	OFR	NB lengths	NB electrodes speed	fano factor	SC burst rate
NB autocorr min	SC rate within burst	SC rate within burst	NB peaks	NB autocorr min	OFR	NB size	SC lengths	NB autocorr min
mutual info	NB electrodes speed	NB falling	NB falling	NB lyapunov	SC lengths	mutual info	rossum distance	SC IBIcv
NB falling	SC IBIcv	NB lyapunov	NB lyapunov	NB rising	NB autocorr min	NB mutual info	NB electrodes speed	NB peaks
NB lengths	NB lyapunov	NB electrodes speed	SC IBIcv	SC lengths	NB electrodes speed	SC burstiness	SC burst rate	NB rate
NB lyapunov	NB lengths	NB lengths	NB rising	fano factor	NB first harmonic	NB autocorr min	NB mutual info	SC ISIcv
NB peaks within burst	NB falling	SC IBIcv	NB lengths	NB lengths	NB peaks within burst	fano factor	NB autocorr min	NB lyapunov
SC rate within burst	NB rising	NB rising	NB electrodes speed	NB peaks within burst	fano factor	NB lyapunov	NB lyapunov	NB falling
NB first harmonic	NB IBI cv	NB first harmonic	NB size	NB IBI cv	NB lyapunov	NB peaks within burst	NB IBI cv	NB peaks within burst
OFR	NB peaks within burst	NB peaks within burst	NB peaks within burst	SC rate within burst	NB IBI cv	NB IBI cv	SC rate within burst	NB first harmonic
NB IBI cv	NB first harmonic	NB IBI cv	NB first harmonic	NB superburstiness	SC rate within burst	SC rate within burst	NB first harmonic	NB IBI cv
NB IPI cv	NB size	NB size	NB IBI cv	NB first harmonic	NB size	NB first harmonic	NB peaks within burst	SC rate within burst
NB superburstiness	NB IPI cv	NB IPI cv	NB IPI cv	NB IPI eigen	NB superburstiness	NB corr dim	NB IPI cv	NB IPI eigen
NB IPI eigen	NB superburstiness	NB superburstiness	NB corr dim	NB size	NB IBI cluster	NB IPI cv	NB IPI eigen	NB corr dim
NB corr dim	NB corr dim	NB corr dim	NB superburstiness	NB IPI cv	NB IPI eigen	NB IBI eigen	NB IBI eigen	NB IBI eigen
NB IBI eigen	NB IBI eigen	NB IBI cluster	NB IBI cluster	NB corr dim	NB IBI eigen	NB IPI cluster	NB superburstiness	NB IPI cluster
NB size	NB IBI cluster	NB IBI eigen	NB IBI eigen	NB IBI eigen	NB IPI cv	NB IPI eigen	NB IBI cluster	NB IBI cluster
NB IBI cluster	NB IPI cluster	NB IPI eigen	NB IPI eigen	NB IBI cluster	NB IPI cluster	NB IBI cluster	NB corr dim	NB IPI cv
NB_IPI_cluster	NB_IPI_eigen	NB_IPI_cluster	NB_IPI_cluster	NB_IPI_cluster	NB_corr_dim	NB_superburstiness	NB_IPI_cluster	NB_superburstiness

FIGURE 3.19: Table illustrating the feature importance ranking in batch dense RF classification with CF (upper plot) and with reduced CF (lower plot). Every subsampled condition is reported, both temporally (columns 2,3,4) and spatially (columns 50,40,30,20,10). For clarity, also the ranking without subsampling is shown in the first column. The red area represents the features that count for half of the importance in the classification.

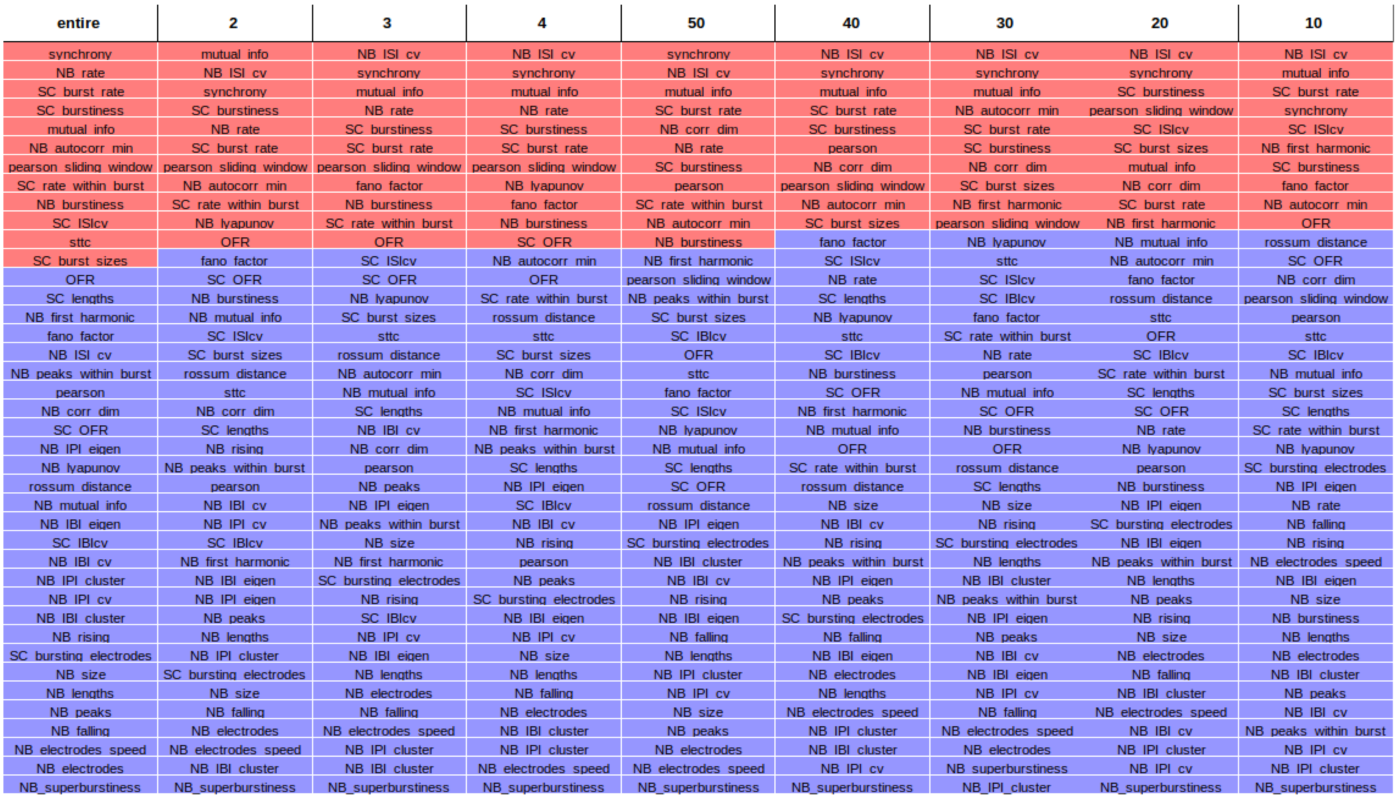

entire	2	3	4	50	40	30	20	10
synchrony	mutual info	NB ISI cv	NB ISI cv	synchrony	NB ISI cv	NB ISI cv	NB ISI cv	NB ISI cv
NB rate	NB ISI cv	synchrony	synchrony	NB ISI cv	synchrony	synchrony	synchrony	mutual info
SC burst rate	synchrony	mutual info	mutual info	mutual info	mutual info	mutual info	SC burstiness	SC burst rate
SC burstiness	SC burstiness	NB rate	NB rate	SC burst rate	SC burst rate	NB autocorr min	pearson sliding window	synchrony
mutual info	NB rate	SC burstiness	SC burstiness	NB corr dim	SC burstiness	SC burst rate	SC ISIcv	SC ISIcv
NB autocorr min	SC burst rate	SC burst rate	SC burst rate	NB rate	pearson	SC burstiness	SC burst sizes	NB first harmonic
pearson sliding window	pearson sliding window	pearson sliding window	pearson sliding window	SC burstiness	NB corr dim	NB corr dim	mutual info	SC burstiness
SC rate within burst	NB autocorr min	fano factor	NB lyapunov	pearson	pearson sliding window	SC burst sizes	NB corr dim	fano factor
NB burstiness	SC rate within burst	NB burstiness	fano factor	SC rate within burst	NB autocorr min	NB first harmonic	SC burst rate	NB autocorr min
SC ISIcv	NB lyapunov	SC rate within burst	NB burstiness	NB autocorr min	SC burst sizes	pearson sliding window	NB first harmonic	OFR
sttc	OFR	OFR	SC OFR	NB burstiness	fano factor	NB lyapunov	NB mutual info	rossum distance
SC burst sizes	fano factor	SC ISIcv	NB autocorr min	NB first harmonic	SC ISIcv	sttc	NB autocorr min	SC OFR
OFR	SC OFR	SC OFR	OFR	pearson sliding window	NB rate	SC ISIcv	fano factor	NB corr dim
SC lengths	NB burstiness	NB lyapunov	SC rate within burst	NB peaks within burst	SC lengths	SC IBIcv	rossum distance	pearson sliding window
NB first harmonic	NB mutual info	SC burst sizes	rossum distance	SC burst sizes	NB lyapunov	fano factor	sttc	pearson
fano factor	SC ISIcv	sttc	sttc	SC IBIcv	sttc	SC rate within burst	OFR	sttc
NB ISI cv	SC burst sizes	rossum distance	SC burst sizes	OFR	SC IBIcv	NB rate	SC IBIcv	SC IBIcv
NB peaks within burst	rossum distance	NB autocorr min	NB corr dim	sttc	NB burstiness	pearson	SC rate within burst	NB mutual info
pearson	sttc	NB mutual info	SC ISIcv	fano factor	SC OFR	NB mutual info	SC lengths	SC burst sizes
NB corr dim	NB corr dim	SC lengths	NB mutual info	SC ISIcv	NB first harmonic	SC OFR	SC OFR	SC lengths
SC OFR	SC lengths	NB IBI cv	NB first harmonic	NB lyapunov	NB mutual info	NB burstiness	NB rate	SC rate within burst
NB IPI eigen	NB rising	NB corr dim	NB peaks within burst	NB mutual info	OFR	OFR	NB lyapunov	NB lyapunov
NB lyapunov	NB peaks within burst	pearson	SC lengths	SC lengths	SC rate within burst	rossum distance	pearson	SC bursting electrodes
rossum distance	pearson	NB peaks	NB IPI eigen	SC OFR	rossum distance	SC lengths	NB burstiness	NB IPI eigen
NB mutual info	NB IBI cv	NB IPI eigen	SC IBIcv	rossum distance	NB size	NB size	NB IPI eigen	NB rate
NB IBI eigen	NB IPI cv	NB peaks within burst	NB IBI cv	NB IPI eigen	NB IBI cv	NB rising	SC bursting electrodes	NB falling
SC IBIcv	SC IBIcv	NB size	NB rising	SC bursting electrodes	NB rising	SC bursting electrodes	NB IBI eigen	NB rising
NB IBI cv	NB first harmonic	NB first harmonic	pearson	NB IBI cluster	NB peaks within burst	NB lengths	NB peaks within burst	NB electrodes speed
NB IPI cluster	NB IBI eigen	SC bursting electrodes	NB peaks	NB IBI cv	NB IPI eigen	NB IBI cluster	NB lengths	NB IBI eigen
NB IPI cv	NB IPI eigen	NB rising	SC bursting electrodes	NB rising	NB peaks	NB peaks within burst	NB peaks	NB size
NB IBI cluster	NB peaks	SC IBIcv	NB IBI eigen	NB IBI eigen	SC bursting electrodes	NB IPI eigen	NB rising	NB burstiness
NB rising	NB lengths	NB IPI cv	NB IPI cv	NB falling	NB falling	NB peaks	NB size	NB lengths
SC bursting electrodes	NB IPI cluster	NB IBI eigen	NB size	NB lengths	NB IBI eigen	NB IBI cv	NB electrodes	NB electrodes
NB size	SC bursting electrodes	NB lengths	NB lengths	NB IPI cluster	NB electrodes	NB IBI eigen	NB falling	NB IBI cluster
NB lengths	NB size	NB electrodes	NB falling	NB IPI cv	NB lengths	NB IPI cv	NB IBI cluster	NB peaks
NB peaks	NB falling	NB falling	NB electrodes	NB size	NB electrodes speed	NB falling	NB electrodes speed	NB IBI cv
NB falling	NB electrodes	NB electrodes speed	NB IBI cluster	NB peaks	NB IPI cluster	NB electrodes speed	NB IBI cv	NB peaks within burst
NB electrodes speed	NB electrodes speed	NB IPI cluster	NB IPI cluster	NB electrodes	NB IBI cluster	NB electrodes	NB IPI cluster	NB IPI cv
NB electrodes	NB IBI cluster	NB IBI cluster	NB electrodes speed	NB electrodes speed	NB IPI cv	NB superburstiness	NB IPI cv	NB IPI cluster
NB_superburstiness	NB_superburstiness	NB_superburstiness	NB_superburstiness	NB_superburstiness	NB_superburstiness	NB_IPI_cluster	NB_superburstiness	NB_superburstiness

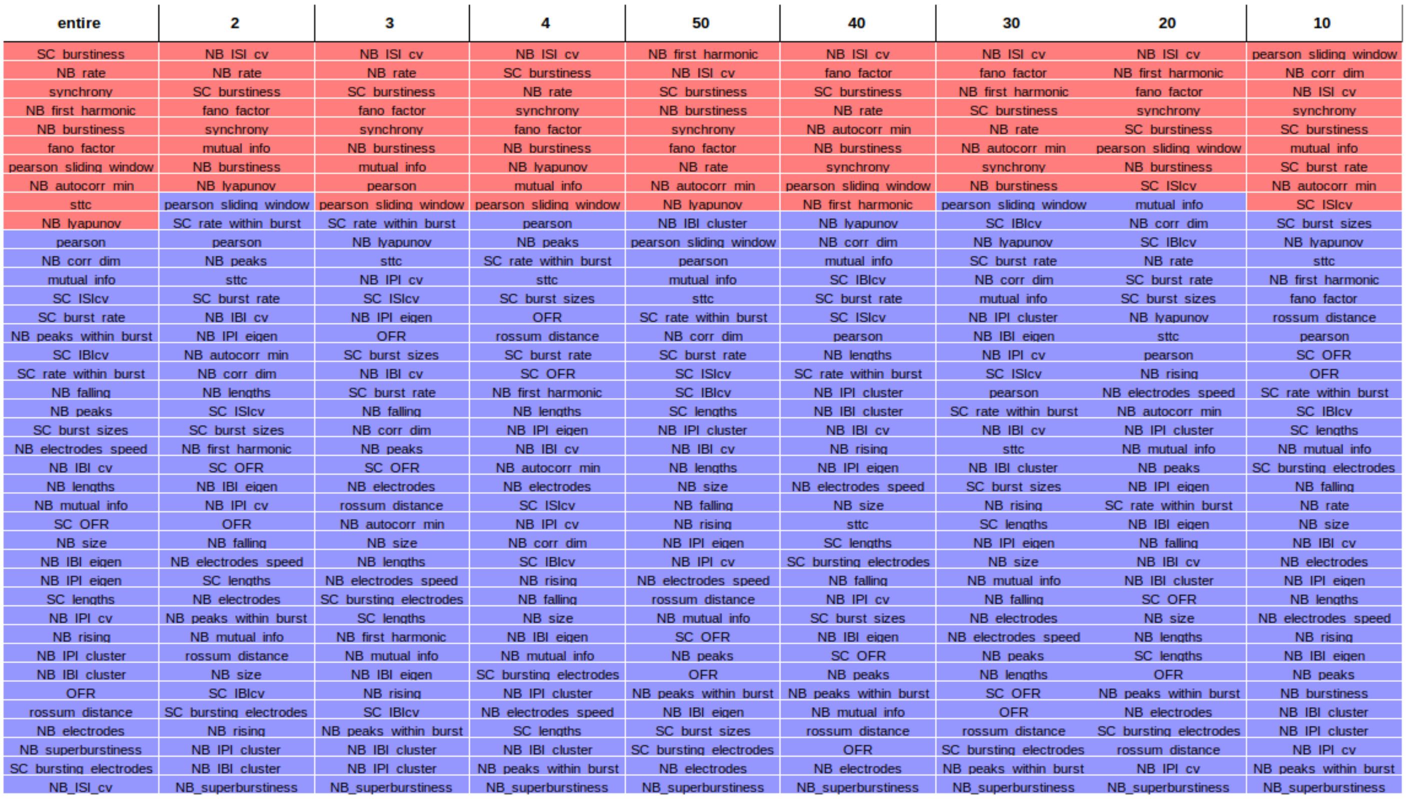

entire	2	3	4	50	40	30	20	10
SC burstiness	NB ISI cv	NB ISI cv	NB ISI cv	NB first harmonic	NB ISI cv	NB ISI cv	NB ISI cv	pearson sliding window
NB rate	NB rate	NB rate	SC burstiness	NB ISI cv	fano factor	fano factor	NB first harmonic	NB corr dim
synchrony	SC burstiness	SC burstiness	NB rate	SC burstiness	SC burstiness	NB first harmonic	fano factor	NB ISI cv
NB first harmonic	fano factor	fano factor	synchrony	NB burstiness	NB rate	SC burstiness	synchrony	synchrony
NB burstiness	synchrony	synchrony	fano factor	synchrony	NB autocorr min	NB rate	SC burstiness	SC burstiness
fano factor	mutual info	NB burstiness	NB burstiness	fano factor	NB burstiness	NB autocorr min	pearson sliding window	mutual info
pearson sliding window	NB burstiness	mutual info	NB lyapunov	NB rate	synchrony	synchrony	NB burstiness	SC burst rate
NB autocorr min	NB lyapunov	pearson	mutual info	NB autocorr min	pearson sliding window	NB burstiness	SC ISIcv	NB autocorr min
sttc	pearson sliding window	pearson sliding window	pearson sliding window	NB lyapunov	NB first harmonic	pearson sliding window	mutual info	SC ISIcv
NB lyapunov	SC rate within burst	SC rate within burst	pearson	NB IBI cluster	NB lyapunov	SC IBIcv	NB corr dim	SC burst sizes
pearson	pearson	NB lyapunov	NB peaks	pearson sliding window	NB corr dim	NB lyapunov	SC IBIcv	NB lyapunov
NB corr dim	NB peaks	sttc	SC rate within burst	pearson	mutual info	SC burst rate	NB rate	sttc
mutual info	sttc	NB IPI cv	sttc	mutual info	SC IBIcv	NB corr dim	SC burst rate	NB first harmonic
SC ISIcv	SC burst rate	SC ISIcv	SC burst sizes	sttc	SC burst rate	mutual info	SC burst sizes	fano factor
SC burst rate	NB IBI cv	NB IPI eigen	OFR	SC rate within burst	SC ISIcv	NB IPI cluster	NB lyapunov	rossum distance
NB peaks within burst	NB IPI eigen	OFR	rossum distance	NB corr dim	pearson	NB IBI eigen	sttc	pearson
SC IBIcv	NB autocorr min	SC burst sizes	SC burst rate	SC burst rate	NB lengths	NB IPI cv	pearson	SC OFR
SC rate within burst	NB corr dim	NB IBI cv	SC OFR	SC ISIcv	SC rate within burst	SC ISIcv	NB rising	OFR
NB falling	NB lengths	SC burst rate	NB first harmonic	SC IBIcv	NB IPI cluster	pearson	NB electrodes speed	SC rate within burst
NB peaks	SC ISIcv	NB falling	NB lengths	SC lengths	NB IBI cluster	SC rate within burst	NB autocorr min	SC IBIcv
SC burst sizes	SC burst sizes	NB corr dim	NB IPI eigen	NB IPI cluster	NB IBI cv	NB IBI cv	NB IPI cluster	SC lengths
NB electrodes speed	NB first harmonic	NB peaks	NB IBI cv	NB IBI cv	NB rising	sttc	NB mutual info	NB mutual info
NB IBI cv	SC OFR	SC OFR	NB autocorr min	NB lengths	NB IPI eigen	NB IBI cluster	NB peaks	SC bursting electrodes
NB lengths	NB IBI eigen	NB electrodes	NB electrodes	NB size	NB electrodes speed	SC burst sizes	NB IPI eigen	NB falling
NB mutual info	NB IPI cv	rossum distance	SC ISIcv	NB falling	NB size	NB rising	SC rate within burst	NB rate
SC OFR	OFR	NB autocorr min	NB IPI cv	NB rising	sttc	SC lengths	NB IBI eigen	NB size
NB size	NB falling	NB size	NB corr dim	NB IPI eigen	SC lengths	NB IPI eigen	NB falling	NB IBI cv
NB IBI eigen	NB electrodes speed	NB lengths	SC IBIcv	NB IPI cv	SC bursting electrodes	NB size	NB IBI cv	NB electrodes
NB IPI eigen	SC lengths	NB electrodes speed	NB rising	NB electrodes speed	NB falling	NB mutual info	NB IBI cluster	NB IPI eigen
SC lengths	NB electrodes	SC bursting electrodes	NB falling	rossum distance	NB IPI cv	NB falling	SC OFR	NB lengths
NB IPI cv	NB peaks within burst	SC lengths	NB size	NB mutual info	SC burst sizes	NB electrodes	NB size	NB electrodes speed
NB rising	NB mutual info	NB first harmonic	NB IBI eigen	SC OFR	NB IBI eigen	NB electrodes speed	NB lengths	NB rising
NB IPI cluster	rossum distance	NB mutual info	NB mutual info	NB peaks	SC OFR	NB peaks	SC lengths	NB IBI eigen
NB IBI cluster	NB size	NB IBI eigen	SC bursting electrodes	OFR	NB peaks	NB lengths	OFR	NB peaks
OFR	SC IBIcv	NB rising	NB IPI cluster	NB peaks within burst	NB peaks within burst	SC OFR	NB peaks within burst	NB burstiness
rossum distance	SC bursting electrodes	SC IBIcv	NB electrodes speed	NB IBI eigen	NB mutual info	OFR	NB electrodes	NB IBI cluster
NB electrodes	NB rising	NB peaks within burst	SC lengths	SC burst sizes	rossum distance	rossum distance	SC bursting electrodes	NB IPI cluster
NB superburstiness	NB IPI cluster	NB IBI cluster	NB IBI cluster	SC bursting electrodes	OFR	SC bursting electrodes	rossum distance	NB IPI cv
SC bursting electrodes	NB IBI cluster	NB IPI cluster	NB peaks within burst	NB electrodes	NB electrodes	NB peaks within burst	NB IPI cv	NB peaks within burst
NB_ISI_cv	NB_superburstiness	NB_superburstiness	NB_superburstiness	NB_superburstiness	NB_superburstiness	NB_superburstiness	NB_superburstiness	NB_superburstiness

FIGURE 3.20: Table illustrating the feature importance ranking in WIV sparse RF classification with CF (upper plot) and with reduced CF (lower plot). Every subsampled condition is reported, both temporally (columns 2,3,4) and spatially (columns 50,40,30,20,10). For clarity, also the ranking without subsampling is shown in the first column. The red area represents the features that count for half of the importance in the classification.

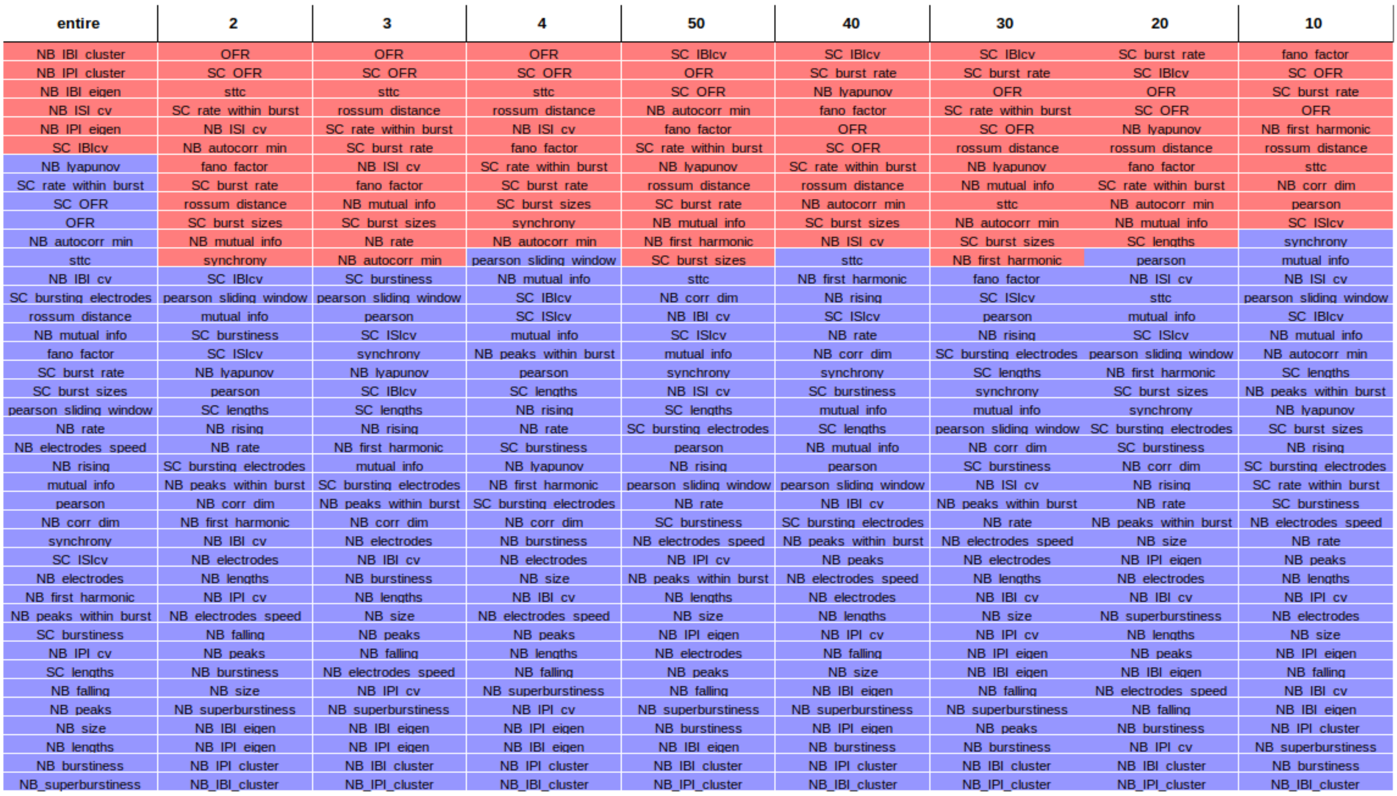

entire	2	3	4	50	40	30	20	10
NB IBI cluster	OFR	OFR	OFR	SC IBIcv	SC IBIcv	SC IBIcv	SC burst rate	fano factor
NB IPI cluster	SC OFR	SC OFR	SC OFR	OFR	SC burst rate	SC burst rate	SC IBIcv	SC OFR
NB IBI eigen	sttc	sttc	sttc	SC OFR	NB lyapunov	OFR	OFR	SC burst rate
NB ISI cv	SC rate within burst	rossum distance	rossum distance	NB autocorr min	fano factor	SC rate within burst	SC OFR	OFR
NB IPI eigen	NB ISI cv	SC rate within burst	NB ISI cv	fano factor	OFR	SC OFR	NB lyapunov	NB first harmonic
SC IBIcv	NB autocorr min	SC burst rate	fano factor	SC rate within burst	SC OFR	rossum distance	rossum distance	rossum distance
NB lyapunov	fano factor	NB ISI cv	SC rate within burst	NB lyapunov	SC rate within burst	NB lyapunov	fano factor	sttc
SC rate within burst	SC burst rate	fano factor	SC burst rate	rossum distance	rossum distance	NB mutual info	SC rate within burst	NB corr dim
SC OFR	rossum distance	NB mutual info	SC burst sizes	SC burst rate	NB autocorr min	sttc	NB autocorr min	pearson
OFR	SC burst sizes	SC burst sizes	synchrony	NB mutual info	SC burst sizes	NB autocorr min	NB mutual info	SC ISIcv
NB autocorr min	NB mutual info	NB rate	NB autocorr min	NB first harmonic	NB ISI cv	SC burst sizes	SC lengths	synchrony
sttc	synchrony	NB autocorr min	pearson sliding window	SC burst sizes	sttc	NB first harmonic	pearson	mutual info
NB IBI cv	SC IBIcv	SC burstiness	NB mutual info	sttc	NB first harmonic	fano factor	NB ISI cv	NB ISI cv
SC bursting electrodes	pearson sliding window	pearson sliding window	SC IBIcv	NB corr dim	NB rising	SC ISIcv	sttc	pearson sliding window
rossum distance	mutual info	pearson	SC ISIcv	NB IBI cv	SC ISIcv	pearson	mutual info	SC IBIcv
NB mutual info	SC burstiness	SC ISIcv	mutual info	SC ISIcv	NB rate	NB rising	SC ISIcv	NB mutual info
fano factor	SC ISIcv	synchrony	NB peaks within burst	mutual info	NB corr dim	SC bursting electrodes	pearson sliding window	NB autocorr min
SC burst rate	NB lyapunov	NB lyapunov	pearson	synchrony	synchrony	SC lengths	NB first harmonic	SC lengths
SC burst sizes	pearson	SC IBIcv	SC lengths	NB ISI cv	SC burstiness	synchrony	SC burst sizes	NB peaks within burst
pearson sliding window	SC lengths	SC lengths	NB rising	SC lengths	mutual info	mutual info	synchrony	NB lyapunov
NB rate	NB rising	NB rising	NB rate	SC bursting electrodes	SC lengths	pearson sliding window	SC bursting electrodes	SC burst sizes
NB electrodes speed	NB rate	NB first harmonic	SC burstiness	pearson	NB mutual info	NB corr dim	SC burstiness	NB rising
NB rising	SC bursting electrodes	mutual info	NB lyapunov	NB rising	pearson	SC burstiness	NB corr dim	SC bursting electrodes
mutual info	NB peaks within burst	SC bursting electrodes	NB first harmonic	pearson sliding window	pearson sliding window	NB ISI cv	NB rising	SC rate within burst
pearson	NB corr dim	NB peaks within burst	SC bursting electrodes	NB rate	NB IBI cv	NB peaks within burst	NB rate	SC burstiness
NB corr dim	NB first harmonic	NB corr dim	NB corr dim	SC burstiness	SC bursting electrodes	NB rate	NB peaks within burst	NB electrodes speed
synchrony	NB IBI cv	NB electrodes	NB burstiness	NB electrodes speed	NB peaks within burst	NB electrodes speed	NB size	NB rate
SC ISIcv	NB electrodes	NB IBI cv	NB electrodes	NB IPI cv	NB peaks	NB electrodes	NB IPI eigen	NB peaks
NB electrodes	NB lengths	NB burstiness	NB size	NB peaks within burst	NB electrodes speed	NB lengths	NB electrodes	NB lengths
NB first harmonic	NB IPI cv	NB lengths	NB IBI cv	NB lengths	NB electrodes	NB IBI cv	NB IBI cv	NB IPI cv
NB peaks within burst	NB electrodes speed	NB size	NB electrodes speed	NB size	NB lengths	NB size	NB superburstiness	NB electrodes
SC burstiness	NB falling	NB peaks	NB peaks	NB IPI eigen	NB IPI cv	NB IPI cv	NB lengths	NB size
NB IPI cv	NB peaks	NB falling	NB lengths	NB electrodes	NB falling	NB IPI eigen	NB peaks	NB IPI eigen
SC lengths	NB burstiness	NB electrodes speed	NB falling	NB peaks	NB size	NB IBI eigen	NB IBI eigen	NB falling
NB falling	NB size	NB IPI cv	NB superburstiness	NB falling	NB IBI eigen	NB falling	NB electrodes speed	NB IBI cv
NB peaks	NB superburstiness	NB superburstiness	NB IPI cv	NB superburstiness	NB superburstiness	NB superburstiness	NB falling	NB IBI eigen
NB size	NB IBI eigen	NB IBI eigen	NB IPI eigen	NB burstiness	NB IPI eigen	NB peaks	NB burstiness	NB IPI cluster
NB lengths	NB IPI eigen	NB IPI eigen	NB IBI eigen	NB IBI eigen	NB burstiness	NB burstiness	NB IPI cv	NB superburstiness
NB burstiness	NB IPI cluster	NB IBI cluster	NB IPI cluster	NB IBI cluster	NB IPI cluster	NB IBI cluster	NB IBI cluster	NB burstiness
NB_superburstiness	NB_IBI_cluster	NB_IPI_cluster	NB_IBI_cluster	NB_IPI_cluster	NB_IBI_cluster	NB_IPI_cluster	NB_IPI_cluster	NB_IBI_cluster

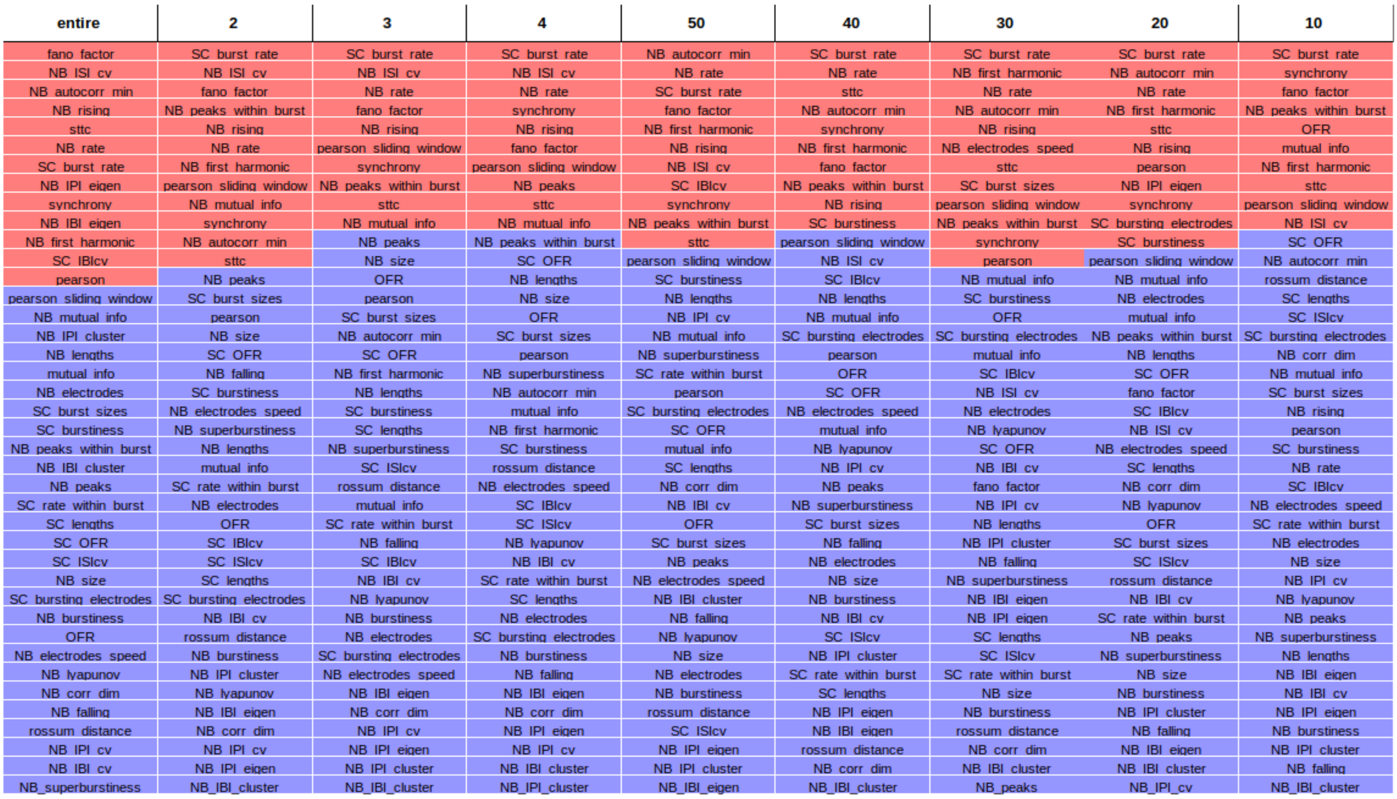

entire	2	3	4	50	40	30	20	10
fano factor	SC burst rate	SC burst rate	SC burst rate	NB autocorr min	SC burst rate	SC burst rate	SC burst rate	SC burst rate
NB ISI cv	NB ISI cv	NB ISI cv	NB ISI cv	NB rate	NB rate	NB first harmonic	NB autocorr min	synchrony
NB autocorr min	fano factor	NB rate	NB rate	SC burst rate	sttc	NB rate	NB rate	fano factor
NB rising	NB peaks within burst	fano factor	synchrony	fano factor	NB autocorr min	NB autocorr min	NB first harmonic	NB peaks within burst
sttc	NB rising	NB rising	NB rising	NB first harmonic	synchrony	NB rising	sttc	OFR
NB rate	NB rate	pearson sliding window	fano factor	NB rising	NB first harmonic	NB electrodes speed	NB rising	mutual info
SC burst rate	NB first harmonic	synchrony	pearson sliding window	NB ISI cv	fano factor	sttc	pearson	NB first harmonic
NB IPI eigen	pearson sliding window	NB peaks within burst	NB peaks	SC IBIcv	NB peaks within burst	SC burst sizes	NB IPI eigen	sttc
synchrony	NB mutual info	sttc	sttc	synchrony	NB rising	pearson sliding window	synchrony	pearson sliding window
NB IBI eigen	synchrony	NB mutual info	NB mutual info	NB peaks within burst	SC burstiness	NB peaks within burst	SC bursting electrodes	NB ISI cv
NB first harmonic	NB autocorr min	NB peaks	NB peaks within burst	sttc	pearson sliding window	synchrony	SC burstiness	SC OFR
SC IBIcv	sttc	NB size	SC OFR	pearson sliding window	NB ISI cv	pearson	pearson sliding window	NB autocorr min
pearson	NB peaks	OFR	NB lengths	SC burstiness	SC IBIcv	NB mutual info	NB mutual info	rossum distance
pearson sliding window	SC burst sizes	pearson	NB size	NB lengths	NB lengths	SC burstiness	NB electrodes	SC lengths
NB mutual info	pearson	SC burst sizes	OFR	NB IPI cv	NB mutual info	OFR	mutual info	SC ISIcv
NB IPI cluster	NB size	NB autocorr min	SC burst sizes	NB mutual info	SC bursting electrodes	SC bursting electrodes	NB peaks within burst	SC bursting electrodes
NB lengths	SC OFR	SC OFR	pearson	NB superburstiness	pearson	mutual info	NB lengths	NB corr dim
mutual info	NB falling	NB first harmonic	NB superburstiness	SC rate within burst	OFR	SC IBIcv	SC OFR	NB mutual info
NB electrodes	SC burstiness	NB lengths	NB autocorr min	pearson	SC OFR	NB ISI cv	fano factor	SC burst sizes
SC burst sizes	NB electrodes speed	SC burstiness	mutual info	SC bursting electrodes	NB electrodes speed	NB electrodes	SC IBIcv	NB rising
SC burstiness	NB superburstiness	SC lengths	NB first harmonic	SC OFR	mutual info	NB lyapunov	NB ISI cv	pearson
NB peaks within burst	NB lengths	NB superburstiness	SC burstiness	mutual info	NB lyapunov	SC OFR	NB electrodes speed	SC burstiness
NB IBI cluster	mutual info	SC ISIcv	rossum distance	SC lengths	NB IPI cv	NB IBI cv	SC lengths	NB rate
NB peaks	SC rate within burst	rossum distance	NB electrodes speed	NB corr dim	NB peaks	fano factor	NB corr dim	SC IBIcv
SC rate within burst	NB electrodes	mutual info	SC IBIcv	NB IBI cv	NB superburstiness	NB IPI cv	NB lyapunov	NB electrodes speed
SC lengths	OFR	SC rate within burst	SC ISIcv	OFR	SC burst sizes	NB lengths	OFR	SC rate within burst
SC OFR	SC IBIcv	NB falling	NB lyapunov	SC burst sizes	NB falling	NB IPI cluster	SC burst sizes	NB electrodes
SC ISIcv	SC ISIcv	SC IBIcv	NB IBI cv	NB peaks	NB electrodes	NB falling	SC ISIcv	NB size
NB size	SC lengths	NB IBI cv	SC rate within burst	NB electrodes speed	NB size	NB superburstiness	rossum distance	NB IPI cv
SC bursting electrodes	SC bursting electrodes	NB lyapunov	SC lengths	NB IBI cluster	NB burstiness	NB IBI eigen	NB IBI cv	NB lyapunov
NB burstiness	NB IBI cv	NB burstiness	NB electrodes	NB falling	NB IBI cv	NB IPI eigen	SC rate within burst	NB peaks
OFR	rossum distance	NB electrodes	SC bursting electrodes	NB lyapunov	SC ISIcv	SC lengths	NB peaks	NB superburstiness
NB electrodes speed	NB burstiness	SC bursting electrodes	NB burstiness	NB size	NB IPI cluster	SC ISIcv	NB superburstiness	NB lengths
NB lyapunov	NB IPI cluster	NB electrodes speed	NB falling	NB electrodes	SC rate within burst	SC rate within burst	NB size	NB IBI eigen
NB corr dim	NB lyapunov	NB IBI eigen	NB IBI eigen	NB burstiness	SC lengths	NB size	NB burstiness	NB IBI cv
NB falling	NB IBI eigen	NB corr dim	NB corr dim	rossum distance	NB IPI eigen	NB burstiness	NB IPI cluster	NB IPI eigen
rossum distance	NB corr dim	NB IPI cv	NB IPI eigen	SC ISIcv	NB IBI eigen	rossum distance	NB falling	NB burstiness
NB IPI cv	NB IPI cv	NB IPI eigen	NB IPI cv	NB IPI eigen	rossum distance	NB corr dim	NB IBI eigen	NB IPI cluster
NB IBI cv	NB IPI eigen	NB IPI cluster	NB IBI cluster	NB IPI cluster	NB corr dim	NB IBI cluster	NB IBI cluster	NB falling
NB_superburstiness	NB_IBI_cluster	NB_IBI_cluster	NB_IPI_cluster	NB_IBI_eigen	NB_IBI_cluster	NB_peaks	NB_IPI_cv	NB_IBI_cluster

FIGURE 3.21: Table illustrating the feature importance ranking in batch sparse RF classification with CF (upper plot) and with reduced CF (lower plot). Every subsampled condition is reported, both temporally (columns 2,3,4) and spatially (columns 50,40,30,20,10). For clarity, also the ranking without subsampling is shown in the first column. The red area represents the features that count for half of the importance in the classification.

Afterwards, we discuss about the **batch dense** classifications (see figure 3.19). In the case with CFs (upper table), the most striking difference with the normal condition is the loss of the first place of the NB ISI that drop out from the red area. Its place was taken by the SC bursting electrodes, except in the case of the highl spatially subsampled recordings (20 and 10 electrodes), where the SC lengths and the NB electrodes are more important. Following the previous trends, the OFR, SC OFR, NB first mminimum of autocorrelation and van Rossum distance keep being in the red area and the IPI/IBI related measure in the last positions, together with superburstiness. On the other hand, when the samples were chosen considering reduced CFs, the NB ISI CV is still important, even in subsampled conditions. However, also here the SC bursting electrodes and the number of active electrodes in NB, as well as the NB burstiness, are high-scored features. It is interesting to notice the multivariate measures present in the red area in the spatially subsampled condition because in the last column five over twelve features are correlations, even if van Rossum is not included. In addition, the OFR and SC OFR do not seem to be that important as they almost never lie in the red area. Also in this case, among the worst features we could find the IBI/IPI related measures and superburstiness.

In figure 3.20 the classifications based on the **WIV sparse** condition are illustrated, both with CFs (upper table) and reduced CFs (lower table). In the former case, among the most important features there are the mutual info, NB ISI CV, synchrony and SC burst rate. Also some multivariate features, as Fano factor and Pearson (sliding window) play an important role in the classification. In the last place, together with the usual IPI/IBI related measures and superburstiness, we could find the NB electrode speed. Conversely, in the case with reduced CFs, apart the NB ISI CV, the ranking considerably changed. Here, among the best-scored features it is possible to find the NB rate and the SC burstiness, particularly important for the temporally subsampled case, and NB first harmonic and Fano factor for the spatially subsampled case, except for 10 electrodes recordings, as the first two places are occupied by Pearson (sliding window) and the correlation dimension. Differently to the other classifications, the OFR and the SC OFR do not show good results as sometimes they even appear in the last positions. Moreover, among the worst scored features there are also the van Rossum distance, the SC bursting electrode and the number of active electrode in NB in the spatially subsampled case, as well as the IBI/IPI related measures and the superburstiness, which are also particularly predominant features in the temporally subsampled lower rankings.

Finally, the case of the **batch sparse** classification is reported in figure 3.21. As we already said, the classification with CFs shows an odd behaviour due to the high level of accuracy and the IPI/IBI related measures that occupy the red area. However, when considering classification affected by subsampling, the 'normal' trend is restored. In the temporally subsampled classification, the best scored features are OFR and SC OFR, together with the STTC and the van Rossum distance. In the spatial subsampling, among the best ranked features one can find the SC IBI CV, the SC burst rate and the Fano factor, as well as the already mentioned features in the temporal subsampling case. In the spatial subsampling classification, together with the usual IBI/IPI related measures, the NB burstiness also appears in the lower part of the ranking. When reducing the CFs the feature that seem to be more involved in the classification is the SC burst rate and, even if in lower position, also the NB rate. For the temporally subsamples FI, also the NB ISI CV plays an important role. As far as it is concerned the lower ranking positions, the correlation dimension, the van Rossum distance and the NB falling time are present together with the IBI/IPI related measures.

3.2.3 General Consideration

Due to the high variability between classifications it is not easy to find an underlying pattern about the most important features. Thus, according to the classification task of interest, one should carefully choose the most appropriate features, looking at every factor that could affect the performance, such as experimental conditions, confounding factors and level of subsampling, both temporal and spatial. Nevertheless, we highlight some general trends, unraveled after carefully analysing every case, reported in the following bucket list.

- Let us start from the **worst features**, the IBI/IPI number of clusters and eigenvalue ratios, as well as the CVs, that are always placed in the lower part of the rankings. A possible explanation for their bad behaviour can be found in the fact that they need many NBs to be properly calculated. In other words, in order to extract meaningful information from these measures, long recordings are needed. Thus, seeing the problems related with the culture survival, they are not suitable measures for this kind of analysis if extended recordings cannot be performed.

- We reported considerable changes when performing the same type of classification with different levels of **confounding factors**, at least for the decisive features in the classification performance. When performing classification with complex data is important to carefully select the samples in order to drop out as much variability as possible, stratifying the data but being aware of the overfitting issue by keeping enough samples.

- Interestingly, the number of features counting for half of the importance (features placed in the red area in the previous tables) did not change significantly in the different subsampled conditions. This could mean that the **number of features** needed to perform the classification is not affected by the subsampling. As we already said, many features usually yields to better performances despite of the recording length and the number of electrodes considered.

- When we looked at the rankings under spatial and temporal subsampling, we usually did not observe striking differences between the two conditions, even if some exception have been reported. Hence, the classifications are quite **robust** when the recordings are affected by **subsampling**. Although a single measure can be affected by subsampling, the overall classification still shown good performances.

- In this thesis our main focus was on the measures extracted from the network bursts. However, we tested also many measures extracted from spiking activity and **single channel** recordings. It came out that they are actually important to characterize cultured neural network activity as the OFR, many SC measures and correlations often occupied high-ranked feature importance positions. In other words, they are more affected by the intrinsic variability of the neural activity *in vitro*.

In addition to the specific-case classification analysis, we wanted to study the general robustness of the extracted measures considering the overall effect of the culture variability due to density, WIV and batch, as well as the temporal and spatial subsampling influence. Therefore, we calculated the number of times each feature fell in the red area of the previous tables, that is, how many times it counted for half of the importance in the classification. Then, we normalized this value for the total number of classifications performed and we called it Half Importance Index (HII) .

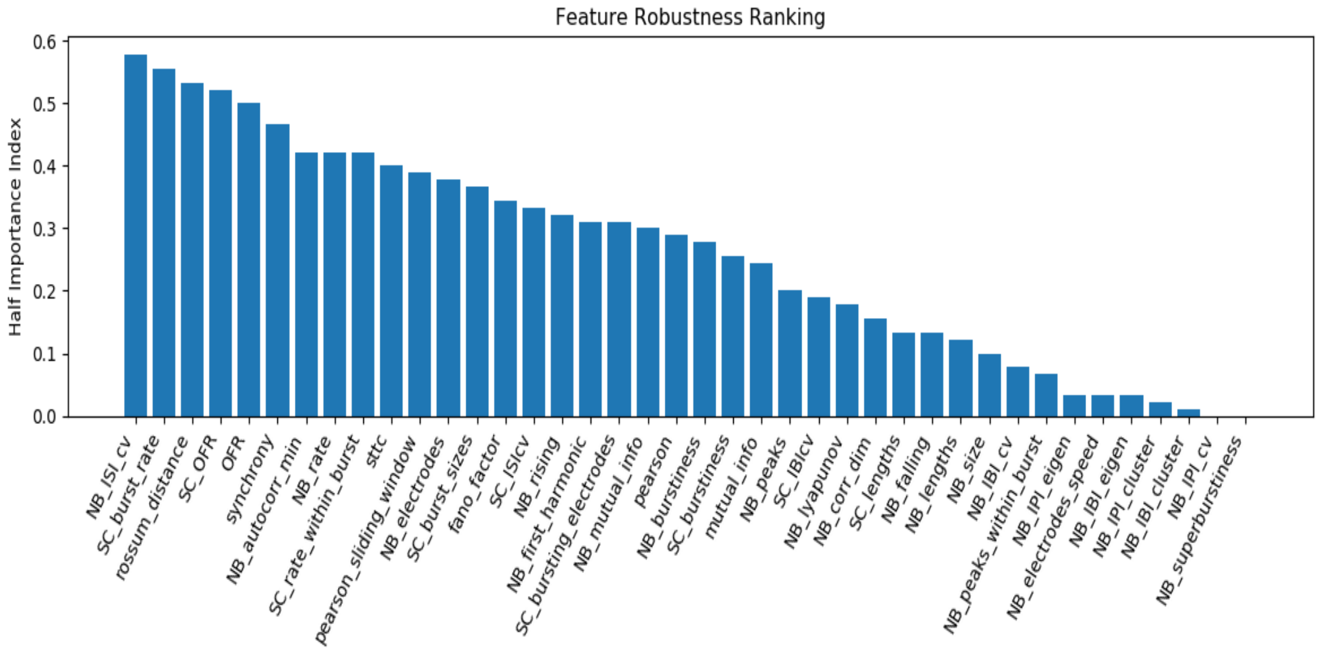

FIGURE 3.22: Ranking of all the 40 features according to the number of time they account for half of the importance in the RF classification, normalized by the total number of classification performed. For the sake of brevity we called it Half Importance index. Considering also the subsampling analysis we performed 90 different classifications.

In figure 3.22 we ranked the features in decreasing order of importance. First of all, the only features that have an HII above 0.5 are the NB ISI CV, the SC burst rate, the van Rossum distance and the SC OFR, noticing that the last three derived from single-channel recordings. Moreover, we found out that the most important feature is the NB ISI CV, confirming somewhat the study reported in [8]. In this study they also found the NB IBI CV to be important while in our work it does not show a good behaviour. However, we should remember that in [8] they only classified cultures in the early developmental stages (first two WIVs), without considering other experimental conditions or subsampling effects.

Looking at the worst features, together at the already mentioned IBI/IPI related measures, the superburstiness has null value of HII, probably due to its high divergences among the cultures as it did not show to follow a pattern according to the experimental conditions. However, this spatiotemporal activity is not yet well understood and should be further analysed because it is believed to play an important role in information processing [54].

In general, the multivariate measures have an important role in the classifications, and in addition to the van Rossum distance, also the synchrony and the STTC have a good HII score. As expected the Pearson correlation is not really suitable for spiking data although the sliding window approach shows better results because it behaves better with quiescent activity periods.

As far as it is concerned the NB measures, the NB rate is the one with higher HII. However, the general trend of this kind of measures shows quite low importance, as for example for the measures related to the duration. Though the rising time seems to behave well, the NB length and falling time report low HII values.

Considering the novel measures that we calculated, just the first minimum of the autocorrelation appears among the best positions. Conversely, all the features extracted by means of the Poincare plots do not show high value of HII, making them not good measures for characterize the neural network activity for our classification purpose, that is, for discriminating cultures with different age, density and batch. Moreover, an high computational effort is needed for calculating them so they will make the classification task quite time-consuming if they have to be extracted for an high number of recordings. However, we are not neglecting their utility in other analysis purpose. For example, the attractor-based measures, like Lyapunov exponent and correlation dimension, are quite stable over different experimental conditions so they could describe intrinsic dynamical and geometrical properties of the culture system and they can be useful in classification task where the spontaneous culture variability has to be discarded.

In conclusion, due the importance shows by the multivariate features, alternative ways for characterizing cultured neural network activity should be addressed to network-based measures. In fact, from correlation measures one can derive a functional network from which novel features can be studied [12]. As we already mentioned in Chapter 1, the cultured neurons networks are extremely characterized by their anatomical linkage and the functional connectivity that elicits.

Conclusion

In conclusion, we discuss the most important results at the light of the motivation behind the analysis, with a particular focus on the difficulties met and the possible future developments to improve this work.

The data analysed in this work represent the spiking activity of cultured neural networks recorded via multi-electrode array (MEA) [55]. The neurons cultured *in vitro* are a cheap and simplified experimental protocol that allows to study the neural network activity in a more controlled manner. MEA is a device designed for multi-unit an high temporal resolution recordings of the neural network activity is coupled with. One of the most interesting patterns emerging from the activity is the network burst, a stereotyped spatiotemporal event that involves the spiking or the bursting activity from many points in the network in a short period of time. This highly synchronized events are separated by longer periods of sparse and random activity. The characterization of the cultured neural network is mostly based on the description of the changes in the network bursts activity. In the cultured neural networks many factors could affect this activity, i.e. the plating density, the culture age, inter-batch and intra-batch culture variability. The latter could be due to genetic differences between the embryos even if they come from the same mother or if analysing cultures harvested from different brain tissues. However, usually the culture-by-culture variability is lower than the other factor (see [55]) and we did not considered it in our analysis.

This thesis aims to characterize these sources of variability extracting a broad range of measures that exhaustive describe a wide variety of activity patterns, as network bursts and spikes, both at single channel and network level. We also calculated measures using techniques borrowed from spike train synchrony methods and Poincaré plots. The analysis were performed by means of different statistical methods: checking the trends and distributions of each measure, using unsupervised learning as PCA and clustering, and finally implementing a random forest classifier. The classification tasks considered were five: dense vs sparse, different WIVs in dense condition, different WIVs in sparse condition, different batches in dense condition and different batches in sparse condition.

The analysis tools developed in this work can be used with any data obtained from experiments involving cell cultures coupled with MEAs. The ultimate goal of this work is not just classifying different culture conditions, as density, age or batch, but implementing a general analysis methodology that can be used also for data coming from stimulated network activity, both chemically and electrically. Studying how the neural network responds to stimuli can lead to new insights in brain functions and pathological disrupted mechanisms. Also the network behaviour perturbed by chemical compounds and drugs could lead to new findings useful for disease treatments and toxicology screening.

According to the literature [6, 35, 55] the activity *in vitro* starts with random sparse spiking on few channels. During the first two weeks *in vitro* the networks grow fast, create new connections, boost the level of synchronicity, and finally give rise to bursting activity, a pattern that appears in different forms, depending on the developmental stage, density and batch. We confirmed the results found in literature: the neural network transits from low activity at early developmental ages (e.g., the first week *in vitro*) to high-frequency coordinated bursting at later stages (e.g., the second week *in vitro* and beyond). The NB changed shape, from broad and infrequent NBs, to frequent sharp NBs with a prominent peak.

Before performing the classification, we checked the class segregation to preventively inspect how much variability affects the data simply looking at the single distributions or by means of unsupervised learning methods, as PCA and clustering. The complexity of the data yield to non-linearly separable classes, as it was difficult to visually delineate neat groups in the reduced feature space obtained by PCA or find the right class labels by means of K-means algorithm. From this preliminary analysis came out that only the density classes were quite distinguishable. Separate sparse and dense classes was the easiest task because the cultures shown considerable different behaviors in the two densities. For example, the overall activity is in general lower in sparse condition as the neuron-electrode coupling is fainter due to the higher spread of neurons in the plating volume. Moreover, the NB pattern appeared with delay in sparse cultures, their shapes also differed as they were in general shorter and less frequent and, as the neurons made less connections, the multivariate measures shown lower values. For the other cases the class separability analysis did not show good results. Thus, more sophisticate methods are needed to discern the high diversity of the neural activity, that is, by using supervised learning technique as random forest, the same method used in [8].

The outcomes of the random forest classifier confirmed the results about the density classification, as it achieved the highest accuracy with respect to the other classification tasks. As far as it is concerned the WIV classes, even using a wide range of features, it was hard to recognize the right WIV class also with the random forest classification. Thus, considering an entire WIV is not advised and comparing activity in distinct DIVs should lead to better results, if one possesses enough recordings from the same culture age. The worst results shown by the WIV classifications are due to the changes induced by development *in vitro*. As the neural network grows, it creates new synaptic connections between neurons trough activity-dependent mechanism. The other factor considered is the inter-batch variability, a subtle element that actually affected the detected activity. In fact, the random forest classifications shown good performance results, even higher than the ones reported in WIV classifications, demonstrating the possibility of distinguish cultures coming from different batches. Each batch contains neurons extracted from different pups so they could still retain some innate characteristics and properties originating from the brain tissue they were derived from. Despite these neurons having been dissociated before plating, the activity may be determined by genetic factors. Thus, more sophisticate statistical methods are needed while try to include in the same analysis non-sister cultures recordings. The analysis methodology implemented in this thesis can be useful to individuate the features that are less affected by batch variability.

We implemented a random forest algorithm because, in addition to performing classification, it is able to estimate the contribution of each feature to the prediction capacity, the so-called feature importance score. The first impression we obtained from the classifications was the number of feature needed to reliably identify the categories examined. We counted how many features were involved for half of the importance. Although for each condition the parameters with higher importance were different, the classifier always needed many features to achieve good performance. This shows how using multiple features collectively provides more robust discriminatory power then relaying on a single or few measures.

Another consideration about the classifications is the role of the confounding factors. As we already said, the data are characterized by high intrinsic variability that has to be considered when choosing the samples to classify. When reducing the confounding factors the classification accuracy was considerably higher, and usually less features were needed. However, when trying to get rid of the confounding factors one has to be careful to not discard too many samples.

When we reduced the confounding factors the number of remaining samples was too low so to avoid overfitting we decided to split in equal parts the recordings. As expected, the classification performance improved and more reliable results were obtained. Moreover, we could test the robustness of the measures over the temporal subsampling, that is, how the classification is affected if shorter recordings are used. From the results we may speculate that the 30-minutes-long recordings can be reduced to one quarter and still faithful measures can be extracted. The only features that do not seem to behave well under temporal subsampling were the IBI/IPI related measures that due to their nature they require to be calculated from a recording containing many network bursts. It would be interesting to keep splitting the recordings until the overall accuracy starts to decline. However, due to time-consumption problem (the computation of all the measures from all the recordings needed few days) we could not go further with the splittings. Nevertheless, we could speculate that if we split the recording up to several seconds, the average length of a NB, we might still extract meaningful measures from the time-series.

Another problem due to the nature of the neural recording devices is the spatial subsampling cause they have to assess an enormous number of neurons with a limited spatial resolution. Thus, investigate to which extend the network properties can be defined with fewer electrodes is important because we can extrapolate the robustness of the features when recorded with the full device. Moreover, studying the spatial subsampling can have implication on *in vitro* experiments using multi-well MEAs. These devices are usually built with a reduced number of electrodes per well for permitting to study many cultures in just one plate. Moreover, assessing the robustness of the measures extracted with less electrodes can be useful in the case of malfunctions of the MEA chip, as many times some electrodes are deteriorated or do not detect the extracellular potentials for other reasons. Our finding suggests that, in general, reducing the number of electrodes does not affect considerably the classification. Probably the activity patterns were gross enough to be detected even with fewer electrodes or maybe the more important features are the single-channel measures that by definition are not affected that much by subsampling. In order to better assess which measures are more affected by subsampling it would be interesting to repeat the classification just using a particular group of measures in order to adopt only the most robust. An exception was found for the case with extremely subsampled recordings, i.e. with only 10 electrodes, where the more subtle changes in the activity could not be easily detected.

Also in the case of the subsampling, both temporal and spatial, we checked how the feature importance was affected. Apart the IBI/IPI related measures, we did not find a particular group of features more sensitive to subsampling, because for each type of classification we observed different trends. Therefore, as the type of measures available for describing neural network activity are innumerables, depending on the aim of the research one should pick the more suitable features. However, when we calculated the Half Importance Index, it came out that the more robust measure is the NB ISI CV, as well as other measures extracted form single-channel recordings and multivariate measures. Surprisingly, the network burst related measures were not of primarily importance in the classification. Probably, multi-channel measures are less affected by intrinsic variability as they take into account the activity recorded by many electrodes. Some of the measures, even if correlated, shown different importances, as for example the rising time has higher feature score than the network burst length or falling time, or among all the multivariate measures the van Rossum distance shows the highest HII.

In some studies, e.g. in classification between spontaneous and perturbed activity, the inner sources of variability, due to density, age and batch, have to be discarded. This implies that the features that have an high HII score in our classifications, which try to discriminate these culture conditions, might not be suitable for any purpose. Thus, in each classification task some case-specific measures have to be extracted using the analysis pipeline here implemented.

The measures extracted by means of the Poincaré plots shown quite poor sensitivity, making them not that suitable for our classification purpose. However, as we have already stressed out, in different classification conditions they can still be good measures.

Due to the results obtained with the multivariate measures, an alternative way to characterize these data is by means of network-based measures. As we are dealing with neural network activity, these measures seem the natural way for studying their underneath spatio-temporal patterns. We could apply the complex network theory for analysing this kind of non-linear data because from the multivariate measures one can obtain a functional connectivity. From the functional connectivity is possible to extract graph theory-like measures of segregation and integration, as degree distribution, centrality and connectivity. Moreover, if the neural network structure is available, the link between functional and structure connectivity could be assessed and the activity-dependent mechanisms that play a pivotal role in shaping the networks during development can be studied.

Furthermore, the analysis pipeline could be tested also using synthetic data. Using computational models, properly fitted with experimental data, is useful for having more control over some parameters, as for example for testing the role of the network structure over the dynamics. Studying the role of the network topology and its relationship with the functional connectivity can shed lights on pivotal neural mechanisms not yet well understood. Moreover, using simulated neural network one could ideally record or stimulate every neurons, getting rid of the spatial subsampling issues. Through the use of computational model it is possible to study how the noise influences the network activity, as it is thought to play an important role on dynamics. The optimal noise level indicates the presence of stochastic resonance, which allows the network dynamics to respond with high sensitivity to external signals, facilitating learning and adaptation. Moreover, in a simulated neural network one can inspect the role of excitatory and inhibitory competitive balance, an interplay that is important for the emergence of network burst patterns and for many neural functions.

As far as it is concerned the machine learning techniques, we used random forest classification because it calculates also the feature importance score. However, the next steps of the analysis should be selecting the best features to apply in a more performant classifier. In addition, also other type of data could be tested, for example coming from different preparations, cells (e.g. human stem cells) or recorded with more performant MEA devices, as high-density MEA or multi-well MEA. The technological advance together with new powerful analysis approaches will enable us to deeply understand the more intricate mechanisms behind the brain functions.

Nomenclature

ASDR	Array-wide Spike Detection Rate
BL	Burst Length
BR	Burst Rate
BS	Burst Size
BI	Burstiness Index
CV	Coefficient of Variation
CF	Confounding Factor
CC	Correlation Coefficient
D	Correlation Dimension
DIV	Day *In Vitro*
FT	Falling Time
FF	Fano Factor
FI	Feature Importance
HII	Half Importance Index
IBI	Inter Burst Interval
IPI	Inter Peak Interval
ISI	Inter-Spike Intervals
KMC	K-Means Clustering
KS	Kolmogorov-Smirnoff
LE	Lyapunov Exponent
MFR	Maximum Firing Rate
MC	Multi Channel
MEA	Multi-Electrode Array
NBRP	Network Burst Rate Profile
NB	Network Burst
OFR	Overall Firing Rate
PCA	Principal component analysis

RF	Random Forest
RC	Recruitment Count
RT	Rising Time
SC	Single Channel
STTC	Spike Time Tiling Coefficient
SD	Standard Deviation
$\chi(N)$	Synchrony
DR	van Rossum Distance
WIV	Week *In Vitro*

Acknowledgement

I eventually arrived at the end of this long journey and it is time to stop and look backwards. In the last two years I had so many experiences that made me grow up a lot, both in academy and in life. However, the experiences without the people who have permitted them to be possible are meaningless.

First of all, I would like to thank all the members of the Computational Neuroscience group at Tampereen Yliopisto. During the amazing five months of my internship, they scientifically inspired me and enabled me to get in touch for the first time with the world of research, made me understand that this will be my path. In particular, a special thanks goes to the person who had the idea of this thesis, Dott. Jugoslava Acimovic who believed in my potentiality and, together with Prof. Daniel Remondini, followed me during the writing, giving me many wise hints, which turned to be crucial to successfully finalize this work. Moreover, an essential thanks is directed to Steve M. Potter of the Georgia Institute of Technology who gave me the permission to analyse the neural network activity data.

Nevertheless, if I could achieve this important goal is also because of all the people I have met during my travels around Italy, Portugal, Brazil and Finland. Moreover, an important contribution is addressed to my family and friends from Laverino, my hometown, who always have been close to me whenever far away I was.

It has always been my dream studying the complexity of the brain and with this thesis I think I started on the right foot. Because this is not an end but just the beginning of new exciting adventures.

As the Finnish quotation reported at the beginning of the thesis says: *"The happiness will not be found looking for it but just living"*.

Thanks, Obrigado, Kiitos, GRAZIE!

Bibliography

[1] Gladkov Arseniy et al. “Functional Connectivity of Neural Network in Dissociated Hippocampal Culture Grown on Microelectrode Array”. In: *Sovremennye tehnologii v medicine* 9 (June 2017), p. 61. DOI: `10.17691/stm2017.9.2.07`.

[2] Douglas Bakkum et al. “Parameters for burst detection”. In: *Frontiers in computational neuroscience* 7 (Jan. 2013), p. 193. DOI: `10.3389/fncom.2013.00193`.

[3] Douglas Bakkum et al. “Removing Some ‘A’ from AI: Embodied Cultured Networks”. In: *Lecture Notes in Artificial Intelligence (Subseries of Lecture Notes in Computer Science)* 3139 (July 2003), pp. 130–145. DOI: `10.1007/978-3-540-27833-7_10`.

[4] Birendra Biswal and Chandan Dasgupta. “Stochastic neural network model for spontaneous bursting in hippocampal slices”. In: *Physical review. E, Statistical, nonlinear, and soft matter physics* 66 (Dec. 2002), p. 051908. DOI: `10.1103/PhysRevE.66.051908`.

[5] Frega Chiappalone Pasquale. “In Vitro Neuronal Networks From Culturing Methods to Neuro-Technological Applications”. In: *Advances in Neurobiology, Spriger* (2019). DOI: `https://doi.org/10.1007/978-3-030-11135-9`.

[6] Michela Chiappalone et al. “Dissociated cortical networks show spontaneously correlated activity patterns during in vitro development”. In: *Brain Research* 1093.1 (2006), pp. 41 –53. ISSN: 0006-8993. DOI: `https://doi.org/10.1016/j.brainres.2006.03.049`. URL: `http://www.sciencedirect.com/science/article/pii/S0006899306008018`.

[7] Ellese Cotterill and Stephen Eglen. “Burst detection methods”. In: (Feb. 2018).

[8] Ellese Cotterill et al. “Characterization of Early Cortical Neural Network Development in Multiwell Microelectrode Array Plates”. In: *Journal of Biomolecular Screening* 21 (Mar. 2016). DOI: `10.1177/1087057116640520`.

[9] Catherine Cutts and Stephen Eglen. “Detecting Pairwise Correlations in Spike Trains: An Objective Comparison of Methods and Application to the Study of Retinal Waves”. In: *Journal of Neuroscience* 34 (Oct. 2014), p. 14288. DOI: `10.1523/JNEUROSCI.2767-14.2014`.

[10] P. Dayan and LF Abbott. “Theoretical Neuroscience:computational and mathematical modeling of neural systems”. In: *MIT Press* (2001). DOI: `ISBN0-262-04199-5`.

[11] Philippe Faure and Henri Korn. “Is there chaos in the brain? I. Concepts of nonlinear dynamics and methods of investigation”. In: *Comptes rendus de l’Académie des sciences. Série III, Sciences de la vie* 324 (Oct. 2001), pp. 773–93. DOI: `10.1016/S0764-4469(01)01377-4`.

[12] A. Fornito, A. Zalesky, and Edward Bullmore. *Fundamentals of Brain Network Analysis*. Mar. 2016, pp. 1–476.

[13] David Golomb. “Neuronal synchrony measures”. In: *Scholarpedia* 2.1 (2007), p. 1347. DOI: `10.4249/scholarpedia.1347`.

[14] P. Grassberger. “Grassberger-Procaccia algorithm”. In: *Scholarpedia* 2.5 (2007). revision #91330, p. 3043. DOI: `10.4249/scholarpedia.3043`.

[15] T Gritsun et al. “Network bursts in cortical cultures are best simulated using pacemaker neurons and adaptive synapses”. In: *Biological cybernetics* 102 (Feb. 2010), pp. 293–310. DOI: `10.1007/s00422-010-0366-x`.

[16] G.W. Gross et al. “A new fixed-array multi-microelectrode system designed for long-term monitoring of extracellular single unit neuronal activity in vitro”. In: *Neuroscience Letters* 6.2 (1977), pp. 101 –105. ISSN: 0304-3940. DOI: `https://doi.org/10.1016/0304-3940(77)90003-9`. URL: `http://www.sciencedirect.com/science/article/pii/0304394077900039`.

[17] J. Haaksma et al. “The dimension of 2D and 3D Poincare plots obtained from 24 hour ECG registrations”. In: (Oct. 2002), pp. 453 –456. DOI: `10.1109/CIC.2002.1166807`.

[18] Vahid Houshyarifar and Mehdi AMIRANI. “Early detection of sudden cardiac death using Poincaré plots and recurrence plot-based features from HRV signals”. In: *TURKISH JOURNAL OF ELECTRICAL ENGINEERING COMPUTER SCIENCES* 25 (Jan. 2017), pp. 1541–1553. DOI: `10.3906/elk-1509-149`.

[19] Eugene M. Izhikevich. “Bursting”. In: *Scholarpedia* (2006). DOI: `doi:10.4249/scholarpedia.1300`.

[20] Andrew F.M. Johnstone et al. “Microelectrode arrays: A physiologically based neurotoxicity testing platform for the 21st century”. In: *NeuroToxicology* 31.4 (2010), pp. 331 –350. ISSN: 0161-813X. DOI: `https://doi.org/10.1016/j.neuro.2010.04.001`. URL: `http://www.sciencedirect.com/science/article/pii/S0161813X10000677`.

[21] Holger Kantz and Thomas Schreiber. “NONLINEAR TIME SERIES ANALYSIS”. In: *Cambridge University Press* (2003).

[22] Raeyoung Kim et al. “Recent trends in microelectrode array technology for in vitro neural interface platform”. In: *Biomedical Engineering Letters* 4 (June 2014), pp. 129–141. DOI: `10.1007/s13534-014-0130-6`.

[23] Thomas Kreuz. “Measures of neuronal signal synchrony”. In: *Scholarpedia* 6.12 (2011), p. 11922. DOI: `10.4249/scholarpedia.11922`.

[24] Thomas Kreuz. “Measures of spike train synchrony”. In: *Scholarpedia* 6.10 (2011), p. 11934. DOI: `10.4249/scholarpedia.11934`.

[25] Anna Levina and V. Priesemann. “Subsampling scaling”. In: *Nature Communications* 8 (May 2017), p. 15140. DOI: `10.1038/ncomms15140`.

[26] Zonghua Liu. “Chaotic Time Series Analysis”. In: *Mathematical Problems in Engineering* 2010 (Mar. 2010). DOI: `10.1155/2010/720190`.

[27] Paolo Massobrio et al. “Activity modulation elicited by electrical stimulation in networks of dissociated cortical neurons”. In: *Conference proceedings : ... Annual International Conference of the IEEE Engineering in Medicine and Biology Society. IEEE Engineering in Medicine and Biology Society. Conference* 2007 (Feb. 2007), pp. 3008–11. DOI: `10.1109/IEMBS.2007.4352962`.

[28] P.W. McCarthy and S.N. Lawson. “Axonal conduction properties of antidromically identified neurons inrat barrel cortex”. In: *Somatosensory Motor Research* 18.3 (2001), pp. 202 –210. ISSN: 0899-0220. DOI: `10.1080/01421590120072196`.

[29] P.W. McCarthy and S.N. Lawson. “Cell type and conduction velocity of rat primary sensory neurons with calcitonin gene-related peptide-like immunoreactivity”. In: *Neuroscience* 34.3 (1990), pp. 623 –632. ISSN: 0306-4522. DOI: `https://doi.org/10.1016/0306-4522(90)90169-5`. URL: `http://www.sciencedirect.com/science/article/pii/0306452290901695`.

[30] Wilfried Nisch Karl-Heinz Boven Michael Fejtl Alfred Stett and Andreas Moller. “On Micro-Electrode Array Revival: Its Development, Sophistication of Recording, and Stimulation”. In: *Advances in Network Electrophysiology* (2006).

[31] Andreas C. Müller and Sarah Guido. “Introduction to Machine Learning with Python. A Guide for Data Scientists”. In: *O’Reilly* (2017).

[32] Yoonkey Nam and Bruce Wheeler. “In Vitro Microelectrode Array Technology and Neural Recordings”. In: *Critical reviews in biomedical engineering* 39 (Jan. 2011), pp. 45–61. DOI: `10.1615/CritRevBiomedEng.v39.i1.40`.

[33] Alessandro Napoli, Jichun Xie, and Iyad Obeid. “Understanding the temporal evolution of neuronal connectivity in cultured networks using statistical analysis”. In: *BMC neuroscience* 15 (Jan. 2014), p. 17. DOI: `10.1186/1471-2202-15-17`.

[34] Valentina Pasquale, Sergio Martinoia, and Michela Chiappalone. “A self-adapting approach for the detection of bursts and network bursts in neuronal cultures”. In: *Journal of computational neuroscience* 29 (Sept. 2009), pp. 213–29. DOI: `10.1007/s10827-009-0175-1`.

[35] Jaap Pelt et al. “Long-Term Characterization of Firing Dynamics of Spontaneous Bursts in Cultured Neural Networks”. In: *Biomedical Engineering, IEEE Transactions on* 51 (Dec. 2004), pp. 2051 –2062. DOI: `10.1109/TBME.2004.827936`.

[36] Jaap van Pelt et al. “Dynamics and plasticity in developing neuronal networks in vitro”. In: Progress in Brain Research 147 (2005), pp. 171 –188. ISSN: 0079-6123. DOI: `https://doi.org/10.1016/S0079-6123(04)47013-7`. URL: `http://www.sciencedirect.com/science/article/pii/S0079612304470137`.

[37] Jerome Pine. “Recording action potentials from cultured neurons with extracellular microcircuit electrodes”. In: *Journal of Neuroscience Methods* 2.1 (1980), pp. 19 –31. ISSN: 0165-0270. DOI: `https://doi.org/10.1016/0165-0270(80)90042-4`. URL: `http://www.sciencedirect.com/science/article/pii/0165027080900424`.

[38] S. M. Potter et al. “Long-term bidirectional neuron interfaces for robotic control, and in vitro learning studies”. In: 4 (2003), 3690–3693 Vol.4. ISSN: 1094-687X. DOI: `10.1109/IEMBS.2003.1280959`.

[39] Steve Potter. “How Should We Think About Bursts?” In: *6th Int. Meeting on Substrate-Integrated Microelectrodes* (2008), 22–25.

[40] Steve M Potter and Thomas B DeMarse. “A new approach to neural cell culture for long-term studies”. In: *Journal of Neuroscience Methods* 110.1 (2001), pp. 17 –24. ISSN: 0165-0270. DOI: `https://doi.org/10.1016/S0165-0270(01)00412-5`. URL: `http://www.sciencedirect.com/science/article/pii/S0165027001004125`.

[41] Steve M Potter and Thomas B DeMarse. "A new approach to neural cell culture for long-term studies". In: *Journal of Neuroscience Methods* 110.1 (2001), pp. 17 –24. ISSN: 0165-0270. DOI: `https://doi.org/10.1016/S0165-0270(01)00412-5`. URL: `http://www.sciencedirect.com/science/article/pii/S0165027001004125`.

[42] J.D. Rolston, D.A. Wagenaar, and S.M. Potter. "Precisely timed spatiotemporal patterns of neural activity in dissociated cortical cultures". In: *Neuroscience* 148.1 (2007), pp. 294 –303. ISSN: 0306-4522. DOI: `https://doi.org/10.1016/j.neuroscience.2007.05.025`. URL: `http://www.sciencedirect.com/science/article/pii/S0306452207006689`.

[43] Mark van Rossum. "A Novel Spike Distance". In: *Neural Computation* 13 (Apr. 2001), pp. 751–763. DOI: `10.1162/089976601300014321`.

[44] Jugelt K-Teichmann C Weiss D. Schroeder OH-U Gramowski A. "Spike train data analysis of substance-specific network activity: application to functional screening in preclinical development". In: *6th international meeting on substrate-integrated microelectrodes.* (2008).

[45] Chris Sekirnjak et al. "Electrical stimulation of mammalian retinal ganglion cells with multielectrode arrays". In: *Journal of neurophysiology* 95 (June 2006), pp. 3311–27. DOI: `10.1152/jn.01168.2005`.

[46] Jan Stegenga et al. "Analysis of Cultured Neuronal Networks Using Intraburst Firing Characteristics". In: *Biomedical Engineering, IEEE Transactions on* 55 (May 2008), pp. 1382 –1390. DOI: `10.1109/TBME.2007.913987`.

[47] Jyothsna Suresh et al. "Network Burst Activity in Hippocampal Neuronal Cultures: The Role of Synaptic and Intrinsic Currents". In: *Journal of Neurophysiology* 115 (Mar. 2016), jn.00995.2015. DOI: `10.1152/jn.00995.2015`.

[48] Floris Takens. "Detecting Strange Attractors in Turbulence. Lecture Notes in Mathematics". In: *Lecture Notes in Mathematics* 898 (Nov. 2006), pp. 366–381. DOI: `10.1007/BFb0091924`.

[49] Heidi Teppola, Jugoslava Aćimović, and Marja-Leena Linne. "Unique Features of Network Bursts Emerge From the Complex Interplay of Excitatory and Inhibitory Receptors in Rat Neocortical Networks". In: *Frontiers in Cellular Neuroscience* 13 (2019), p. 377. ISSN: 1662-5102. DOI: `10.3389/fncel.2019.00377`.

[50] C.A. Thomas et al. "A miniature microelectrode array to monitor the bioelectric activity of cultured cells". In: *Experimental Cell Research* 74.1 (1972), pp. 61 –66. ISSN: 0014-4827. DOI: `https://doi.org/10.1016/0014-4827(72)90481-8`. URL: `http://www.sciencedirect.com/science/article/pii/0014482772904818`.

[51] Tin Kam Ho. "Random decision forests". In: 1 (1995), 278–282 vol.1. DOI: `10.1109/ICDAR.1995.598994`.

[52] Ildikó Vajda et al. "Low-Frequency Stimulation Induces Stable Transitions in Stereotypical Activity in Cortical Networks". In: *Biophysical Journal* 94.12 (2008), pp. 5028 –5039. ISSN: 0006-3495. DOI: `https://doi.org/10.1529/biophysj.107.112730`. URL: `http://www.sciencedirect.com/science/article/pii/S0006349508703667`.

[53] D. Wagenaar, T. B. DeMarse, and S. M. Potter. "MeaBench: A toolset for multi-electrode data acquisition and on-line analysis". In: (2005), pp. 518–521. ISSN: 1948-3554. DOI: `10.1109/CNE.2005.1419673`.

[54] Daniel Wagenaar, Zoltan Nadasdy, and Steve Potter. “Persistent dynamic attractors in activity patterns of cultured neuronal networks”. In: *Physical review. E, Statistical, nonlinear, and soft matter physics* 73 (June 2006), p. 051907. DOI: `10.1103/PhysRevE.73.051907`.

[55] Daniel Wagenaar, Jerome Pine, and Steve Potter. “An extremely rich repertoire of bursting patterns during the development of cortical cultures. BMC Neurosci 7:11”. In: *BMC neuroscience* 7 (Feb. 2006), p. 11. DOI: `10.1186/1471-2202-7-11`.

[56] Daniel Wagenaar et al. “Controlling Bursting in Cortical Cultures with Closed-Loop Multi-Electrode Stimulation”. In: *The Journal of neuroscience : the official journal of the Society for Neuroscience* 25 (Feb. 2005), pp. 680–8. DOI: `10.1523/JNEUROSCI.4209-04.2005`.

[57] Daniel A et al. Wagenaar. “Persistent dynamic attractors in activity patterns of cultured neuronal networks”. In: *Physical review. E* 73.5 (2006). ISSN: 051907. DOI: `10.1103/PhysRevE.73.051907`.